

Rochester Institute of Technology

## RIT Digital Institutional Repository

---

Theses

---

2012

### Scanning evanescent wave lithography for sub-22nm generations

Peng Xie

Follow this and additional works at: <https://repository.rit.edu/theses>

---

#### Recommended Citation

Xie, Peng, "Scanning evanescent wave lithography for sub-22nm generations" (2012). Thesis. Rochester Institute of Technology. Accessed from

This Dissertation is brought to you for free and open access by the RIT Libraries. For more information, please contact [repository@rit.edu](mailto:repository@rit.edu).

# SCANNING EVANESCENT WAVE LITHOGRAPHY FOR SUB-22 NM GENERATIONS

by

PENG XIE

A DISSERTATION

Submitted in partial fulfillment of the requirements  
For the degree of Doctor of Philosophy  
in  
Microsystems Engineering  
at the  
Rochester Institute of Technology

November 2012

Author: \_\_\_\_\_  
Peng Xie  
Microsystems Engineering Program

Certified by: \_\_\_\_\_  
Bruce W. Smith, Pd.D.  
Professor of Microsystems Engineering

Approved by: \_\_\_\_\_  
Bruce W. Smith, Ph.D.  
Director of Microsystems Engineering Program

Certified by: \_\_\_\_\_  
Harvey J. Palmer, Ph.D.  
Dean, Kate Gleason College of Engineering

# Scanning Evanescent Wave Lithography for Sub-22nm Generations

By

Peng Xie

Submitted by Peng Xie in partial fulfillment of the requirements for the degree of Doctor of Philosophy in Microsystems Engineering and accepted on behalf of the Rochester Institute of Technology by the dissertation committee.

We, the undersigned members of the Faculty of the Rochester Institute of Technology, certify that we have advised and/or supervised the candidate on the work described in this dissertation. We further certify that we have reviewed the dissertation manuscript and approve it in partial fulfillment of the requirements of the degree of Doctor of Philosophy in Microsystems Engineering.

## Approved by:

Dr. Bruce W. Smith \_\_\_\_\_ Date  
(Committee Chair and Dissertation Advisor)

Dr. John H. Bruning \_\_\_\_\_ Date

Dr. Karl D. Hirschman \_\_\_\_\_ Date

Dr. Zhaolin Lu \_\_\_\_\_ Date

Dr. Stefan Preble \_\_\_\_\_ Date

MICROSYSTEMS ENGINEERING PROGRAM  
ROCHESTER INSTITUTE OF TECHNOLOGY

November 2012

## ABSTRACT

Kate Gleason College of Engineering  
Rochester Institute of Technology

**Degree:** Doctor of Philosophy                      **Program:** Microsystems Engineering

Name of Candidate: Peng Xie

Title: Scanning Evanescent Wave Lithography for Sub-22nm Generations

Current assumptions for the limits of immersion optical lithography include NA values at 1.35, largely based on the lack of high-index materials. In this research we have been working with ultra-high NA evanescent wave lithography (EWL) where the NA of the projection system is allowed to exceed the corresponding acceptance angle of one or more materials of the system. This approach is made possible by frustrating the total internal reflection (TIR) evanescent field into propagation. With photoresist as the frustrating media, the allowable gap for adequate exposure latitude is in the sub-100 nm range. Through static imaging, we have demonstrated the ability to resolve 26 nm half-pitch features at 193 nm and 1.85 NA using existing materials. Such imaging could lead to the attainment of 13 nm half-pitch through double patterning. In addition, a scanning EWL imaging system was designed, prototyped with a two-stage gap control imaging head including a DC noise canceling carrying air-bearing, and a AC noise canceling piezoelectric transducer with real-time closed-loop feedback from gap detection. Various design aspects of the system including gap detection, feedback actuation, prism design and fabrication, software integration, and scanning scheme have been carefully considered to ensure sub-100 nm scanning. Experiments performed showed successful gap gauging at sub-100 nm scanning height. Scanning EWL results using a two-beam interference imaging approach achieved pattern resolution comparable to static EWL imaging results. With this scanning EWL approach and the imaging head developed, optical lithography becomes extendable to sub-22 nm generations.

Abstract Approval:                      Committee Chair: \_\_\_\_\_

Program Director: \_\_\_\_\_

Dean, KGCOE: \_\_\_\_\_

## ACKNOWLEDGMENTS

First and foremost, I'd like to thank my father Zhenfu Xie and my mother Xiejun Zhao. Without their guidance, constant care and unconditional love, I could have never reached this far in my life. My father always had this vision in higher education and deeply believed that education changes lives, even when there were times that I don't. I share this thesis and my doctorate degree with my parents. I love you, Mom and Dad, forever.

I want to thank my wife, Chanchan Du. This journey would have been much harder without you. No matter where you were, Chengdu, Rochester, Dubai; and no matter where I was, Rochester, Leuven, Rochester, our relationship has been faithful and joyful. Just knowing the fact that you are always there gives me the extra motivation to do better. I love you, Chanchan, forever.

I am grateful to my advisor, Dr. Bruce W. Smith. He brought me into this fascinating field of nanolithography. Coming from a different academic background, the transition was difficult but Dr. Smith allowed me enough freedom to choose my projects. None of the research results presented in this thesis could have happened without his guidance, encouragement and support.

I thank my committee members Dr. John H. Bruning, Dr. Karl D. Hirschman, Dr. Zhaolin Lu and Dr. Stefan Preble for their useful guidance and help along my dissertation research. I also want to thank all the useful discussions and cares that I receive from my group members and friends, Neal Lafferty, Jianming Zhou, Anatoly Bourov, Andrew Estroff, Burak Baylav. I enjoyed sharing the work place with Monica Sears, Germain Fenger and Chris Maloney. I am grateful to Steve Smith for helping me with

brainstorming and designing the imaging head. I would also like to acknowledge help from my coworkers at the microsystems engineering program Liang Cao and Ruoxi Yang.

I want to acknowledge the people at RIT who helped me with work and life. Sharon Stevens, our program secretary; John Nash, Bruce Tolleson and all SMFL staff; Dr. Dale Ewbank; and all the professors I've had. Lastly, I thank SRC and Sematech which provided funding for this project.

## TABLE OF CONTENTS

1. Lithography: past, present and future .....	1
1.1 Projection optical lithography: an overview .....	1
1.2 Double patterning: a successor to projection optical lithography .....	6
1.3 NGL: beyond 22 nm node .....	7
1.3.1 EUV lithography .....	8
1.3.2 193 nm immersion lithograph + multiple patterning .....	9
1.3.3 Maskless lithography .....	10
1.3.4 Nanoimprint lithography .....	12
1.3.5 193 nm immersion lithography + directed self-assembly .....	13
1.3.6 A reflection on NGL: call for regular design.....	13
1.4 Interference lithography: a NGL not on the roadmap?.....	15
1.5 Research motivation .....	15
2. Interference lithography: theory and scalability .....	18
2.1 Interference imaging theory .....	18
2.1.1 Experimental setup .....	18
2.1.2 Pitch dependence.....	20
2.1.3 Coherence, field size and defects .....	23
2.2 Extending IL to sub-22 nm nodes .....	26
2.2.1 IL+DPL/MPL.....	26
2.2.2 IL+DSA .....	36
2.2.3 Mask trimming considerations.....	38
2.3 IL limitations and paths towards manufacturing.....	40
3. Evanescent wave lithography: theory and static imaging .....	42
3.1 Introduction.....	42

3.2	Evanescent wave lithography.....	43
3.2.1	Total internal reflection and evanescent field.....	43
3.2.2	Frustrated total internal reflection.....	44
3.2.3	Simulation study.....	47
3.2.4	Interference imaging with EWL.....	49
3.3	Static imaging approach and results.....	50
3.3.1	Experimental setup.....	50
3.3.2	Results and discussion.....	52
3.3.3	On $NA_{sys} > NA_{resist}$ Imaging.....	57
3.3.4	Next generation resist research.....	59
4.	Designing a scanning EWL head.....	64
4.1	System Architecture.....	65
4.1.1	Design task identification.....	65
4.1.2	System design overview.....	66
4.2	System design considerations and implementations.....	68
4.2.1	Gap detection.....	68
4.2.2	Scanning head design.....	70
4.2.3	Prism design and manufacturing.....	75
4.2.4	Control circuit design.....	79
4.2.5	Scanning approaches.....	83
4.2.6	Sources of gap variation and system limitation.....	86
5.	Experiments and results.....	88
5.1	Experimental setup.....	88
5.2	Image contrast degradation.....	94
5.2.1	System vibration.....	94

5.2.2	Imaging misalignment .....	97
5.2.3	Process latitude.....	99
5.2.4	Gap height.....	100
5.3	Gapping and imaging with fused silica prism and sapphire prism .....	101
5.3.1	Static gap gauging .....	101
5.3.2	Dynamic gap gauging .....	104
5.3.3	Imaging results .....	107
6.	Conclusions and future work.....	111
7.	References .....	117

## LIST OF FIGURES

Figure 1: Imaging configuration of a simplified "6f" projection system used in optical lithography with Köhler illumination. ....	2
Figure 2. A schematic of the main components of an EUV lithography system [47]. ....	8
Figure 3. Illustration of quadruple pitch division by multiple patterning. Aerial image with intensity above the threshold is recorded in the photoresist. Subsequent exposures are done by shifting the mask $1/N^{\text{th}}$ of the original pitch. ....	10
Figure 4. Principles of electron beam lithography including multiple EBL [60]. ....	11
Figure 5. Schematic of the originally proposed NIL process [64]. ....	12
Figure 6. An example of Intel's SRAM poly gate layer design at 90nm (left) and 45 nm (right) [73]. ....	14
Figure 7. Schematic of the Smith Talbot interferometric lithography [89]. ....	19
Figure 8. Schematics of two prisms used in the bench-top system. Left: sapphire prism; Right: quartz half-ball prism [87]. ....	20
Figure 9. Pitch dependence on interference angle. Larger angle results in finer repeated patterns. ....	21
Figure 10. Wave propagation (reflection and refraction) through the imaging stack. ....	22
Figure 11. Image contrast loss as a function of distance from center of field [96]. ....	25
Figure 12. Field ringing effect from coherent diffraction from the edge of the circular field stop [96]. ....	26
Figure 13. a. over exposing a positive resist results in line CD well below the half-pitch; b. sinusoidal aerial image showing different resist/developer threshold level affects the CD. The spatial period pitch remains the same. ....	28
Figure 14. Left: illustration of pitch division through dual tone development process. The area above the threshold (e) set by the positive-tone developer and below the threshold (f) set by the negative-tone developer is removed [107]. Right: top-down SEM image of resist pattern with 50 nm 1:1 L/S features printed by the dual tone development process [108]. ....	29
Figure 15. Positive-tone double line process (left) and negative-tone double trench process (right) used in a standard LELE double patterning process [111]. ....	30
Figure 16. a. 44nm 1:1 L/S pattern obtained by positive and negative tone resists on resist double patterning. L2, which corresponds to the negative tone resist imaging, shows	

rough line edge [108]; b. 32 nm on 128 nm double pitch obtained from positive-positive tone resist combination [117].	32
Figure 17. Generic process flow and SEM image snapshots for Applied Materials' positive tone self-aligned spacer double patterning [119].	33
Figure 18. Detailed process schemes for higher order pitch division. a-c. triple patterning including triple exposure, LELELE and LFLFLF; d-e. quadruple patterning including iterative spacer and freezing assisted double spacer; f. mix-and-match process.	35
Figure 19. Conventional graphoepitaxy DSA process using positive-tone photoresist.	37
Figure 20. Conventional chemical epitaxy DSA process using pattern-first, neutralization approach.	38
Figure 21. Upper: SEM snapshots of GDR lines and cuts patterns including 35 nm half-pitch DRAM (left), 32 nm half-pitch SRAM (center) and 22 nm half-pitch SRAM (right); Lower: 26nm half-pitch damascene trench patterning demonstration for 16nm logic node GDR [127].	39
Figure 22. SEM images showing spacer formation after defining the core pattern [128].	40
Figure 23. Reflection and transmission at a thin, homogenous film.	45
Figure 24. TE transmittance through gap thickness for different gap refractive indices. $n_1=1.92$ , $n_3=1.7$ , $\lambda=193$ nm, incident angle at $56^\circ$ corresponding to 1.6 NA. $n_2$ is set to vary from 1 to 1.55.	46
Figure 25. Frustrated TIR dependencies on (a) gap thickness, (b) numerical aperture, (c) resist material and (d) gap material. Simulation conditions are as follows except for the plots where the corresponding parameters are varied: $\lambda=193$ nm; gap thickness $d=20$ nm; system NA=1.6; incident medium (sapphire) $n_1=1.92$ , $k_1=0$ ; gap material (air) $n_2=1.0$ , $k_2=0$ ; resist material $n_3=1.7$ , $k_3=0.04$ . The only exception is for (c) where the extinction coefficient is kept at $k_3=0$ when varying the refractive index $n_3$ .	48
Figure 26. ILSim2 simulation on two-beam interference EWL. TE polarized 193 nm laser incident with 1.5 NA from sapphire ( $n=1.92$ ) through 20 nm air gap on 50 nm thick photoresist ( $n=1.692$ , $k=0.042$ ). The BARC is optimized with 40 nm thickness to minimize reflection.	49
Figure 27. A two-beam Talbot interferometer with a two-piece modified prism holder.	50
Figure 28. (a). (c): laser reflection measurement at different torque values when air and water are used as the gap materials, respectively. The measured transmittance T is referenced to simulated data to calibrate the corresponding gap thickness; (b). (d): SEM photographs showing 32 nm half-pitch line space grating using air and water as the gap medium, respectively. The torque for both cases is kept at 50 inch-lbs.	53

Figure 29. (a)-(c): laser reflection measurement at different torque values when air, water and cyclohexane are used as the gap materials, respectively. The measured transmittance T is referenced to simulated data to calibrate the corresponding gap thickness; (d)-(f): SEM photographs showing 30 nm half-pitch line space grating using air, water and cyclohexane as the gap medium, respectively. The torque for all cases is kept at 40 inch-lbs. ....	55
Figure 30. SEM photographs showing line space grating (a). 30 nm half-pitch (1.6NA); (b). 26 nm half-pitch (1.83 NA). Air gap is used in both cases. Torque is kept at 40 inch-lbs. ....	57
Figure 31. For an absorbing medium ( $n=1.7$ , $k=0.04$ ), both the effective refractive index and effective extinction coefficient increases with system NA (incident angle) above the nominal refractive index. The net result is surface imaging on the top $<20$ nm region. Light is incident from sapphire ( $n=1.92$ , $k=0$ ). ....	58
Figure 32. (a) resist profile simulation by ILSim2 at NA larger than the nominal refractive index of the resist; (b) Frustrated TIR transmittance through the evanescent gap and into the photoresist as a function of nominal resist extinction coefficient. System NA is 1.8. All other simulation conditions are kept the same. ....	59
Figure 33. (a) 60 nm lines on a 60 nm half-pitch written in ZircSOx using 193 nm optical interference lithography at a dose of $25 \text{ mJ/cm}^2$ ; (b) 60 nm half-pitch crosshatched patterns produced by static interference EWL imaging with LFLE double patterning process. ....	61
Figure 34. SEM images of patterns printed on the HfO nanoparticle resist using 193 nm static interference EWL: 60 nm half-pitch negative tone (upper) and 50 nm half-pitch negative tone (bottom). ....	62
Figure 35. Schematic of the two-beam interference scanning EWL system. ....	67
Figure 36. Total internal reflection detection and gap referencing. ....	68
Figure 37. Experimental reflected irradiance observations of a 1.5 NA near-field solid immersion lens tester that focuses through an air gap onto a flat sample of BK7 glass. Observations were made at air gaps of 1000 nm, 500 nm, 200 nm, 100 nm, 50 nm, 20 nm and 0 nm. The illumination was linearly polarized in the vertical direction. [Reproduced from [145]] ....	69
Figure 38. Two-stage gap control head with passive air floating system to control low frequency noise and active piezoelectric transducer feedback system to control high frequency deviation. ....	70
Figure 39. 50 mm air bearing. Left: original vacuum preloaded air bearing purchased from New Way Air Bearing; Right: customized air pad with tight slip fit and side openings. ....	71

Figure 40. Prism holder designed to fit in the air bearing and actuated by the piezo-transducer.....	72
Figure 41. Piezoelectric transducer and its voltage-displacement curve.....	72
Figure 42. Assembled prism, prism holder, piezoelectric transducer and an adapting plate. The prism was glued to the prism holder through the side holes. The piezoelectric transducer was glued on both ends to the prism holder and an adapting plate. ....	73
Figure 43. Assembled scanning EWL imaging head. Left: Bottom view of the air bearing with prism inserted; Right: Side view of the imaging head with screw and spacer identified. ....	74
Figure 44. SolidWorks design of the assembled imaging head. ....	75
Figure 45. Four different configurations of the exit surface of the final prism. (a). a flat surface; (b). a small protruding flat head; (c). a semi-spherical surface; (d). a truncated cone with a small flat tip.....	76
Figure 46. Design of the modified prism with a truncated cone exit surface. The conical angle is set to be 80 degrees and flat tip has a width between 20 and 50 $\mu\text{m}$ . ....	76
Figure 47. Surface roughness profile of a truncated cone exit surface. The image shows a test-run result on a glass sample without protective coating. The center flat strip shows a width around 50 $\mu\text{m}$ . ....	77
Figure 48. Modified prisms with a truncated cone exit surface. Left: photograph of a fused silica prism; Center: sapphire prism with 275 $\mu\text{m}$ center flat tip; Right: fused silica prism with 44 $\mu\text{m}$ wide center flat tip.....	78
Figure 49. Total internal reflection detection and gap referencing. ....	79
Figure 50. Gap control block diagram. ....	81
Figure 51. Front panel of the gap control and feedback system. ....	81
Figure 52. Block diagrams of the two case structures used in the control algorithm. Upper: Case 1 to take TIR reference with calibrated photodiode detectors; Lower: Case 2 to take active gap signal, relate to Matlab code to determine gap, and then feed back to PZT using PID control loop. ....	82
Figure 53. A block diagram of a typical PID controller. ....	83
Figure 54. Depiction of two possible scanning schemes used by SBIL. (a) Parallel scanning. (b) Doppler scanning [150]. ....	84
Figure 55. Schematics of the exposure schemes used in this work. The image field was exposed while the wafer is stationary. After each exposure, the wafer scans in the linear	

direction at sub-100 nm gap to another isolated location await next exposure. Gap control system is always active in both exposure and scanning modes. Beam A and beam B are intentionally misplaced to illustrate two-beam interference imaging. The size of the image field is determined by the prism bottom flat.....	85
Figure 56. Experimental setup of the EWL head with static gap control. Additional optics were used to shape and direct the reference gap control laser beam. ....	88
Figure 57. Reflected intensity as a function of incident laser light fluctuation. Left: Incident laser light fluctuation; Right: reflected laser light fluctuation. The two beams were separated by a non-polarizing beam splitter and detected with two calibrated broadband photodiodes. ....	90
Figure 58. Two configurations showing misalignment between monitor laser and prism bottom flat when the imaging head moves vertically. (a): Final turning mirror mounted on micrometer stage; (b): Final turning mirror stationary. ....	91
Figure 59. Left: Normalized reflectance power when the EWL head was driven toward the wafer surface by a motorized micrometer stage. The signal first increases which indicates the misalignment between the reference laser and the prism flat tip. The laser is aligned with the prism as soon as the reflectance reaches its peak. Further movement of the head toward the wafer surface induces evanescent coupling; Right: Simulated reflectance as a function of gap thickness in the gapping setup used in this experiment. The inset shows the experimental and simulation condition. ....	92
Figure 60. Static EWL head with gap control module to maintain constant gap above wafer surface. The EWL head was mounted on a motorized micrometer stage while the wafer is placed on an XY translation stage.....	93
Figure 61. Illustrations of imaging samples indicating prism tilt and imaging beam misalignment. ....	94
Figure 62. Measured vertical vibration velocity spectrum on SEWL imaging system. ....	96
Figure 63. Measured horizontal vibration velocity spectrum on SEWL imaging system. ....	96
Figure 64. Simulated and experimental verification of contrast degradation as a function of system misalignment OPD between two interferometric arms. Experiments carried out on static EWL system with NA=1.3. ....	98
Figure 65. SEM snapshots showing pattern imaging quality degradation as a function of dose. Experiments carried out on static EWL system with NA=1.3. ....	100
Figure 66. Simulated and experimental verifications of image quality degradation as a function of imaging plane defocus. Experiments carried out on static EWL system with NA=1.3. ....	100

Figure 67. SEM snapshots of 1:1 line-space grating taken at different gap heights. Experiments carried out on static EWL system with NA=1.3. ....	101
Figure 68. Static gapping results with optimized controller at various gap heights. ....	102
Figure 69. Static gapping results showing gap heights variation in various control scenarios. ....	103
Figure 70. Static gapping results showing gap heights change when the gap target is adjusted in the control software. ....	103
Figure 71. Dynamic gapping with optimized controller at various gap heights. Scan speed =1 $\mu\text{m}/\text{sec}$ . ....	104
Figure 72. Comparative study on static vs. scanning gapping results with gap target set at 100 nm. ....	105
Figure 73. Comparative study on static vs. scanning gapping results with gap target set at 50 nm. ....	106
Figure 74. Plotted gap heights fluctuation when the wafer stage switches between stationary and scanning. ....	106
Figure 75. Dynamic gapping with different scan rate. ....	107
Figure 76. SEM snapshots of 1.35 NA line-and-space patterns imaged with stepping EWL using fused silica prism. ....	108
Figure 77. SEM snapshot of a non-uniform image field. 1.35 NA line-and-space patterns were imaged with stepping EWL using fused silica prism. Field non-uniformity is caused by local gap variations. ....	109
Figure 78. Left: photograph of an exposed silicon wafer sample. The bright line indicates the image field exposed with 1.2 NA stepping EWL using sapphire prism; Right: SEM snapshot of the image field. ....	110

## LIST OF TABLES

Table I. Gap thickness measurement and corresponding dose-to-size information at 1.5 NA. * indicates the minimum gap achieved with the gap material and resist stack. ....	54
Table II. Gap thickness measurement and corresponding dose-to-size information at 1.6 NA. * indicates the minimum gap achieved with the gap material and resist stack. Underlined values are extrapolated from the experiment and simulation. ....	56
Table III. Summary of the sources of gap variation and internal noises of the system.....	86
Table IV. Summary of the measured vibration data on SEWL imaging system. ....	97

## LIST OF ACRONYMS AND ABBREVIATIONS

BARC .....	Bottom Anti-Reflecting Coating
CAR.....	Chemically Amplified Resists
CD.....	Critical dimension
DOF .....	Depth of Focus
DPL.....	Double Patterning Lithography
DSA .....	Directed Self-Assembly
EBL.....	Electron-Beam Lithography
EDA.....	Electronic Design Automation
EUVL.....	Extreme Ultra Violet Lithography
EWL.....	Evanescent Wave Lithography
GDR.....	Gridded Design Rule
IL .....	Interference Lithography
ITRS.....	International Technology Roadmap for Semiconductors
LELE.....	Litho-Etch-Litho-Etch
LER.....	Line-Edge Roughness
LFLE.....	Litho-Freeze-Litho-Etch
LuAG .....	LUtanium Aluminum Garnet
MEBL .....	Multiple Electron-Beam Lithography
ML2 .....	Maskless Lithography
MPL .....	Multiple Patterning Lithography

NA ..... Numerical Aperture

NGL ..... Next Generation Lithography

NIL ..... Nano Imprint Lithography

OPC ..... Optical Proximity Correction

OPD ..... Optical Path Difference

PAG ..... Photo-Acid Generator

PEB ..... Post-Exposure Bake

PID ..... Proportional-Integral-Derivative

PML2 ..... Projection Maskless Lithography

PSM ..... Phase Shift Mask

rCEL ..... reversible Contrast Enhancement Layer

REBL ..... Reflective Electron-Beam Lithography

RET ..... Resolution Enhancement Technique

RLS ..... Resolution, Line-edge-roughness and Sensitivity

SADP ..... Self-Aligned spacer Double Patterning

SBIL ..... Scanning Beam Interference Lithography

SEM ..... Scanning Electron Microscope

SIL ..... Solid Immersion Lens

TE ..... Transverse Electric (s polarized)

TIR ..... Total Internal Reflection

TPA ..... Two-Photon Absorption

---

# 1. LITHOGRAPHY: PAST, PRESENT AND FUTURE

---

## 1.1 Projection optical lithography: an overview

Lithography represents a complex process of defining and transferring miniature circuit patterns from design templates to real devices. It has been essential to the advancement of semiconductor devices ever since its inception [1], [2]. While semiconductor manufacturing aims to produce devices with more functionality, faster speed, greater packing density and lower power consumption etc., these attributes closely rely on what lithography can deliver: minimum line-width. To date, optical lithography has been the workhorse for semiconductor manufacturing [3], [4]. Compared to other patterning techniques such as imprint lithography, X-ray lithography, and electron beam lithography, optical lithography offers the advantages of higher information transfer per bit, cost-effectiveness, defect-free large area patterning, and robust infrastructure.

In 1971, Intel released its first ever microprocessor, the Intel 4004, containing 2300 transistors on an area of 12 mm<sup>2</sup>. The 10 μm optical lithography process relied on physically cutting sheets of Rubylith into thin strips to lay out the circuits to be printed. Now 40 years later, Intel announced its 32 nm process 10-Core Xeon Westmere-EX microprocessor counting 2.6 billion transistors on an area of 512 mm<sup>2</sup>. Starting with contact/proximity lithography, optical lithography has transitioned through 14 technology nodes in a span of almost 50 years decreasing from 10 μm half-pitch to 32 nm [5], [6]. State-of-the-art water immersion projection lithography, which employs a 193 nm ArF excimer laser source with 1.35 NA catadioptric projection optics, prints minimum features around 40 nm [7].

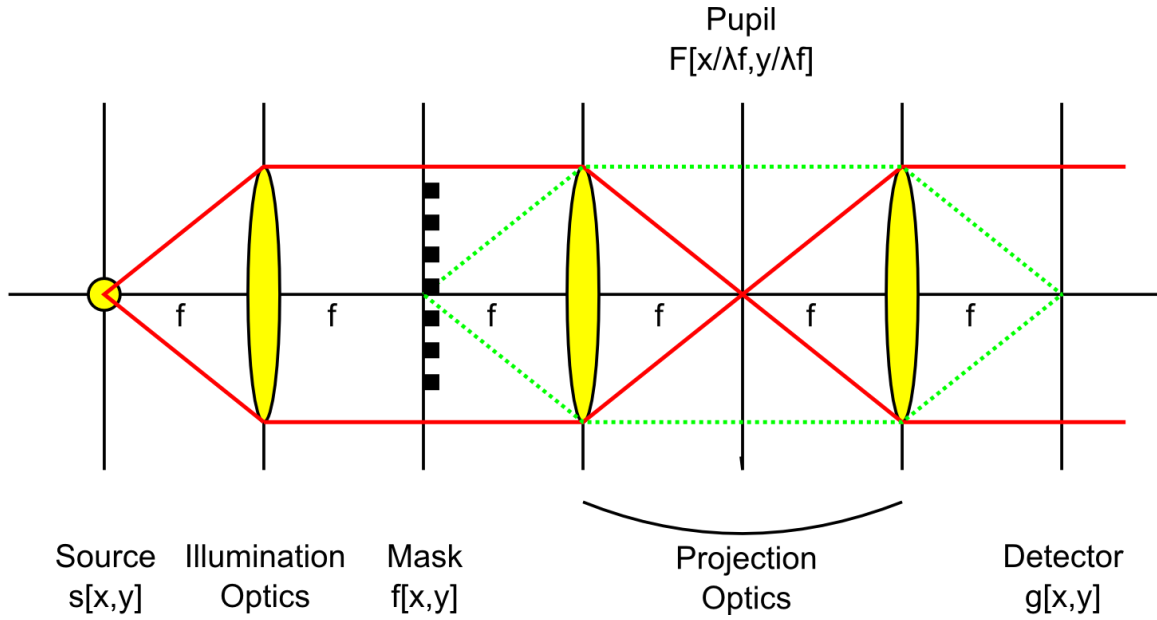


Figure 1: Imaging configuration of a simplified "6f" projection system used in optical lithography with Köhler illumination.

A simplified version of a projection lithography system, depicted in Figure 1, can be represented as five components: a light source, illumination optics, a mask with design pattern, projection/collection optics and a photodetector. In Köhler illumination setting, the image transformation/reduction takes place by imaging the mask pattern onto the detector plane while the source is focused onto the pupil plane. Under the realm of Fourier Optics, such system is well characterized by approximating light propagation in the Fraunhofer region [8], [9]. The physical limitation on imaging resolution is governed by the Rayleigh criterion [10], [11], which describes the system as diffraction limited

$$R = k_1 \frac{\lambda}{NA} \quad (1.1)$$

where  $R$  is the critical dimension (CD),  $\lambda$  is the illumination wavelength, and  $k_1$  represents the process capability and has a lower limit of 0.25 for incoherent illumination.

Over the years, the physics behind the Rayleigh criterion has been guiding the development of projection lithography system. Source wavelength scaling has been observed from mercury g-line (436 nm) illumination down to ArF 193 nm. Research in 157 nm F<sub>2</sub> laser source lithography was once intense, but failed due to a lack of suitable optics and photosensitive resist materials at this wavelength [12]. On the other hand, the advancement in lens making and design enabled higher-NA optics to be made. The NA limitation on a dry projection system was then overcome by the introduction of water immersion lithography at the lens/resist interface. Further development in high index liquid (HIL) lithography which promises >1.35 NA proves to be difficult because of the demanding requirement on not only the fluid, but also a drastic change in projection lens material and resist film stack [13]. The third factor, known as  $k_1$ , describes the process manufacturability. Various resolution enhancement techniques (RETs) have been developed including phase shift mask (PSM) [14], optical proximity correction (OPC) [15], off-axis illumination (OAI) [16], customized polarization [17], source mask optimization (SMO) [18], and design for manufacturability (DFM) [19].

Referencing the typical projection systems used in optical lithography in Figure 1 provides another way to look at the developments/innovations that take place at the component level:

1. Source: As NA reached its limit at a given wavelength, lens and tool design shifts to shorter wavelength to extend imaging resolution. This has led to the switch from mercury lamp wavelengths to excimer laser wavelengths at 248 nm and 193nm successively. Excimer lasers are pulsed premixed-gas laser light sources that are well suited for lithography applications because of their power scalability

[20]. The key matrices in evaluating its performance are power output, spectral bandwidth, stability and reliability. A state-of-the-art 193 nm excimer laser using an ArF gas premix operates with 6 kHz repetition rate, 90W average power, 0.3 picometer bandwidth and lifetime over 2 billion cycles [21]. Although excimer laser development is likely to peak at 1.35 NA immersion lithography, continued improvement is expected in the area of source stability and productivity to maximize process control budgets in double patterning processes.

2. Illumination optics: Traditionally, illumination optics aim to shape and position the effective light source and provide uniform illumination on the mask while preserving angular distribution. More recently, various RETs have been incorporated in the design of the illuminator, leading to the development of customized source diffractive optical element (DOE) [22], polarization control [23], and programmable illuminator FlexRay [24].
3. Mask: The pattern template defines the magnified (typically 4X) layer design geometry and requires defect-free precision. Any residual mask-error is likely to deteriorate image contrast and post CD violations through mask error enhancement factor (MEEF) [25]. Most commonly comprised of graded  $\text{CrO}_x\text{N}_y$  composite thin film on a transparent glass substrate, the photomask evolved from binary (two levels of intensity) to attenuated phase shift mask (a-PSM) which allows a significant amount of intensity through the dark regions with a  $180^\circ$  phase shift [26]. The benefit of allowing phase-shifted transmittance through the dark feature is to suppress the zero diffraction order and enhance the first order, which improves image contrast manifested through normalized image log slope

(NILS). The strong alternating phase-shift mask (alt-PSM) proposed by Levenson [14] had the potential for nearly doubling resolution and extending depth of focus (DOF), but eventually found limited use in manufacturing due to difficulty in mask design (phase conflicts and imbalance) and manufacturing [27]. The latest mask technology development has switched to the computational arena to provide a rigorous 3D mask description integrated in lithographic modeling [28].

4. Projection optics: The heart of any optical lithography system, the projection lens, images the relief pattern on the mask into the resist-coated wafer with appropriate reduction. Optics complexity has been increasing steadily over time, leading to larger NA (up to 1.35NA) and extremely low aberrations (wavefront RMS  $< 10$  m $\lambda$ ). State-of-the-art projection optics consists of more than 30 lens elements including at least 6 flexible lenses. Catadioptric lens design becomes essential in order to contain size and cost while keeping the image field flat [29]. Lately a new wavefront manipulator named FlexWave has been introduced in the ASML 1950i scanner to fine-tune wavefront using a local heating element [30].
5. Image detector: For the most part, the image detector used in optical lithography requires two primary functions: faithfully record the latent optical intensity distribution; and transfer such distribution from the detector to the substrate. For this purpose, conventional photoresists (photopolymeric etch resistant materials) are composed of multiple components wherein a base resin material is modified in terms of solubility upon photochemical reactions, followed by solvent development and transfer etch [31]. Photoresist chemistry evolved with each device generation, and major changes took place when the illumination source

shifted to a lower wavelength [32]. Modern chemically amplified resists (CAR) utilize a photosensitizing photoacid generator (PAG) to deblock the polymer resin in an acid-catalyzed chemical amplification reaction at elevated temperature [33]. Polymethacrylates bearing acid-labile ester functionality and an alicyclic pendant group have become a major foundation for the design of positive 193 nm resists [34]. Moving forward, CAR is facing physical challenges at sub-22 nm device nodes trading off resolution (R) for line-edge-roughness (L) and sensitivity (S), known as the RLS trade-off [35], [36]. Acid diffusion that occurs at the post-exposure bake (PEB) step induces stochastic effects and photon shot-noise and may eventually limit the use of CAR at advanced device nodes including EUV [37]. Development efforts are underway to find non-chemically amplified inorganic resists [38], [39].

Despite all the research and development efforts in the fields, the conventional scaling trend in optical projection lithography ended with 1.35 NA water immersion lithography. This was due to a combination of factors including physical limit in projection lithography resolution, material challenges at shorter-wavelengths and higher NA, technological and economic justifications compared to competitive technologies. The lithography community decided to find substitutes to projection lithography which led to the development of double patterning lithography (DPL) and next generation lithography (NGL) [5].

## **1.2 Double patterning: a successor to projection optical lithography**

In many ways, double patterning lithography was adopted by the industry not by choice but due to lack of options succeeding 1.35 NA single exposure systems [40].

Extreme ultra violet lithography (EUVL) which promises ultimate resolution failed to mature in time for the 32 nm and 22 nm nodes, suggesting the use of existing methods to enable production [41].

Initially proposed as a double-exposure double-etch process where one or more sacrificial hardmask layers are used to print the first patterning mask, DPL is double the trouble and poses challenges in cost of ownership and process control [42]. Various forms of DPL exist including litho-etch-litho-etch (LELE), litho-freeze-litho-etch (LFLE), self-aligned spacer double patterning (SADP), dual-tone development (DTD) and double exposure (DE) [43]. The details of each DPL approaches are surveyed in chapter 2. DPL effectively breaks the diffraction limit of  $0.25 k_1$  by doubling the spatial frequency through either two exposures or side-wall spacer formation. The realistic net gain in logic chip manufacturing is expected to be around 30% due to the splitting of conflicts in a complex chip layout. Taking the current state-of-the-art optical lithography resolution limit at 40 nm, double patterning is capable of printing logic circuits down to 28 nm. More aggressive scaling is possible with gridded design rules (GDRs) which can extend DPL to the 22 nm node, although some forms of triple patterning may have been used to pattern critical layers such as poly gate.

### 1.3 NGL: beyond 22 nm node

DPL is not capable of meeting the resolution requirement below the 22 nm node. A few candidates have been identified by the international technology roadmap for semiconductors (ITRS) including EUVL, 193 nm immersion lithography + multiple patterning, maskless lithography (ML2), nanoimprint lithography (NIL), 193 nm immersion lithography + directed self-assembly (DSA) [44]. Each technology promises

opportunities to pattern smaller features but also faces significant technological and engineering challenges [45].

### 1.3.1 EUV lithography

EUVL has been widely regarded as the most popular NGL choice [46]. Using the 13.5 nm wavelength, the ultimate resolution is mainly limited by the interaction volume in the photoresist. Given a 0.25 NA and a moderate 0.6  $k_1$ , 32 nm CD is attainable. Further process and illumination improvements can reduce the  $k_1$  factor to values closer to 0.5. Increased numbers of reflective multi-layer dielectric mirrors help increase system NA, but also put higher requirements on the source power because each mirror has only up to 70% reflectivity.

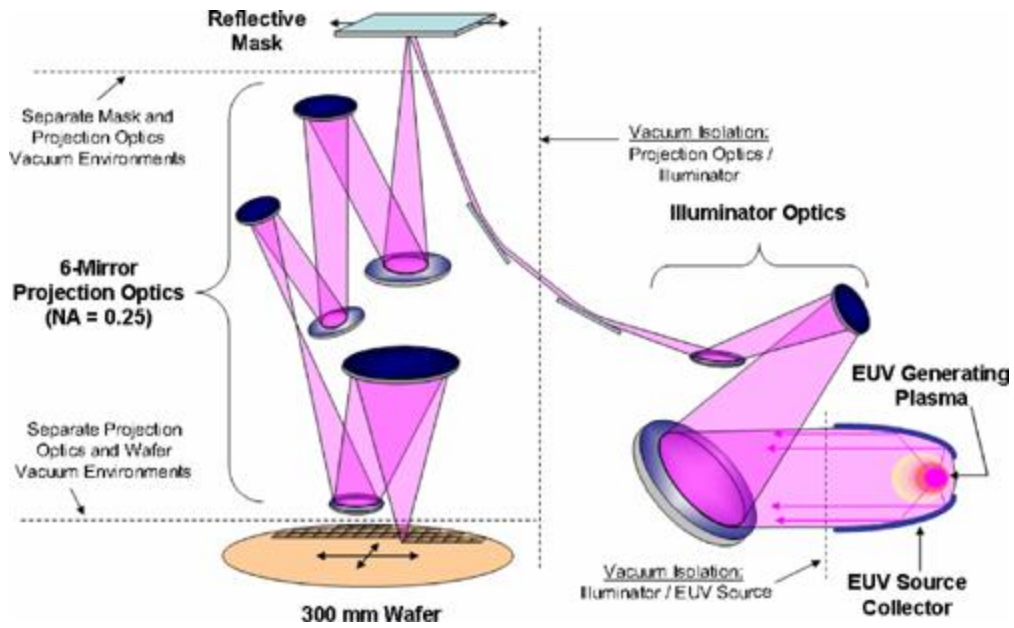


Figure 2. A schematic of the main components of an EUV lithography system [47].

Figure 2 illustrates the main components of an EUV lithography system [47]. Its design differs from conventional projection lithography in four major areas: laser produced plasma (LPP) or discharge produced plasma (DPP) source, multi-layer pseudo-

Bragg reflecting optics and reticle, vacuum environment, and resist chemistry. The latest ASML NXE: 3100 pre-production EUV tool exhibits 27 nm resolution and features 6 mirrors, 0.25 NA optics with a conventional  $0.8\sigma$  illumination, and 4.0 nm dedicated-chuck overlay (DCO), 60 wafer-per-hour throughput and  $10 \text{ mJ/cm}^2$  resist sensitivity [48]. Although these are significant improvements, critical issues remain to be addressed in three areas: reliable high power source, resist meeting RLS trade-offs, and a defect-free reticle [49], [50]. It remains unclear whether or not these issues can be solved in a timely manner while other competing patterning techniques get ready for sub-22 nm production. A combination of EUV lithography with some forms of DPL may be required to meet the resolution targets.

### 1.3.2 193 nm immersion lithograph + multiple patterning

Multiple patterning lithography (MPL) is the next conceptually straightforward extension to DPL [51]. An example of a quadrupole patterning aerial image is shown in Figure 3. Frequency multiplication can be achieved by splitting the pattern more than once, followed by a series of exposures and processing. These exposure and processing steps may take the form of: a. multiple exposures and etches (LE)<sup>n</sup>, where n is an integer greater than 2; b. multiple exposures and freezes (LF)<sup>n</sup>, where n is an integer greater than 2; and c. a multiple cascade of spacer process, i.e. spacer on spacer [52]. In addition, a mix-and-match strategy is also possible; this involves more than one conventional double patterning technique, e.g. LE+SADP. This gives extra degrees of freedom in optimizing the process and minimizing cost. It has been shown that overlay budget is not tightened in multiple patterning processes when compared to the double patterning scenario [53]. Recently, a self-aligned triple patterning (SATP) process has been proposed to pattern 15

nm half-pitch by keeping the mandrel lines and adding the second spacers [54]. Despite various process schemes, the key challenge remains in engineering tighter process control and justifying process complexity and cost. It is also a non-trivial issue for electronic design automation (EDA) tools to come up with manufacturable layout decomposition [55].

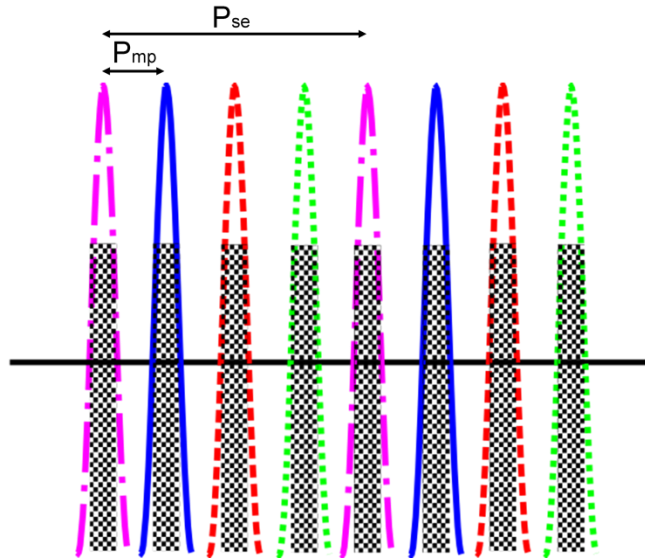


Figure 3. Illustration of quadruple pitch division by multiple patterning. Aerial image with intensity above the threshold is recorded in the photoresist. Subsequent exposures are done by shifting the mask  $1/N^{\text{th}}$  of the original pitch.

### 1.3.3 Maskless lithography

While many forms of maskless lithography (ML2) exist such as focused-ion-beam (FIB) lithography [56], dip-pen lithography [57] and zone-plate-array lithography [58], the most commonly used is electron-beam lithography (EBL). EBL is attractive to high resolution chip making because of the short electron wavelength and corresponding high resolution. However, single beam EBL relies on a serial writing process which led to

extremely slow writing speed and high cost, limiting its application in high-end photomask and research prototyping [59].

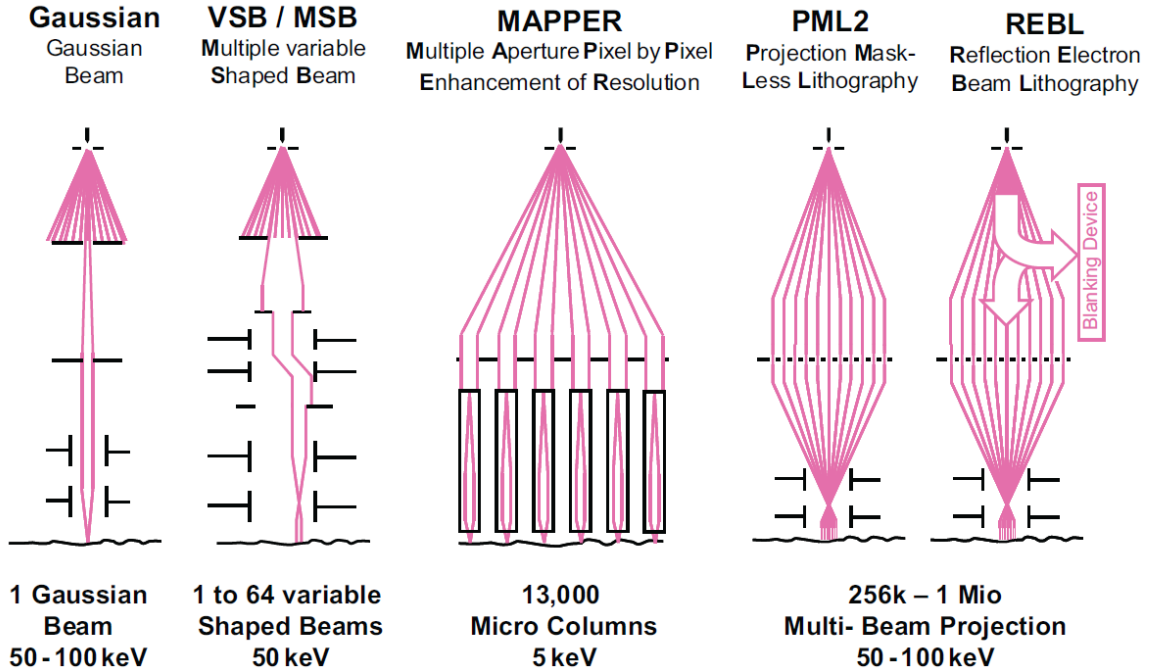


Figure 4. Principles of electron beam lithography including multiple EBL [60].

Recently, the lithography community decided to invest in multiple electron beam lithography (MEBL) to improve the throughput of the direct-write systems. Key design challenges include simultaneously coordinating thousands of beams in terms of their placement, size, and dose, managing individual beam defects and achieving gray-tone exposure [60]. Three major system structures have been studied by Mapper, reflective electron beam lithography (REBL), and projection maskless lithography (PML2), shown in Figure 4. While Mapper relies on a multiple micro-column array, REBL and PML2 both rely on a multi-beam projection system with REBL implementing a reflecting blanking device [61–63]. Each technology is still magnitude away from the required throughput in terms of the multitude of beams even with tool clustering. The low voltage

individual electron beam due to multi-beam splitting may induce stronger forward scattering which limit the resolution.

#### 1.3.4 Nanoimprint lithography

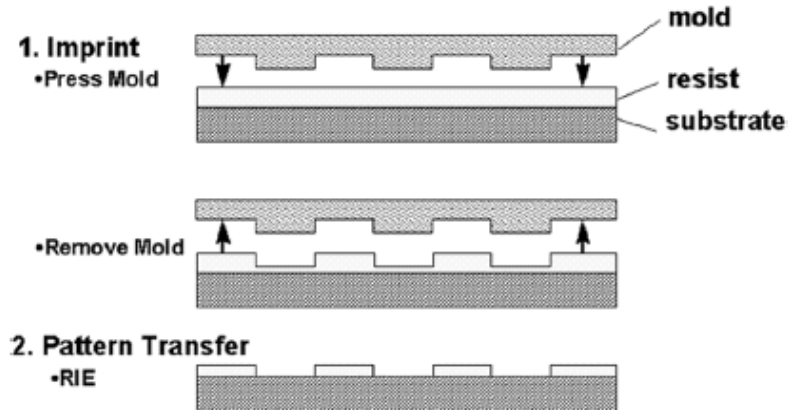


Figure 5. Schematic of the originally proposed NIL process [64].

NIL is another attractive patterning method in terms of its high resolution and low cost. Figure 5 shows a schematic of the originally proposed NIL process [64]. By mechanically deforming the imprint resist, the patterns are transferred from the template (mold) to the resist. Subsequent processes include heat or UV curing and proper release between the template and resist. This has led to the development of a step-and-flash imprint lithography (SFIL) process [65]. The resolution, however, still relies on other patterning techniques to generate the template. Similar to any contact printing process, key concerns to NIL need to be addressed including 1X patterning, alignment, defect control and repair, production-level throughput, template patterning and template lifetime. The method is more likely to find applications in niche markets such as patterned media, photonics and biology.

### 1.3.5 *193 nm immersion lithography + directed self-assembly*

Block copolymer based directed self-assembly (DSA) is the latest addition to NGL candidates due to its high resolution (10 nm), cost effectiveness, scalability and recently found compatibility with 193 nm lithography [66]. It relies on microphase segregation of two immiscible molecular blocks into microdomains to reduce the interfacial energy, forming periodic nanostructures such as lamellar, cylinder and spheres [67]. It became an attractive lithography technology when it was found that high frequency line patterns occur by subdividing larger scale lithographic structures into sub-lithographic units by either topographic pre-patterning (graphoepitaxy) or chemical pre-patterning [68–70]. Much of the development has been focused on study and control of the defect density due to inherent polymer phase defects [71]. More applications of the technology can be found in other aspects of microelectronics such as memory, nanowires and novel materials [72].

### 1.3.6 *A reflection on NGL: call for regular design*

No matter which technology, if any becomes a contender for NGL, significant amount of development and innovation is required. EUVL, still the most likely option, but has been delayed for two lithography nodes and may already be too late to print 16 nm half-pitch with single exposure. ML2 has a big problem with throughput even with tool clustering, making it cost-inhibitive. NIL is battling with defect control but may find greater applications in patterned media. DSA is still early in exploration phase and hard to predict. MPL sees no technology roadblocks but path toward integration is challenging. As a result, sub-22 nm lithography remains an open question.

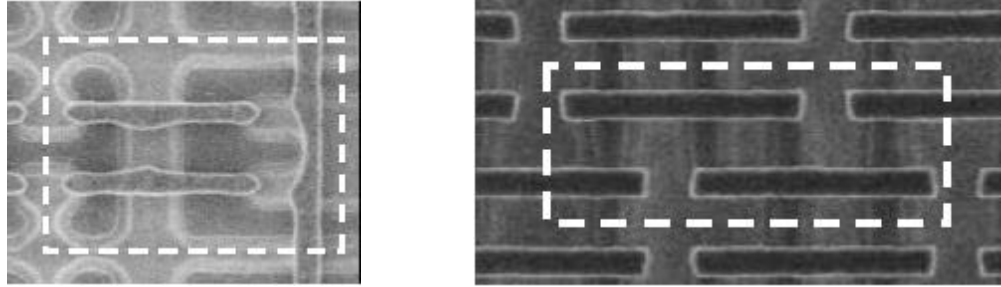


Figure 6. An example of Intel's SRAM poly gate layer design at 90nm (left) and 45 nm (right) [73].

Layout design is another area that cannot be ignored when considering NGL. For example, both MPL and DSA rely on 193 nm immersion lithography to generate a base template. The design and quality of the templates determines how to implement the pitch division technologies. The reality that designers have to follow lithography rules to yield a manufacturable design requires one to evaluate NGL not only from the technology and process viewpoints but also from design. For example, complex logic designs yield more decomposition conflicts than memory chips, making DPL more difficult for CPU chips [74]. The current trend in design rule evolution is so called gridded design rules (GDRs) where the layout structures become ultra-regular [75]. Figure 6 shows how Intel's SRAM poly design evolved from conventional 2D 90 nm to nearly GDR layout architecture at 45 nm [73]. The key benefit of such regular design is the ease of 1D patterning and scaling compared to 2D due to proximity effect [76]. Even with EUVL, which is less prone to proximity effect due to its high  $k_1$ , GDRs are attractive especially considering the possibility of a mix-and-match methodology between EUVL and DPL.

Consequently, large field ultra-regular 1D patterning technique becomes highly desirable for template patterning, followed by additional pitch division and trimming steps [77].

#### 1.4 Interference lithography: a NGL not on the roadmap?

Interference lithography (IL) is well suited for patterning 1D regular line-and-space structures [78–81]. It has been used in many non-IC repetitive patterning applications such as optical gratings [82], photonic crystals [83], and wire grid polarizers [84]. Differing from a conventional projection stepper/scanner, interference lithography produces periodic patterns by the coherent interference of multiple coherent laser beams. Analogous to dipole imaging in a projection system, interference lithography represents a system's ultimate resolution limit with high contrast and DOF. A  $k_1$  of 0.25 is generally assumed on such systems by applying suitable RETs such as phase shift mask and favorable polarization state.

Over the years, interference lithography has been on and off the ITRS roadmap many times, the most recent be in year 2009 [85]. The technology has been extensively studied and demonstrated academically but never seriously considered for high volume manufacturing (HVM) in the semiconductor industry. Some of the biggest question marks for the technology include (a). turning line-and-space gratings into working circuits; (b). printing large field size; and (c). high resolution IL printing less than 36 nm half-pitch (equivalent to 1.35 NA).

#### 1.5 Research motivation

As discussed above, traditional technological scaling trend in optical lithography has failed beyond the 32 nm node. This presents both great challenges and opportunities for new technologies. The lithography community is pursuing multiple paths in terms of developing NGL. On the other hand, the general trend observed is the use of ultra-regular layer design combined with some forms of innovation, e.g. 193 nm immersion + DSA,

and 193 nm immersion + DPL/MPL. This combinational patterning approach can be characterized with two parts: “template” + “manipulation”. While none of the NGL is optical, the templating technology is likely to remain optical lithography. Improvements can be made at both the “template” and the “manipulation”. It is therefore the objective of this thesis to improve the “template” using existing materials and infrastructure.

Optical interference lithography is a great platform for templating with its merits and limitations stated in the previous section. To compete with 1.35 NA immersion projection lithography as the templating technology, the most fundamental requirement for IL is to have NA above 1.35, namely printing smaller patterns. The high spatial frequency information stored in the evanescent field upon TIR, which doesn't exist in traditional projection lithography, is explored in this thesis. Upon frustrating the evanescent field with a nm-scale air/fluid gap, photons tunnel through this gap and interfere at the photoresist to form high NA patterns. This new imaging approach, evanescent wave lithography, differs from traditional projection lithography in breaking the constraint that  $NA_{\text{system}} < NA_{\text{material}}$ , greatly relaxing material requirement. Once the imaging theory is established, the technical challenge becomes to control and gauge such nm-scale gap with tight tolerance, which is the heart and soul of this thesis. We first carried out experiments in demonstrating static imaging with various gap fluids and NAs to study the interdependence among various imaging-related parameters to determine the optimum imaging conditions. For the technology to be useful in real-world manufacturing as a templating technology, we built a dynamic-scan imaging head with both passive and active feedback loop to gauge and control the scanning height while carrying out evanescent wave imaging.

In summary, none of the NGLs, including EUVL, is ready for sub-22 nm patterning. In the meantime, the emerging trend of GDRs, line-and-cut DPL, MPL and DSA presents opportunities for IL and especially evanescent wave lithography as potential candidates to replace projection lithography as a templating technology. It is not the objective of this thesis to defend IL as a candidate for NGL, but to present progress that has been made toward enabling evanescent wave lithography as a templating technology for its obvious advantage in achieving higher-NA using existing materials and infrastructure.

---

## 2. INTERFERENCE LITHOGRAPHY: THEORY AND SCALABILITY

---

### 2.1 Interference imaging theory

Interference imaging produces periodic patterns by interfering two or more coherent laser beams. It differs from projection lithography in a way that not all diffraction orders and angles are utilized. This eliminates the need for complex aberration-free lens systems that collect a maximum range of diffraction orders at the pupil plane. Instead, flexible varying angle mirror systems can be used to achieve the interference of diffraction orders at the image plane. In some special cases such as dipole illumination and alt-PSM, the function of a projection system closely resembles that of an interferometer [86].

Rigorous vector analysis of two-beam and three-beam interference imaging has been previously performed [87], [88]. Here, we review some key concepts relevant in answering the questions raised in Chapter 1.

#### 2.1.1 *Experimental setup*

Interference imaging approaches can be categorized into two classes: wavefront splitting (interfering two parts of a wavefront) and amplitude splitting (interfering two amplitude-split wavefronts). In our setup, a fully automated 193 nm Microstepper “Amphibian” with Talbot type prism amplitude splitting interferometer has been built previously, shown in Figure 7 [89]. Using a chromeless phase mask, the two-beam interferometer can have various NA values up to 1.2 depending on the final prism design.

Beam expander, UV polarizer and Fourier spatial filter are employed to improve the beam uniformity, polarization state and spatial cleanliness, respectively. Reliable 45 nm half-pitch line-and-space patterns are routinely printed on this system. This tool has been serving as a low-cost alternative platform to study novel optical phenomena and evaluate new materials.

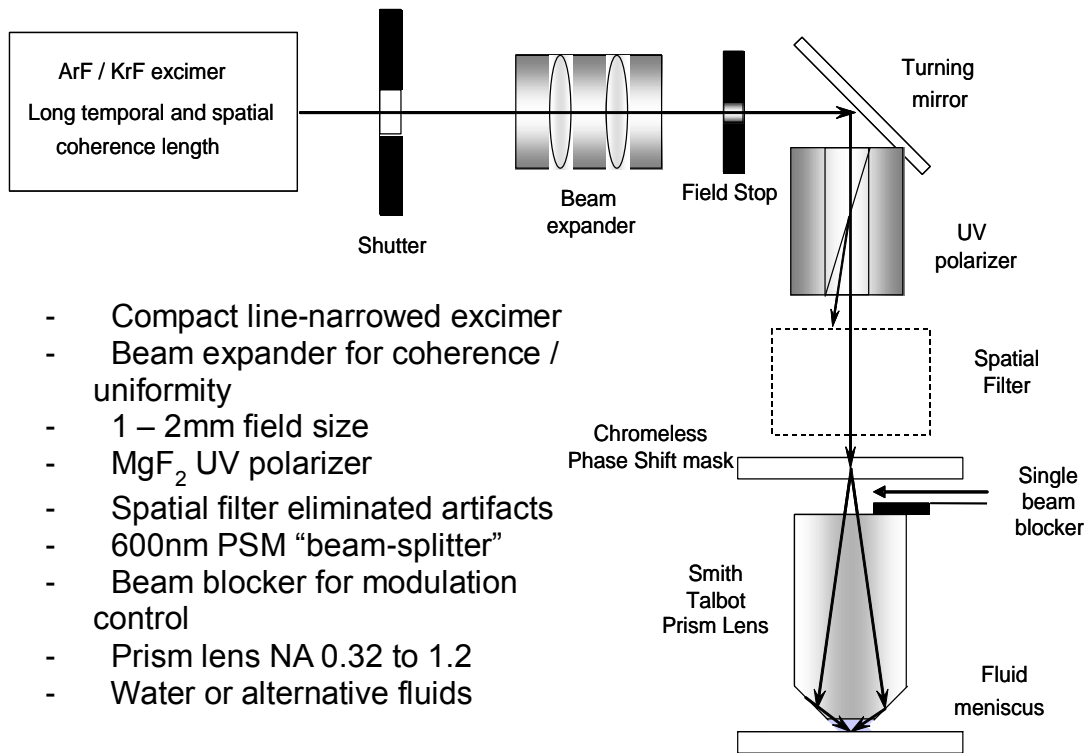


Figure 7. Schematic of the Smith Talbot interferometric lithography [89].

A bench-top version of this system, based on a similar configuration, is capable of more degrees-of-freedom and can support higher NA using either quartz or sapphire prism and high index immersion fluid. The angle of two reflecting mirrors together with the refractive index of the final lens material determines the system NA. Two setups including quartz and sapphire prisms are shown in Figure 8. Higher index lens materials

such as lutetium aluminum garnet (LuAG) has previously been explored; but found difficult to manufacture and control impurity levels [90].

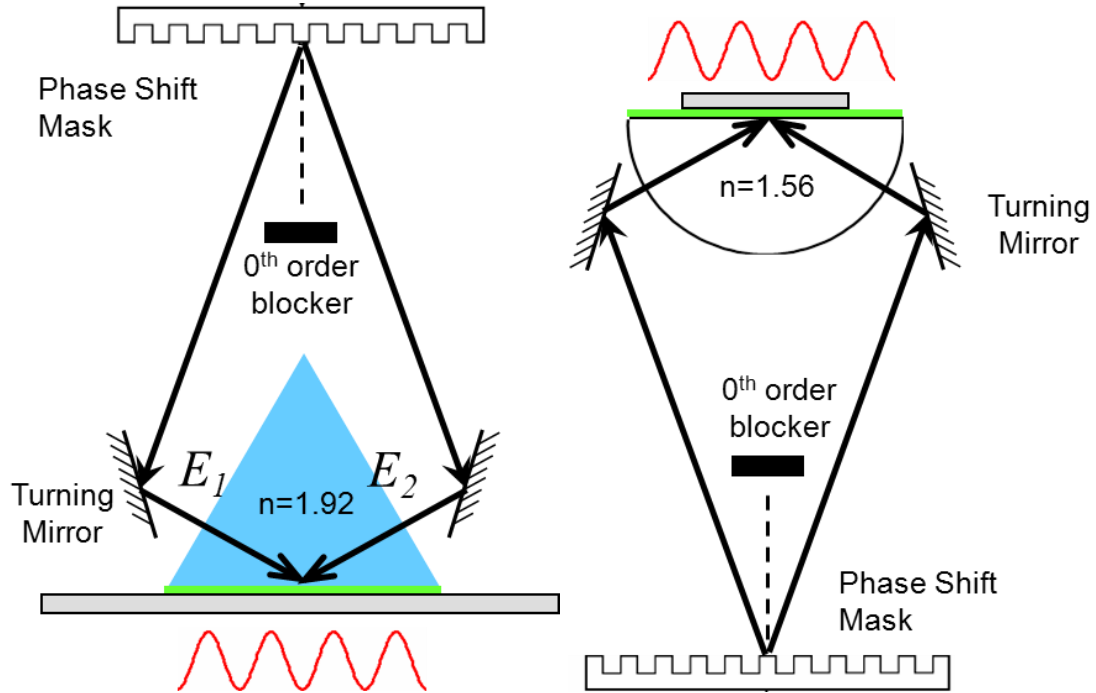


Figure 8. Schematics of two prisms used in the bench-top system. Left: sapphire prism; Right: quartz half-ball prism [87].

### 2.1.2 Pitch dependence

The final printed pattern resolution on the wafer is dependent on the NA ( $n \cdot \sin(\theta)$ ) achievable with the system. As depicted in Figure 9, larger angle of incidence (oblique/grazing incidence) leads to finer printed patterns by pushing  $\sin(\theta)$  to its numerical limit of 1. By adjusting and aligning the turning mirror angles, NA can be varied to achieve a desired pitch value. The highest NA; however, is limited by the lowest refractive index of any of the materials in the imaging stack\*. This is to guarantee

\* Note: this statement is only valid in the context of far-field imaging. We will see how this requirement becomes obsolete when considering evanescent imaging in Chapter 3.

the continuousness of wave propagation in the far-field. Figure 10 shows the typical imaging stack observed from the final prism down to the substrate.

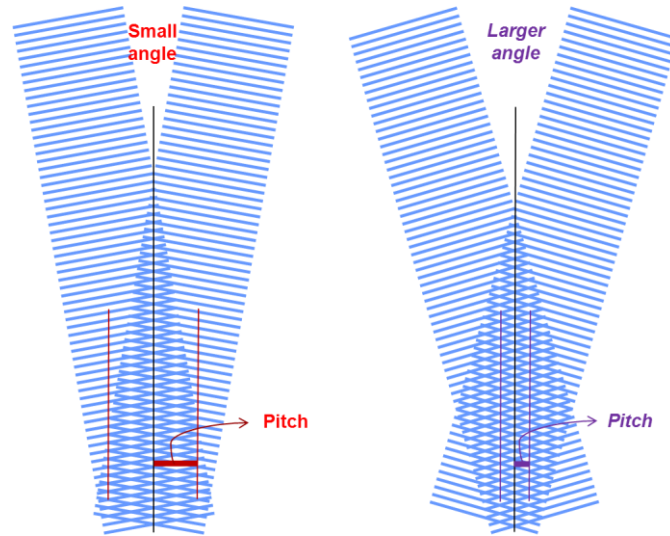


Figure 9. Pitch dependence on interference angle. Larger angle results in finer repeated patterns.

Taking practical material refractive indices into consideration, see Figure 10, the lowest refractive index material exists in the gap between the prism and top-coat/resist. ( $d_1$  is on the order of millimeter). This has led to the development of Gen-1 immersion lithography, by replacing air ( $n_1=1$ ) with water ( $n_1=1.44$ ) as the immersion fluid [91]. Water immersion lithography was successful, but it was only capable of 1.35 NA imaging. Gen-2 immersion fluids were then intensively investigated aiming at refractive indices greater than 1.6 to scale NA up to 1.55, required for 32 nm device node. The exhaustive search identified materials such as decalin, bicyclohexyl, and water additives as possible candidates [92]. Practical considerations such as refractive index, absorbance, defectivity, fluid handling and recycling, contamination, viscosity, thermal stability, and scattering limit, need to be taken into account. This extension would also require using new high index final lens elements such as LuAG ( $n=2.14$ ) to replace quartz ( $n=1.55$ ).

While no fundamental showstoppers exist for Gen-2 immersion lithography, this technology was never commercialized because in competing with NGL, the marginal resolution improvement (14%) hardly justifies the development cost for one device node.

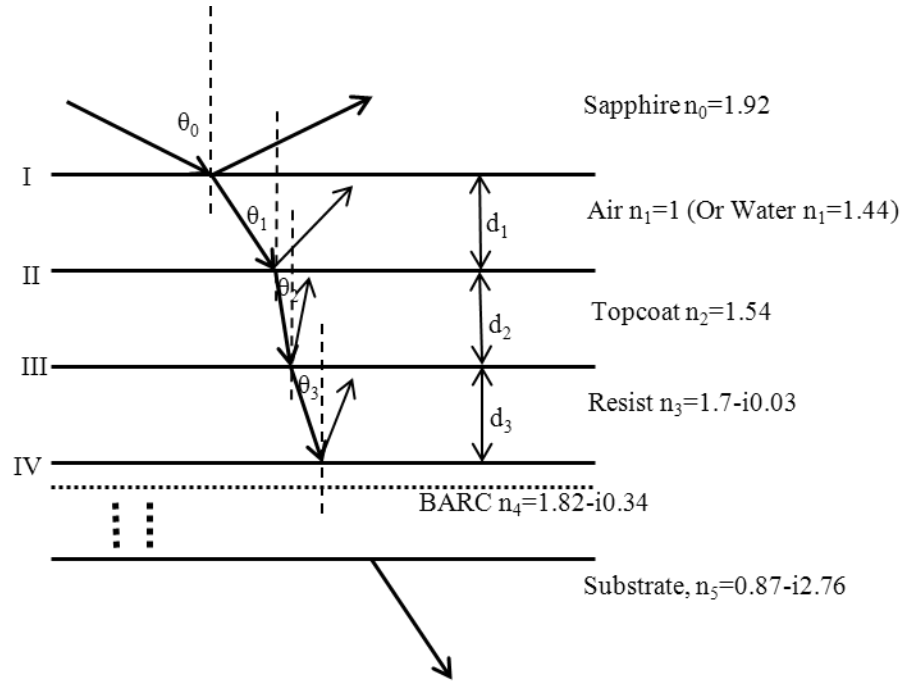


Figure 10. Wave propagation (reflection and refraction) through the imaging stack.

More ambitious development efforts were then devoted to develop Gen-3 immersion fluids with index larger than 1.8 to produce 1.7 NA immersion lithography. This poses a new array of material challenges ( $n > 1.8$ ) to the entire imaging stack including final lens, immersion fluids, resist and antireflective coatings [13]. Before the industry decided to cease Gen-3 immersion lithography development in 2008 (again due to timing and economic reasons), good progress has been made in developing final lens material (synthetic LuAG) [90] and high index ( $> 1.9$ ) inorganic resist materials [38], [39]. However, no Gen-3 fluids have been identified. Fundamental limitation exists in how much polarity and density can be introduced into organic molecules without

significantly degrading their transparency [93]. It is possible to add nanoparticles into solution but it requires extensive nanocomposite understanding [94].

To summarize, the bottleneck in developing high NA ( $>1.7$ ) immersion lithography currently lies in the lack of high index fluid material. While interference lithography shares most of the issues encountered in projection immersion lithography, it should be noted that the birefringence requirement in projection lens is greatly relaxed in IL because of the unidirectional TE polarized dipole. For this reason, the otherwise unsuitable sapphire (birefringence  $8 \times 10^{-3}$  @193 nm) prism becomes the workhorse for extremely high NA IL imaging.

### 2.1.3 *Coherence, field size and defects*

Due to the lack of well-defined energy level at ground state and short life time at excitation state, excimer laser is inherently poor in both temporal coherence and spatial coherence. Linewidth narrowing module consisting of dispersive prisms and gratings improves temporal coherence by orders of magnitude. State-of-the-art projection system employs excimer laser source with 0.4 pm linewidth centered at 193 nm. The poor spatial coherence, on the contrary, is used to the advantage of incoherent imaging to improve resolution and to avoid interference artifacts such as speckle.

IL poses high requirements on both temporal and spatial coherency [95]. Coherent IL imaging produces uniform, high contrast patterns across a large field. In our IL setup, the interference fringe pitch is dependent on the wavelength  $\lambda$ , the refractive index of the final lens material  $n$ , and the incident angle  $\theta$  which in turn depends on the first order diffraction angle  $\alpha$  and mirror tilt angle  $\beta$ . This relationship is expressed as:

$$p = 1/2n[\cos(2\beta)\frac{1}{p_g} + \sin(2\beta)\sqrt{\frac{1}{\lambda^2} - \frac{1}{p_g^2}}] \quad (2.1)$$

where  $p_g$  is the grating pitch. This equation reveals the pitch dependence on the wavelength. Finite spectral linewidth leads to the interference of two or more pitches in the aerial image and is detrimental to the field contrast. The resulting beat period  $L$  from the interference of two adjacent wavelengths has been derived as:

$$L = l_c / 2n\sin(2\beta)\cos\alpha \quad (2.2)$$

where  $l_c$  is the temporal coherence length. Converting the beat period to more perceivable contrast, we have field contrast as a function of the distance  $x$  from the center field:

$$\text{Contrast} = |\cos\{\pi x / L\}| \quad (2.3)$$

The contrast loss as a function of the distance from the center field is plotted in Figure 11. Depending on the tolerance set on the contrast, the corresponding maximum field size can be extracted from this plot. Clearly, with higher NA imaging, the maximum printable field size is likely to decrease.

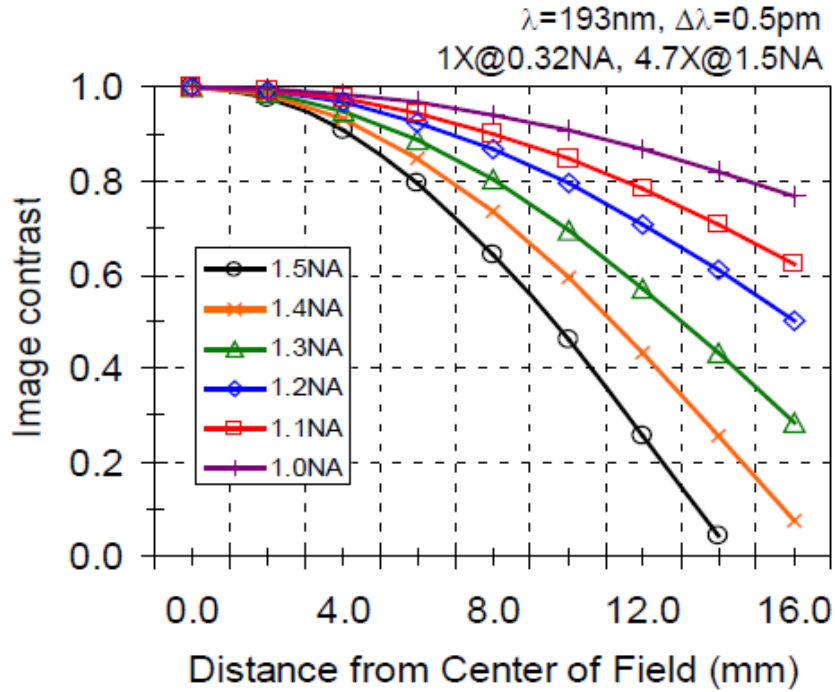


Figure 11. Image contrast loss as a function of distance from center of field [96].

The analysis above shows two clear paths to improve the field size. One way is to improve the temporal coherence of the laser source. Development of sub-200 nm wavelength solid state laser with 0.05 pm linewidth has been reported [97]. The other path is to use achromatic design in the interference system configuration. Referring to Equation 2.1, our setup can completely eliminate chromatic contribution by letting the reflecting mirror to be perpendicular to the mask ( $\beta=0$ ). The downside of doing this is to sacrifice the flexibility of the variable NA system with a fixed mask grating pitch. Various other achromatic designs have been reported and it is expected that adequate field size can be achieved with IL [78], [98], [99].

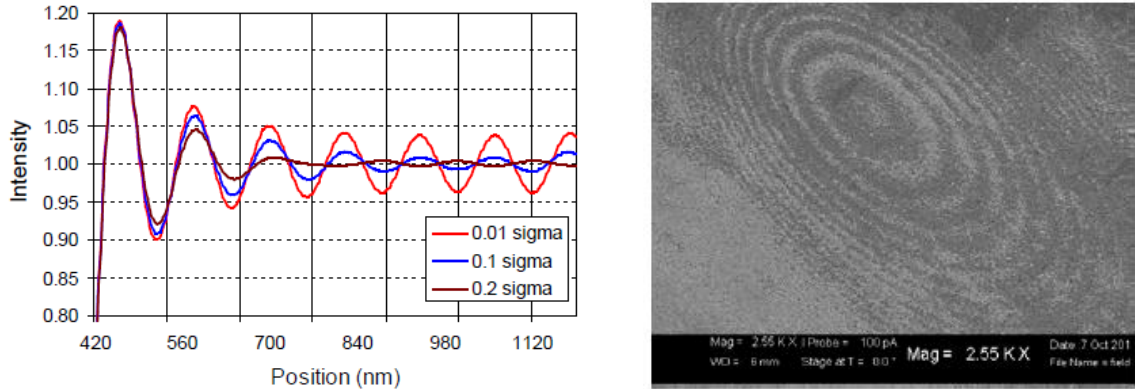


Figure 12. Field ringing effect from coherent diffraction from the edge of the circular field stop [96].

The requirement on spatial coherence is more complicated for IL. On one hand, highly spatial coherent beams are desirable to produce more overlap between interfering beams especially if there exists a focus offset. On the other hand, high spatial coherence is likely to introduce field ringing and speckle as the result of undesired random interference inside the coherent beam [100]. Figure 12 depicts the field ringing effect observed on the resist image as a result of highly spatial coherent beams diffracted by circular field stop edge. To remove these interference artifacts, spatial filter as close to image plane as possible needs to be employed. A beam with impurities (non-plane wave content, high spatial frequency content, etc.) will not be focused through the properly sized pinhole. The spatial filter corrects for the hyperbolic phase distortion induced by spherical wave and reduces field ringing and speckle [101].

## 2.2 Extending IL to sub-22 nm nodes

### 2.2.1 IL+DPL/MPL

To date, the highest reported optical IL resolution is 26 nm half-pitch at 193 nm wavelength [102] and 22 nm half-pitch at 157 nm wavelength [103]. In either case, such

resolution doesn't justify developing IL as a sub-22 nm lithography technology, especially considering the lack of high index materials in pushing for ultra-high NA.

The development and commercialization of double patterning lithography provides a viable path to extend IL into sub-22 nm regime. Most forms of DPL rely on optical projection lithography to create the first image (template) and a subsequent process step for pitch manipulation. With advanced device nodes, this first template image is likely to become ultra-regular, a concept called gridded design rules [104], [105]. The most important requirement for the dense line and space grating template is to have high contrast and large process window. Compared to projection lithography, IL produces the highest possible resolution grating of any optical lithography with a contrast close to 1. DOF, in theory infinite given a coherent source, can be quite large in practice with improved spatial coherence. In addition, the expensive masks and projection optics are eliminated in a conventional projection system, reducing the cost significantly. High index lens materials such as sapphire and LuAG, which are hard to produce in large diameter high precision projection optics, are once again viable. Troublesome optical proximity effects, mainly associated with 2D geometry such as line-ends, corners and pads, are minimized since only dense line and space grating is printed. Various RETs such as strong phase shift mask and off-axis dipole illumination with optimized polarization state can now be applied. Since only one duty ratio is defined, iso-dense bias is not required which simplifies the etch process and modeling. The above-mentioned advantages associated with IL make it a viable candidate in replacing projection lithography to image the DPL template. Together with DPL and even MPL, IL is now extendible to sub-22 nm nodes.

DPL arises from the fact that diffraction limit acts on the minimum pitch but not minimum linewidth. Practically, the minimum linewidth is only dependent on the resist property. Figure 13(a) shows an example of over-exposing a positive-tone resist to a linewidth well below the half-pitch.

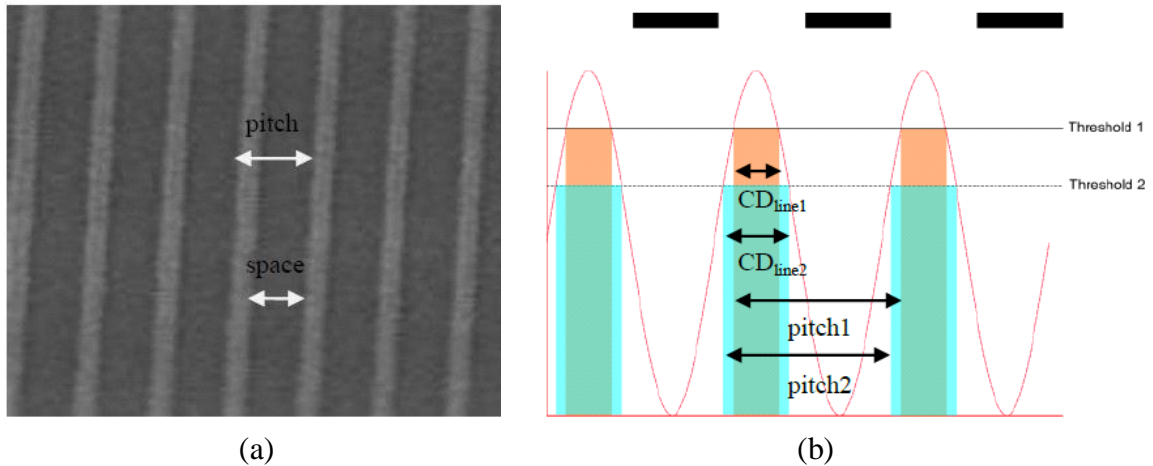


Figure 13. a. over exposing a positive resist results in line CD well below the half-pitch; b. sinusoidal aerial image showing different resist/developer threshold level affects the CD. The spatial period pitch remains the same.

The ability to manipulate the linewidth within a given pitch by thresholding the sinusoidal intensity distribution gives lithographers an extra option to break the minimum pitch criterion imposed by the diffraction limit. An example is given in Figure 13(b). The ideal form of pitch division (double patterning) requires a single exposure with dual tone development. Negative-tone developer, which dissolves the resist with intensity below the threshold, is possible for conventional chemically amplified resist [106]. The photochemically induced de-protection reaction changes the polarity or hydrophobicity of the resist polymer, which provides opportunity to engineer the developer solvent to have suitable properties [107]. If the dissolving threshold for the positive alkaline developer and the negative tone developer is different, pitch division results as only the resist with

dose in between two thresholds remains. 50 nm half-pitch dense lines were printed at 0.85 NA with this approach [108]. The schematic of the double development approach and imaging results are shown in Figure 14.

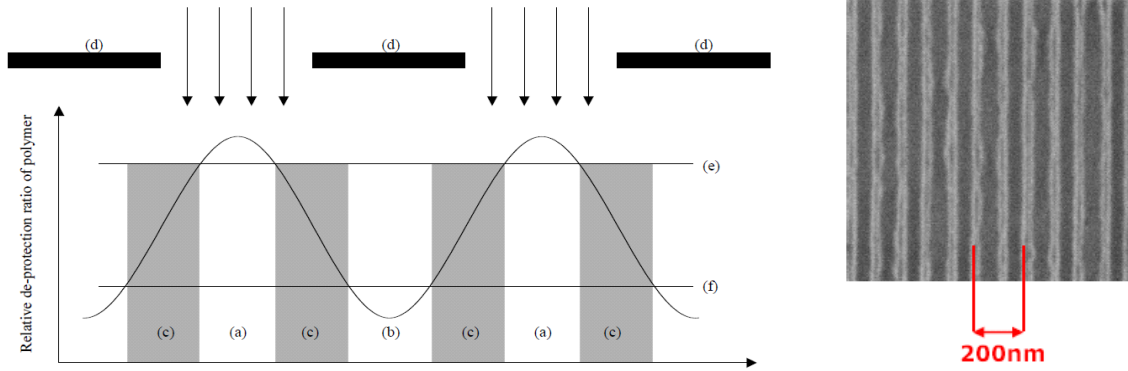


Figure 14. Left: illustration of pitch division through dual tone development process. The area above the threshold (e) set by the positive-tone developer and below the threshold (f) set by the negative-tone developer is removed [107]. Right: top-down SEM image of resist pattern with 50 nm 1:1 L/S features printed by the dual tone development process [108].

An alternative to achieve pitch division is to include a second exposure which interdigitates the first exposure. The sum of the exposures cannot improve the minimum pitch limit unless the photoresist response is not a simple addition of the two exposures ( $\cos^2 + \sin^2 = 1$ ). That is,  $\Delta(D_1) + \Delta(D_2) \neq \Delta(D_1 + D_2)$ . At least two approaches exist. One is true double exposure, where the engineered resist system responds to exposure non-linearly. Of the many categories of materials that respond in a non-reciprocal manner to dose, two have been intensively studied: simultaneous and sequential two-photon absorption (TPA), and reversible contrast enhancement layer (rCEL) [109], [110].

Since double exposure faces many challenges in designing non-conventional materials, the other more practical approach called DPL draws the most attention. In this

approach, the non-linearity in response is not induced photochemically but through an intermediate step between two exposures to freeze the pattern produced by the first exposure. Such an intermediate step can be hardmask etching, freezing material coating, thermal curing, UV curing, ion implantation, and negative tone or positive tone resist coating, etc. Depending on the nature of this intermediate process step, various DPL schemes exist including: LELE which corresponds to the hardmask etching approach, LFLE which requires certain form of freezing step, and freezing free litho-litho-etch (LLE) based on a resist on resist approach.

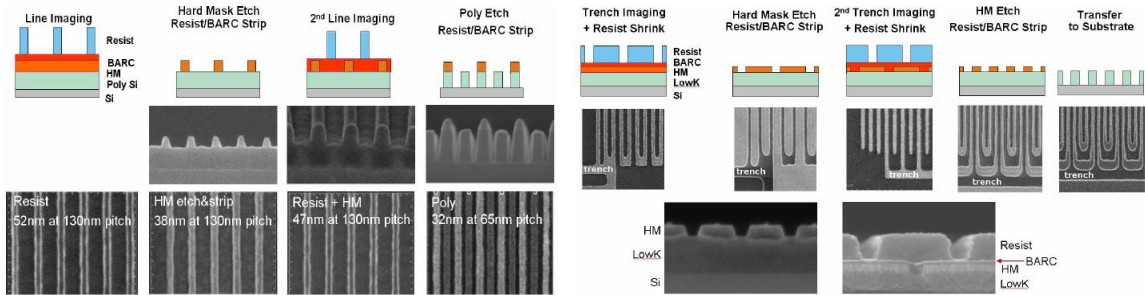


Figure 15. Positive-tone double line process (left) and negative-tone double trench process (right) used in a standard LELE double patterning process [111].

In the LELE approach, the patterned image by the first exposure is transferred and etched down to a sacrificial hardmask layer. By doing so, the first image is preserved in the hardmask. The subsequent BARC and resist coating then planarizes the film stack, followed by the second exposure. After development, the alternating hardmask line by first exposure and resist line by second exposure doubles the spatial frequency and awaits the final etch and pattern transfer. CD bias is usually required since the first etch step is prone to induce CD shrinkage, which in turn put more stringent requirements on process optimization, modeling and OPC. The process has been demonstrated by many at the

poly, metal, and contact levels, down to 32 nm half-pitch. The process is slightly different between double-line (positive, poly) and double-trench (negative, metal). Both process flows are shown in Figure 15. The major challenge comes from process control including alignment, interaction between two exposures, and the existence of four CD populations which complicates the CD uniformity (CDU) control. The alignment error between two exposures, given a 10% error budget for 32 nm half-pitch, requires less than 3 nm alignment error. Efforts are being devoted to ensure the requirement is met. The second exposure, differing from the first exposure in the underlying film stack, inevitably produces interactions between the two exposures. This interaction is reflected on the CD mean and CD  $3\sigma$  of the two exposures. Together with the alignment error, four CD populations ( $CD_{line1}$ ,  $CD_{line2}$ ,  $CD_{space1}$ ,  $CD_{space2}$ ) exist. Careful tuning of the process and improvement in alignment are needed to make a mature production level technology.

A similar approach, namely LFLE replaces the hardmask etch step with a freeze step (chemical crosslinking [112], thermal [113] or UV curing [114], ion implantation [115]) to preserve the first image. It is likely to be less expensive than the LELE approach since the wafer does not have to be taken off the litho track for etch. On the other hand, these systems are generally less robust since the interaction between the first and second exposures is less understood. Freezing typically grows the line CD and varies the resist height, which consequently reduces the process window [116].

A more interesting approach, freezing free litho-litho-etch, which eliminates the intermediate freezing step, makes use of different resist chemistry [117]. In the positive-negative resist on resist scheme, two solvent systems are engineered such that the first developed image is insoluble in the second solvent. The second negative tone resist

utilizes the dark mask application to prevent energy overlap between two exposures. However, negative-tone resist is notorious for its roughness when printing dense lines, as indicated by L2 in Figure 16(a) [118]. This leads to the design of a positive-positive resist on resist scheme. The two solvent systems are kept the same as in the positive-negative approach to minimize chemical impact to the first image. In order to prevent the first image from being developed by the second developer due to second exposure, the development rate of the first image is engineered to be extremely slow. This is done by setting the second PEB temperature to be 20°C less than the first PEB temperature and using a more photosensitive second resist. Small CD shift is likely to occur but may be corrected by OPC modeling. Imaging result of 32 nm lines on 128 nm double-pitch is shown by Figure 16 (b).

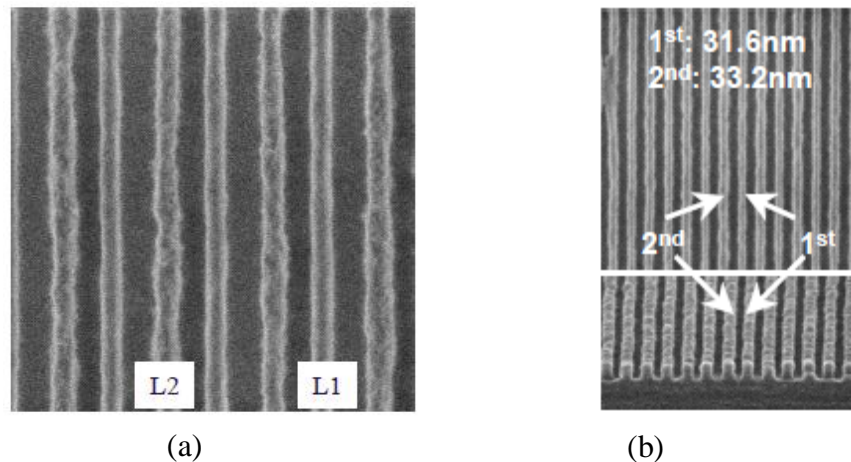


Figure 16. a. 44nm 1:1 L/S pattern obtained by positive and negative tone resists on resist double patterning. L2, which corresponds to the negative tone resist imaging, shows rough line edge [108]; b. 32 nm on 128 nm double pitch obtained from positive-positive tone resist combination [117].

All the double patterning approaches surveyed so far require two exposures. Consequently, the associated cost, intermediate freezing step, CD changes due to interaction between two exposures and alignment errors make these processes expensive

and difficult. The next approach called SADP, which operates under a totally different principle, avoids the above-mentioned limits and is being employed in production for 3x nm flash and DRAM.

The process flow, shown on Figure 17, involves: a. pattern the resist with twice the target pitch; b. expose or trim resist to 1:3 L/S; c. etch (pattern transfer) to a sacrificial template; d. form sidewall spacers at desired linewidth with nitride plasma enhanced chemical vapor deposition (PECVD); e. remove the original template; f. use the frequency doubled sidewall spacer as the hardmask to transfer etch down to the substrate.

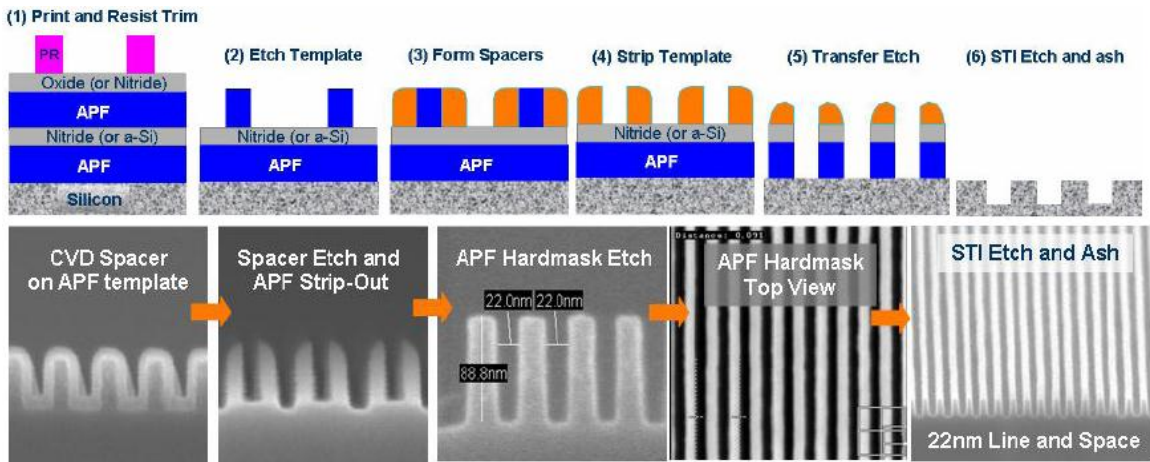


Figure 17. Generic process flow and SEM image snapshots for Applied Materials' positive tone self-aligned spacer double patterning [119].

A more aggressive processing scheme in extending optical lithography is to extend DPL to multiple patterning. While lithographers are understandably cautious of MPL because of the potential high cost and process complexity, not many patterning choices exist for sub-16 nm imaging. Carlson and Liu recently demonstrated iterated SADP from 600 nm half-pitch down to 40 nm half-pitch after four iterations [52]. To mitigate the cascaded pattern deformation due to individual spacer line-width variation

and sidewall angle, a multi-tiered sacrificial hardmask approach was adopted. Chen *et.al.* developed a triple patterning variation of the SADP process to relax the overlay accuracy requirement of critical layers and reduce their process complexity by using less masks [54]. As depicted in Figure 18, many other forms of MPL could be developed based on mix-and-matching existing DPL technologies, but it comes down to engineer the economically sound solution that produces the most viable process control.

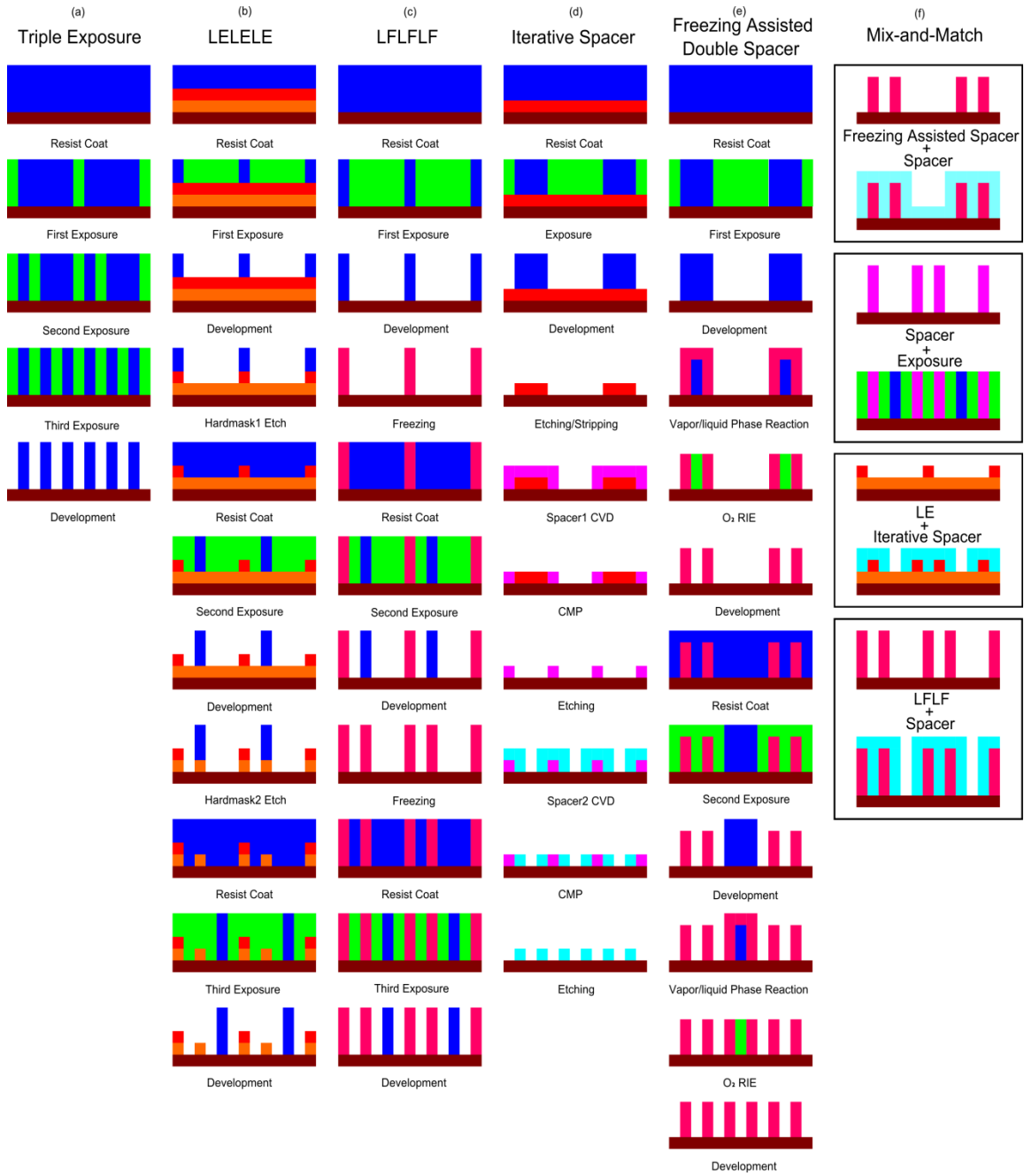


Figure 18. Detailed process schemes for higher order pitch division. a-c. triple patterning including triple exposure, LELELE and LFLFLF; d-e. quadruple patterning including iterative spacer and freezing assisted double spacer; f. mix-and-match process.

### 2.2.2 *IL+DSA*

Recent active research in directed self-assembly offers another insertion point for IL into sub-22 nm IC manufacturing. In a hybrid imaging scheme called “top-down” helps “bottom-up”, optical lithography is used to pattern the guiding template to direct the subsequent self-assembly process of block-copolymer [120], [121]. The orientation and placement of block-copolymer domains can be directed by topographically or chemically patterned templates. Therefore, IL becomes a great candidate to generate high-precision patterns, which is particularly important in the spatial registration and modulation of microdomains of block copolymers.

Whitesides and Grzybowski define self-assembly as the spontaneous organization of materials into regular patterns without human intervention [122]. In fact, biology has abundant examples of complex nano-scale structures (proteins, DNA, peptides, etc.) formed by self-assembly. Block copolymers consisting of two or more chemically immiscible molecular blocks have been extensively investigated as an excellent self-assembly material. Upon heating, amorphous block copolymers comprising blocks such as polystyrene (PS), poly(methyl methacrylate) (PMMA), poly(ethylene-alt-propylene) (PEP), or poly(vinylpyridine) (PVP) microphase segregate into microdomains (5-20 nm in size) to reduce the interfacial energy, due to the immiscibility of the chemically distinct constituent blocks and the confinement of covalent bonds. A variety of morphologies exist ranging from spherical to cylindrical (2D contact holes and vias) to lamellar (1D line-and-space), by varying the chemistry [123].

To achieve long-range order with the self-assembly process, the substrate needs to be properly patterned either topographically or chemically. Graphoepitaxy techniques use

topographic relief features much greater in length scale than the microdomains to induce single crystallinity which is essential for the epitaxial growth of the overlying block copolymer film [124]. In general, the graphoepitaxy process can be summarized as: (a). pre-treating the substrate to provide energetically neutral surface to align the lamellae perpendicular to the substrate; (b). pattern the substrate with periodic structures so that the sidewalls of the trenches are selectively wetted; (c). spin-cast the block copolymer and self-assemble with baking or UV curing; (d). selectively remove one domain by chemical solution or reactive ion etch (RIE). While defect free microdomains are expected when the periodicity of microdomains matches the width of the topographic guiding pattern, high frequencies line patterns occur by subdividing larger scale lithographic structures into sub-lithographic units. This process is depicted in Figure 19.

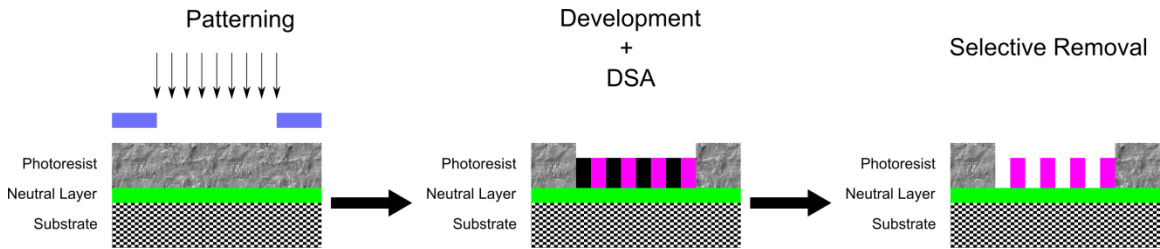


Figure 19. Conventional graphoepitaxy DSA process using positive-tone photoresist.

Chemical epitaxy DSA process works on controlling the interfacial interactions between the block copolymer and chemically nanopatterned surfaces [125]. Compared to graphoepitaxy, chemical epitaxy DSA process induces higher degrees of ordering perfection with less surface real-estate but requires additional processing. In a conventional pattern-first, neutralization-last process, a chemical brush is applied to neutralize the patterned geometry followed by a lift-off step. This process scheme is shown in Figure 20.

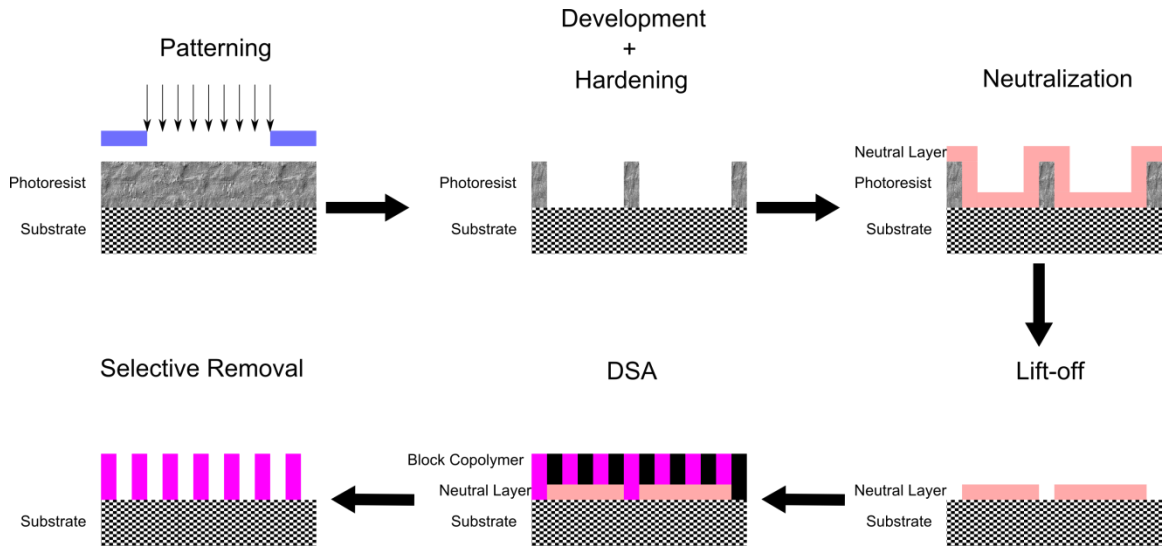


Figure 20. Conventional chemical epitaxy DSA process using pattern-first, neutralization approach.

### 2.2.3 Mask trimming considerations

One difficulty in extending IL to IC manufacturing is to re-work the single linewidth periodic patterns into usable circuit. While many forms of mix-and-match exposure schemes have been proposed in the past, it is not until the recent development of SADP and GDR that draws more attention to develop IL trimming [79], [126]. Bencher *et.al.* demonstrated various device layouts down to 16 nm using the line-and-cut approach, shown in Figure 21. As many as 5 additional masks and lithography steps are required to reroute the IL patterns. In SADP case, for each single line in the original layout there are two lines formed on both sides (spacers), which ultimately form a closed loop at the line-ends. An example of closed loop line-ends is given in Figure 22. Therefore, a second trim mask needs to be applied to open the line-ends. Moreover, SADP-produced sidewall spacers contain only one linewidth, determined by the sidewall spacer width. This is often undesirable since circuit designers tend to use multiple linewidths or even complex 2D geometries. A third pad mask is then applied to

accommodate such needs. Since the trim and pad masks are typically less demanding in resolution, those lithography steps can be accomplished in a dry scanner from an older device node to reduce the cost. The overlay situation among the multiple trimming masks is expected to be critical in advanced device nodes. Sub-3 nm overlay is required if overlay is assumed to take 20% of the CD budget. Another important consequence of the multiple mask/litho steps is that sophisticated EDA tool is required to optimize the three mask combinations.

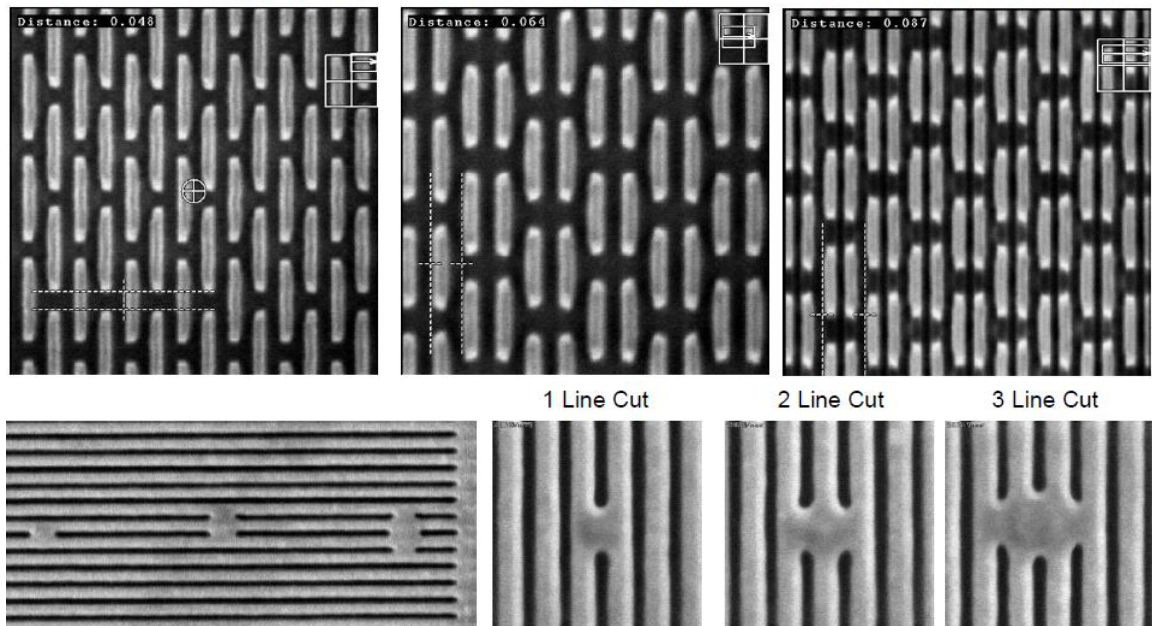


Figure 21. Upper: SEM snapshots of GDR lines and cuts patterns including 35 nm half-pitch DRAM (left), 32 nm half-pitch SRAM (center) and 22 nm half-pitch SRAM (right); Lower: 26nm half-pitch damascene trench patterning demonstration for 16nm logic node GDR [127].

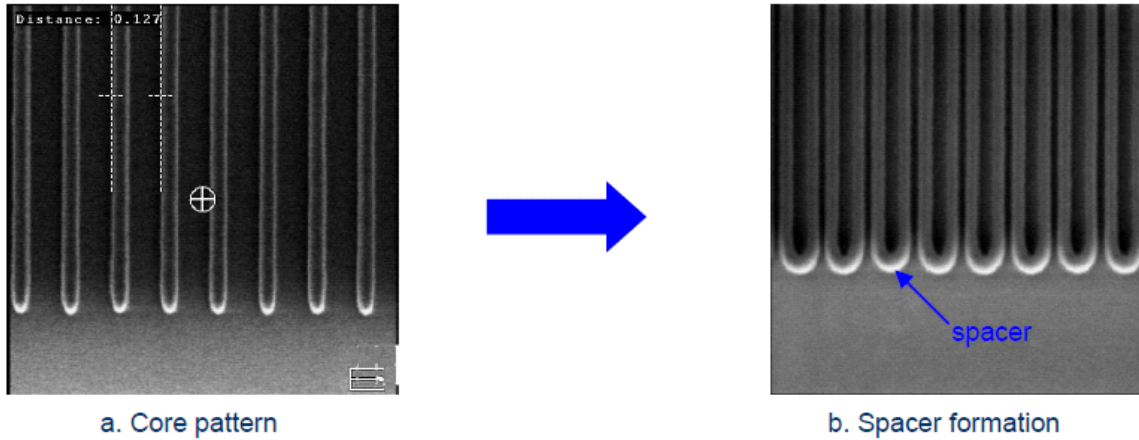


Figure 22. SEM images showing spacer formation after defining the core pattern [128].

### 2.3 IL limitations and paths towards manufacturing

IL provides an inexpensive, large area, large depth of focus technique for fabrication of high-resolution periodic nano-scale features. Despite the proposition for potential template IC patterning, IL found most use in serving as laboratory test-beds for material evaluation, and limited commercial applications in printing optical gratings and photonic crystals. The path towards manufacturing integration requires full-field exposure, resolution enhancement and new circuit design library.

A stable, uniform, high power, long coherence length uniformity solid state laser source coupled with metrology and possibly adaptive optics design that control fringes over full-field needs to be developed. Alternatively, scanning beam IL which stitches together small fields by synchronizing optical phase with stage scan may provide another path.

IL in high volume manufacturing would need to be capable of  $NA > 1.35$ . With the unsuccessful development of high index materials, the resolution enhancement technique proposed in this thesis, namely perturbing the ultra-high NA evanescent field

information, may well be the only viable optical approach. The challenge becomes to design and operate an imaging system in the sub-100 nm near-field scanning mode.

In the hybrid lithography approach where IC patterns are formed by “trimming and stitching” IL-produced grating pattern, new design library needs to be established to convert most random 2D structures to regular 1D designs. The associated cost issue, process complexity, 4 nm trim overlay, and lithography tool matching still remain to be addressed.

---

## 3. EVANESCENT WAVE LITHOGRAPHY: THEORY AND STATIC IMAGING

---

### 3.1 Introduction

The challenges in achieving  $>1.35$  high NA IL imaging mostly lie in the lack of non-absorbing high index fluids and lens materials. The need for high index materials to enable higher NA imaging is based on the assumption of the constant optical invariant imposed in far-field imaging. This assumption, however, breaks down in near field imaging when the wafer plane is brought into close proximity to the final lens element.

In this chapter, an approach is described to allow for imaging up to 1.85 NA using existing lens materials (quartz and sapphire) by employing evanescent wave optical effects at the imaging plane. The physical limitations of imaging imposed by the refractive indices of the materials, *i.e.* optical invariant, were surpassed through the interference of evanescent waves at near fields. This has allowed for the imaging into photoresist of half-pitch resolution below  $\lambda/7$ . A special situation where imaging at a system numerical aperture above resist refractive index is discussed. Lithography results are shown using image media including air, water, and a high refractive index fluid together with systematic gauge control to determine gap requirements and tolerances to achieve adequate image contrast in resist. Gauging methods include both optical and mechanical approaches to achieve nm level gap control. It is found that gap depths as large as 50 nm can be tolerated using this approach, well beyond the levels associated with alternative high resolution approaches such as those using surface plasmons [129].

## 3.2 Evanescent wave lithography

### 3.2.1 Total internal reflection and evanescent field

Consider a simple reflection/refraction interface where light is incident from high index medium to a low index medium, the refracted field is expressed as:

$$\vec{E}_t = \vec{E}_{ot} \cdot e^{i(\vec{k}_t \cdot \vec{r} - \omega t)} \quad (3.1)$$

If we choose the coordinate system such that

$$\vec{k}_t \cdot \vec{r} = k_{t_x} \cdot x + k_{t_y} \cdot z \quad (3.2)$$

It is straightforward to derive

$$k_{t_x} = k_t \sin \theta_t, \text{ and } k_{t_z} = k_t \cos \theta_t \quad (3.3)$$

In case of TIR in which the incident angle is above the critical angle, we have  $\sin \theta_i > n$ , where  $n = \frac{n_t}{n_i} < 1$ . Employing Snell's law  $n_i \sin \theta_i = n_t \sin \theta_t$  and substituting  $\sin \theta_i$  for  $\sin \theta_t$  and  $\cos \theta_t$  in Equation (3.3), we get

$$k_{t_x} = k_t \sin \theta_t = \frac{k_t}{n} \sin \theta_i \quad (3.4)$$

and

$$k_{t_z} = k_t \cos \theta_t = \pm k_t \sqrt{1 - \sin^2 \theta_t} = \pm k_t \sqrt{1 - \frac{\sin^2 \theta_i}{n^2}} = \pm i k_t \sqrt{\frac{\sin^2 \theta_i}{n^2} - 1} = \pm i \beta \quad (3.5)$$

where  $\beta = k_t \sqrt{\frac{\sin^2 \theta_i}{n^2} - 1}$ . Substituting Equation (3.4) and (3.5) to Equation (3.1) and (3.2), we get

$$\vec{E}_t = \vec{E}_{ot} \cdot \underbrace{e^{-\beta z}}_{\text{exponential decay in } z\text{-direction}} \cdot \underbrace{e^{i\left(\frac{k_t}{n} \sin \theta_i x - \omega t\right)}}_{\text{propagation in } x\text{-direction}} \quad (3.6)$$

In this situation, TIR generates an evanescent field which “propagates” along the interface but decays exponentially in the z-direction. The decay continues with distance and would theoretically lead to the existence of the evanescent field at any location, z. More practically, the penetration depth ( $d_p$ ) is defined as:

$$d_p = \frac{\lambda}{2\pi\sqrt{n_h \sin^2 \theta - n_l^2}} \quad (3.7)$$

where the energy in the evanescent field drops to a value of 1/e from that at z=0, defining its confinement to the sub-wavelength values. For transverse electric polarization (TE), the evanescent field is transverse to the direction of propagation; while for transverse magnetic (TM) polarization, separable components have a  $\pi/2$  phase difference. Though the amplitude of the evanescent electric field decreases with distance, the average energy in the field over time is zero.

It should be noted here that TIR is not the only method to generate an evanescent field. Light incident on a sub-wavelength aperture or a diffractive grating both gives rise to an evanescent field.

### 3.2.2 *Frustrated total internal reflection*

The non-traveling inhomogeneous evanescent field contains the high frequency information associated with the extremely oblique incident beam. If such information can be made to travel again, the highest achievable NA is then no longer limited by the immersion fluid but the final lens element itself. Detection or recording of the evanescent field is only possible if the field is perturbed into propagation, such as with a media of higher index, allowing for the escape and propagation of energy from illumination at

angles beyond critical, a situation called Frustrated total internal reflection (Frustrated TIR).

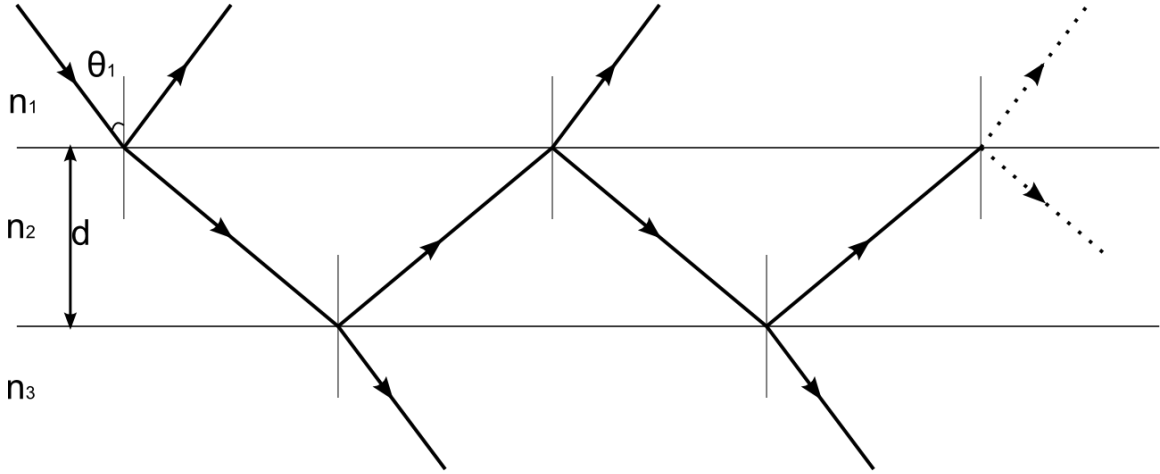


Figure 23. Reflection and transmission at a thin, homogenous film.

The classical treatment<sup>†</sup> of Frustrated TIR has been previously developed by including the imaginary phase change in Snell's law [130]. The reflection and transmission for a thin, homogenous film (as shown in Figure 23), results in a transmission coefficient  $T$  through the second medium given as:

$$1/T = \alpha \sinh^2 y + \beta \quad (3.8)$$

where

$$y = (d / \lambda)(n_1^2 \sin^2 \theta_1 - n_2^2)^{1/2} \quad (3.9)$$

For TE polarized light, which has greater applications in lithography,  $\alpha$  and  $\beta$  take on forms of:

<sup>†</sup> Quantum mechanical description of Frustrated TIR is analogous to optical barrier penetration/tunneling problem characterized by Schrödinger equation.

$$\alpha_{\perp} = \frac{\left[ \left( n_1 / n_2 \right)^2 - 1 \right] \left[ \left( n_3 / n_2 \right)^2 - 1 \right]}{4 \left( n_1 / n_2 \right)^2 \cos \theta_1 \left[ \left( n_1 / n_2 \right)^2 \sin^2 \theta_1 - 1 \right] \left[ \left( n_3 / n_1 \right)^2 - \sin^2 \theta_1 \right]^{1/2}} \quad (3.10)$$

and

$$\beta_{\perp} = \frac{\left\{ \left[ \left( n_3 / n_1 \right)^2 - \sin^2 \theta_1 \right]^{1/2} + \cos \theta_1 \right\}^2}{4 \cos \theta_1 \left[ \left( n_3 / n_1 \right)^2 - \sin^2 \theta_1 \right]^{1/2}} \quad (3.11)$$

Here,  $n_1$ ,  $n_2$  and  $n_3$  are the refractive index of three media, respectively,  $d$  is the thickness of the second medium,  $\lambda$  is the wavelength and  $\theta_1$  is the incident angle. An example is shown in Figure 24 where the TE transmittance is plotted as a function of varying gap thickness for different gap refractive indices. This plot indicates both sub-wavelength (<193 nm) gapping control and high index gapping material to get sufficient light transmittance into the third medium.

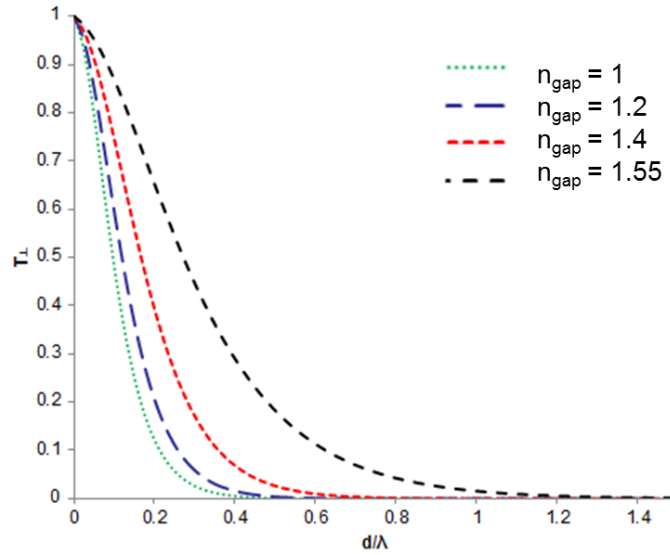


Figure 24. TE transmittance through gap thickness for different gap refractive indices.  $n_1=1.92$ ,  $n_3=1.7$ ,  $\lambda=193$  nm, incident angle at  $56^\circ$  corresponding to 1.6 NA.  $n_2$  is set to vary from 1 to 1.55.

### 3.2.3 *Simulation study*

While the derivation in the previous section yields an analytical solution to the Frustrated TIR transmission at a single surface, it is difficult to extend this approach to a situation for multiple absorbing thin films encountered in resist stacks. A multi-film matrix method [131] was adopted here where each film is represented by a  $2 \times 2$  characteristic matrix that takes into account the total electric and magnetic field and its boundary conditions. The resultant transmission or reflection of the system is characterized by the system matrix which is the product of the individual matrices. Using this approach, a Matlab program has been created to study the variables that affect transmission into a multi-film stack. Figure 25 shows the transmission through the evanescent gap as a function of gap thickness, numerical aperture, resist material and gap material in a lithographic imaging situation. In order to get the maximum intensity transfer to the photoresist, it is desirable to have a small gap, a high index non-absorbing gap material, and a high index resist material. This allows optimization between the materials and mechanics to achieve adequate throughput. It should also be noted here that the requirement for high index non-absorbing gap fluid is not the enabling factor encountered in high-index fluid immersion lithography; it is rather a parameter that helps relax the gapping requirement if needed.

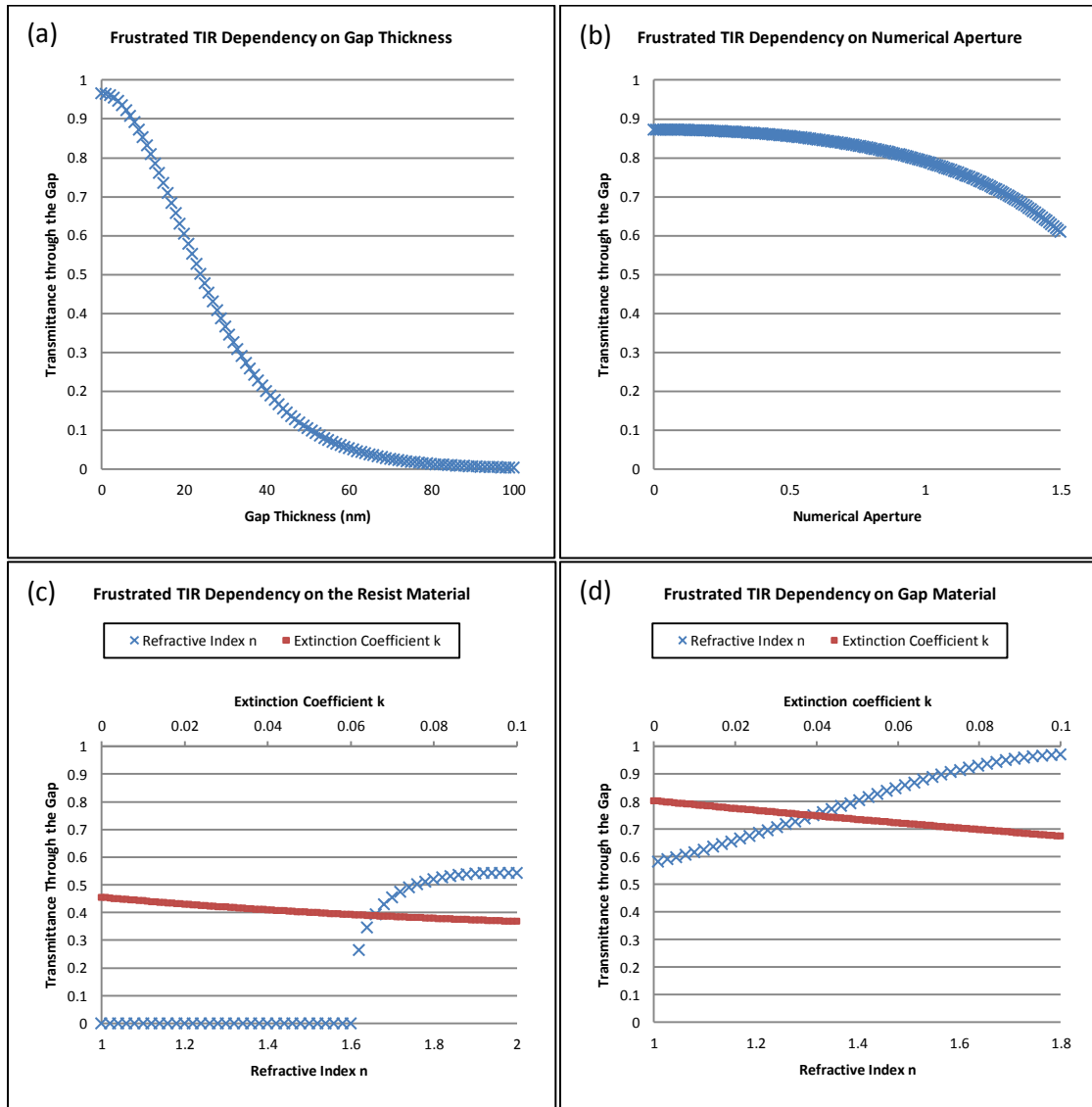


Figure 25. Frustrated TIR dependencies on (a) gap thickness, (b) numerical aperture, (c) resist material and (d) gap material. Simulation conditions are as follows except for the plots where the corresponding parameters are varied:  $\lambda=193$  nm; gap thickness  $d=20$  nm; system  $NA=1.6$ ; incident medium (sapphire)  $n_1=1.92$ ,  $k_1=0$ ; gap material (air)  $n_2=1.0$ ,  $k_2=0$ ; resist material  $n_3=1.7$ ,  $k_3=0.04$ . The only exception is for (c) where the extinction coefficient is kept at  $k_3=0$  when varying the refractive index  $n_3$ .

### 3.2.4 Interference imaging with EWL

A Matlab code called ILSim2 has previously been developed by RIT nanolithography group to simulate two-beam interference lithography aerial image [132]. Written with the same thin-film matrix approach, this program adds the vector interference theory to produce imaging results including evanescent field effects. Figure 26 shows the 2-D aerial image at the resist plane with parameters used in interference EWL where the air gap is set at 20 nm.

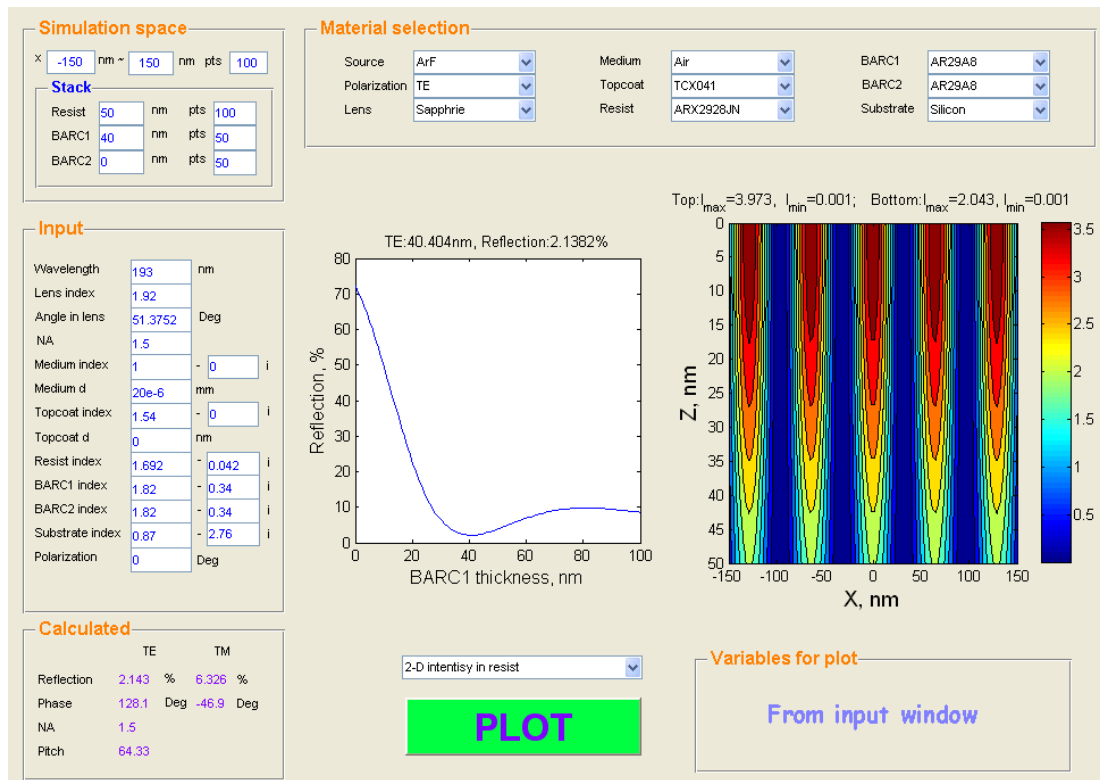


Figure 26. ILSim2 simulation on two-beam interference EWL. TE polarized 193 nm laser incident with 1.5 NA from sapphire ( $n=1.92$ ) through 20 nm air gap on 50 nm thick photoresist ( $n=1.692, k=0.042$ ). The BARC is optimized with 40 nm thickness to minimize reflection.

### 3.3 Static imaging approach and results

#### 3.3.1 Experimental setup

##### A. Exposure Apparatus

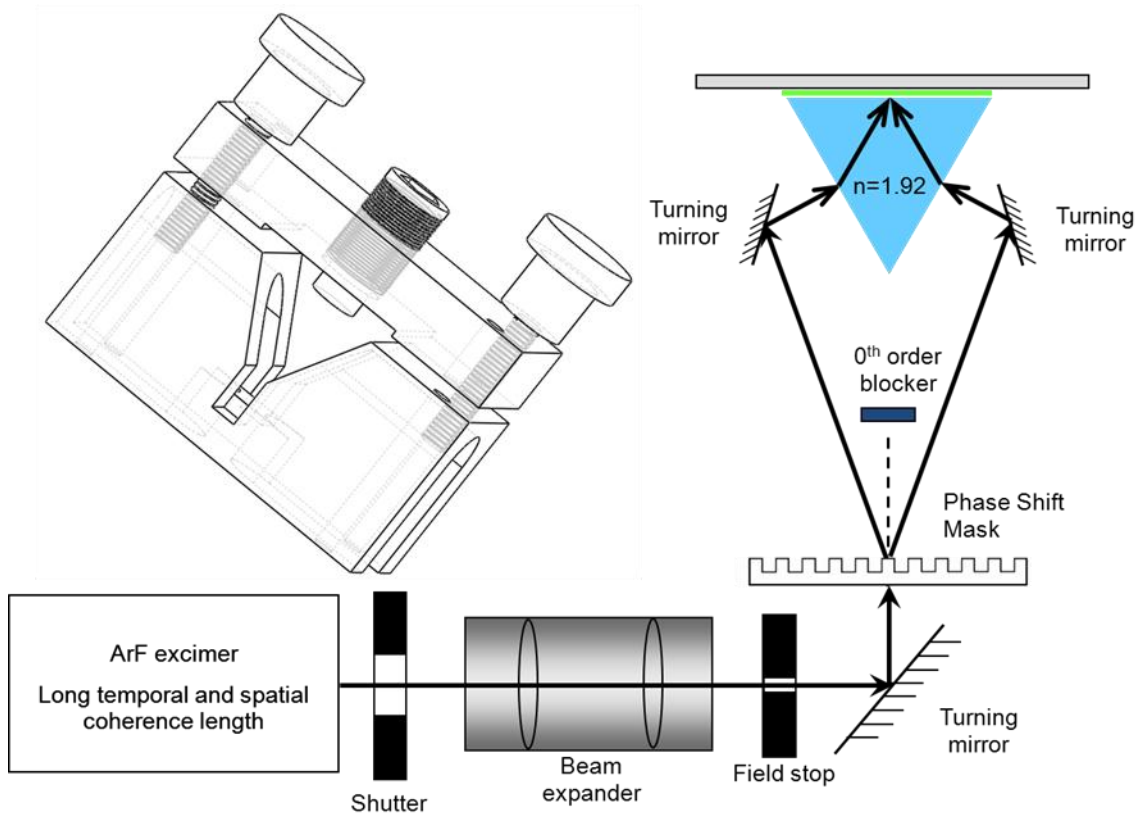


Figure 27. A two-beam Talbot interferometer with a two-piece modified prism holder.

A two-beam Talbot interferometer with a modified prism holder was used for the lithographic exposure, as shown in Figure 27. A detailed description of this system has been presented earlier [81]. 193nm ArF line-narrowed laser beam is expanded and linearly polarized. The Chromeless phase grating acts as a beam splitter, and only the 1st and the -1st diffraction orders are used as the interference waves. The final turning mirrors, together with the phase grating, define the arrival angle on the wafer. By changing the impinging angle, the resultant pitch size can be calculated.

The two-piece modified prism holder is designed to house an IR polished 10x10x10 mm 60° equilateral sapphire prism (refractive index  $n=1.9288$  @193 nm for ordinary ray). The bottom piece provides the support and openings for the beam paths while the top piece includes gap gauging via torque control. A calibrated torque wrench drives a nylon screw tip to provide intimate contact between the prism and the coated wafer sample. The exposure field is 4 mm in diameter, completely covered by the tip to ensure consistent gap thickness.

### *B. Gap Gauging*

Gap gauging was achieved by collecting the reflected laser beam from one arm of the interferometer. The right arm mirror was replaced with a pyroelectric photodetector (Coherent model J25LP-4). At a numerical aperture greater than the refractive index of the imaging medium, a baseline reading was taken as a reference. In this case, TIR resulted in maximum reflected energy. As the coated wafer sample makes contact with the prism, light can tunnel through the gap into the resist stack through Frustrated TIR, resulting in a decrease in the reflected energy. These reflected energy readings were taken at different torque values and normalized to the baseline reading. They were then plotted against the theoretical prediction of gap-transmission plot which takes into account the optical constants and thickness of prism-gap-resist stack, incident angle and polarization state. The gap is consequently gauged and controlled by monitoring the transmission and corresponding applied torque.

### *C. Experimental Approach*

The experiment was carried out exploring different resist film stack and imaging medium at different numerical apertures and gap thickness. At 1.50 NA, a resist stack

was used consisting of 40 nm JSR TCX041 ( $n=1.54$ ,  $k=0$ ) topcoat with 40 nm JSR ARX2928JN-7 ( $n=1.692$ ,  $k=0.042$ ) resist and 40 nm Brewer ARC29A-8 ( $n=1.82$ ,  $k=0.34$ ) BARC. Two imaging medium were tested at this NA including air ( $n=1.0$ ) and HPLC water ( $n=1.44$ ). At 1.60 NA, two resist stacks were used. The first stack consists of 40nm topcoat-less JSR AIM6023JN ( $n=1.705$ ,  $k=0.035$ ) resist with 96 nm AZ Krf-17B-100 ( $n=1.70$ ,  $k=0.10$ ) BARC. Three different imaging medium were tested including air, HPLC water, and cyclohexane ( $n=1.55$ ). The second resist stack consists of 40 nm JSR ARX2928JN-7 resist with 92 nm AZ Krf-17B-100 BARC. Only an air gap condition was tested. At 1.83NA, a 40 nm JSR ARX2928JN-7 resist with 64 nm AZ Krf-17B-100 BARC stack was exposed with an air gap only.

### 3.3.2 *Results and discussion*

Figure 28 shows the gap thickness measurement results and SEM photographs using both air and water as the gap medium at 1.50 NA. The measured transmittance data is referenced to simulation to calibrate the corresponding gap thickness. These measurements and dose-to-size information are summarized in Table I. Good agreement is found between the dose-to-size and measured transmittance, which validates the gap measurement and gauging repeatability. The air gap thickness varies from 20 nm to 70 nm with 0 to 65 inch-lbs of torque. The water gap thickness varies between 50 and 106 nm. The different torque-gap behavior is the result of their different hydrodynamic related material properties.

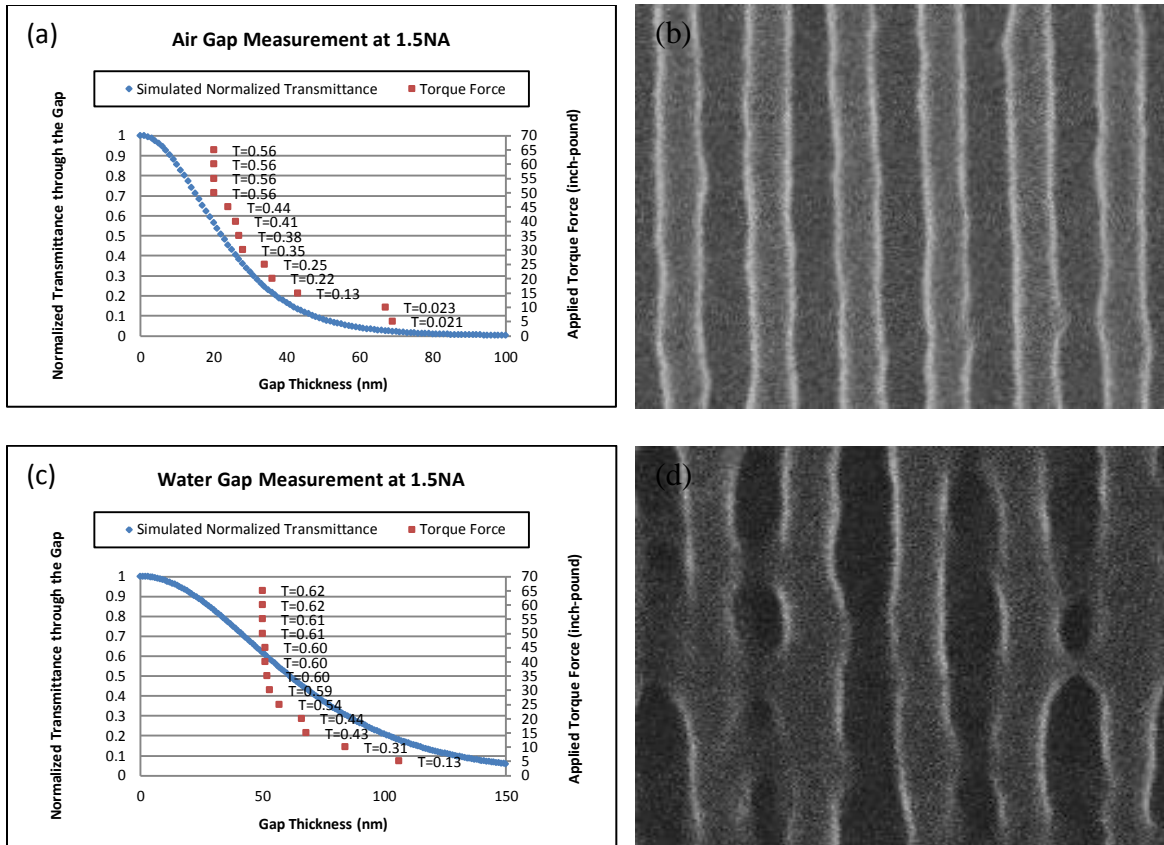


Figure 28. (a). (c): laser reflection measurement at different torque values when air and water are used as the gap materials, respectively. The measured transmittance  $T$  is referenced to simulated data to calibrate the corresponding gap thickness; (b). (d): SEM photographs showing 32 nm half-pitch line space grating using air and water as the gap medium, respectively. The torque for both cases is kept at 50 inch-lbs.

Gap Material	Torque		Gap	
	Applied (inch-lbs)	Normalized Transmittance	Thickness (nm)	Dose-to-size $E_{1:1}$ (mJ/cm <sup>2</sup> )
Air	50	0.56	20*	24
	50	0.61	50*	22
Water	20	0.44	66	30
	10	0.31	84	43
	5	0.13	106	102

Table I. Gap thickness measurement and corresponding dose-to-size information at 1.5 NA. \* indicates the minimum gap achieved with the gap material and resist stack.

At 1.60 NA, similar experimental results are obtained, shown in Figure 29. The minimum gaps are found to be 11 nm, 19 nm and 25 nm for air, water and cyclohexane, respectively. These gaps are associated with 75%-80% intensity transfer to the photoresist. While good imaging results are achieved, gap thickness in the sub 20 nm range could impose significant challenges in manufacturing control. If 50% transmission into the resist criteria was established as tolerable for high throughput imaging, the requirement on gap thickness can be relaxed, shown in Table II. The underlined values show the 50% corresponding gap thickness and dose-to-size which are extrapolated from the measured data (~75% transmission). It is found that a cyclohexane gap as large as 50 nm can produce 50% transmission into the resist with 8 mJ/cm<sup>2</sup> dose-to-size. Larger gaps are possible with Gen-2 (n=1.60-1.65) or Gen-3 (n=1.80) fluids as well as resist stack optimization.

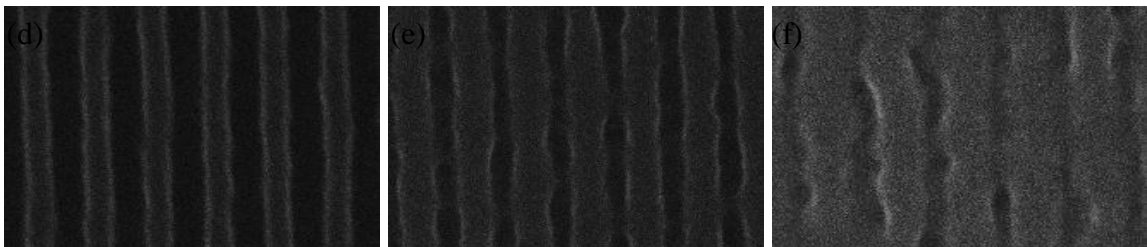
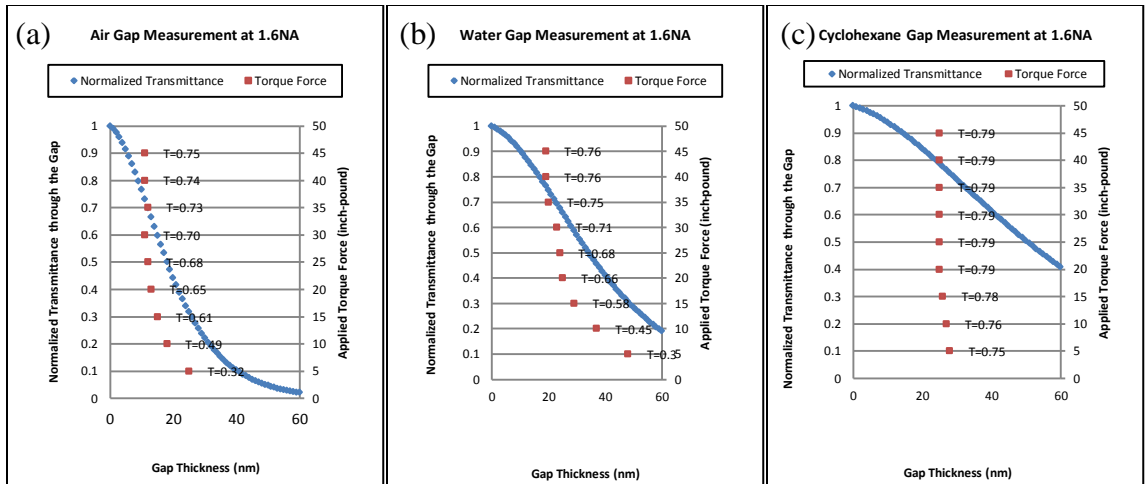


Figure 29. (a)-(c): laser reflection measurement at different torque values when air, water and cyclohexane are used as the gap materials, respectively. The measured transmittance  $T$  is referenced to simulated data to calibrate the corresponding gap thickness; (d)-(f): SEM photographs showing 30 nm half-pitch line space grating using air, water and cyclohexane as the gap medium, respectively. The torque for all cases is kept at 40 inch-lbs.

<b>Gap</b>				
<b>Gap Material</b>	<b>Torque Applied (inch-lbs)</b>	<b>Normalized Transmittance</b>	<b>Thickness (nm)</b>	<b>Dose-to-size E<sub>1:1</sub> (mJ/cm<sup>2</sup>)</b>
Air	40	0.74	11*	7
	-	0.5	<u>18</u>	<u>10</u>
Water	40	0.76	19*	7
	-	0.5	<u>35</u>	<u>11</u>
Cyclohexane	40	0.79	25*	6
	-	0.5	<u>50</u>	<u>9</u>

Table II. Gap thickness measurement and corresponding dose-to-size information at 1.6 NA. \* indicates the minimum gap achieved with the gap material and resist stack. Underlined values are extrapolated from the experiment and simulation.

In all the experimental conditions studied, the torque-gap response shows similar behavior. As the torque force is applied, the gap thickness reduces quickly and then gradually levels off to a minimum gap thickness. This minimum gap is dependent on both the resist film stack and gap material. It is suspected that hydraulic forces in the confined fluid bearing region prevents smaller gaps to be achieved. It is noted that cyclohexane shows a unique torque-gap response in which the gap reaches its minimum thickness the moment the torque force is applied. It is observed that the air gap imaging exhibits superior lithography quality compared to other gap materials, which is possibly due to interaction of hydraulic pressure on photoresist and imaging performance.

Imaging NA as high as 1.83 is also achieved with EWL. The results are shown in Figure 30. Imaging performance at 1.83 NA could be further improved with better dose

control because the process window is very narrow. Nonetheless, this result shows promise in achieving sub-32 nm patterns with single exposure optical lithography. With the development of high index high etch selectivity inorganic resist, very thin resist film (<30 nm) would make excellent candidate for >1.8 NA imaging.

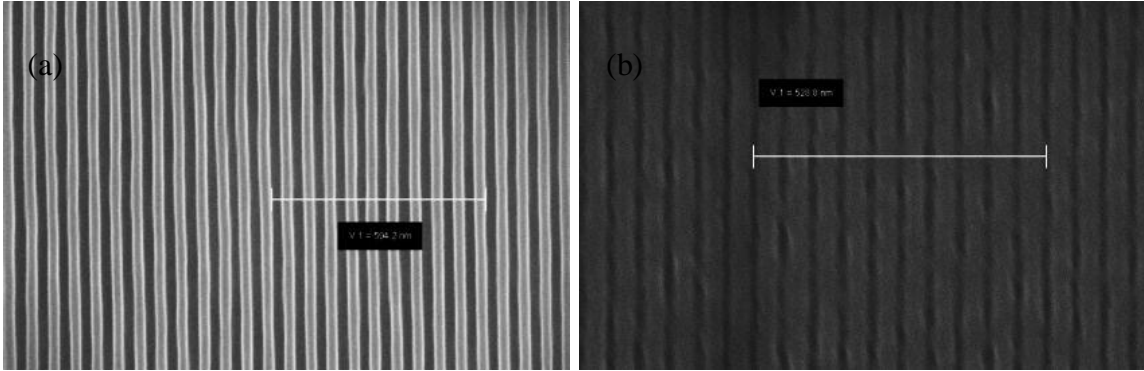


Figure 30. SEM photographs showing line space grating (a). 30 nm half-pitch (1.6NA); (b). 26 nm half-pitch (1.83 NA). Air gap is used in both cases. Torque is kept at 40 inch-lbs.

### 3.3.3 On $NA_{sys} > NA_{resist}$ Imaging

It has been shown previously that NA greater than the real part of the refractive index of the resist is attainable with evanescent imaging, and is experimentally confirmed in the 1.83 NA imaging condition ( $n_{resist}=1.7 < NA_{sys}$ ) [102]. To explain this phenomenon, Snell's law needs to be expanded to take into account refraction into an absorption medium such as photoresist [133]. The effective refractive index  $n_{eff}$  can be written as:

$$n_{eff} = \left\{ \frac{n^2 - k^2 + \sin^2\theta \pm \sqrt{(n^2 - k^2 + \sin^2\theta)^2 - 4[(n^2 - k^2)\sin^2\theta - n^2k^2]}}{2} \right\}^{1/2} \quad (3.12)$$

where n and k are the complex refractive index of the absorbing medium, and  $\theta$  is the incident angle. Similarly, the effective extinction coefficient  $k_{eff}$  is given as:

$$k_{eff} = nk / \left\{ n_{eff} \cos \left[ \arcsin \left( \frac{\sin \theta}{n_{eff}} \right) \right] \right\} \quad (3.13)$$

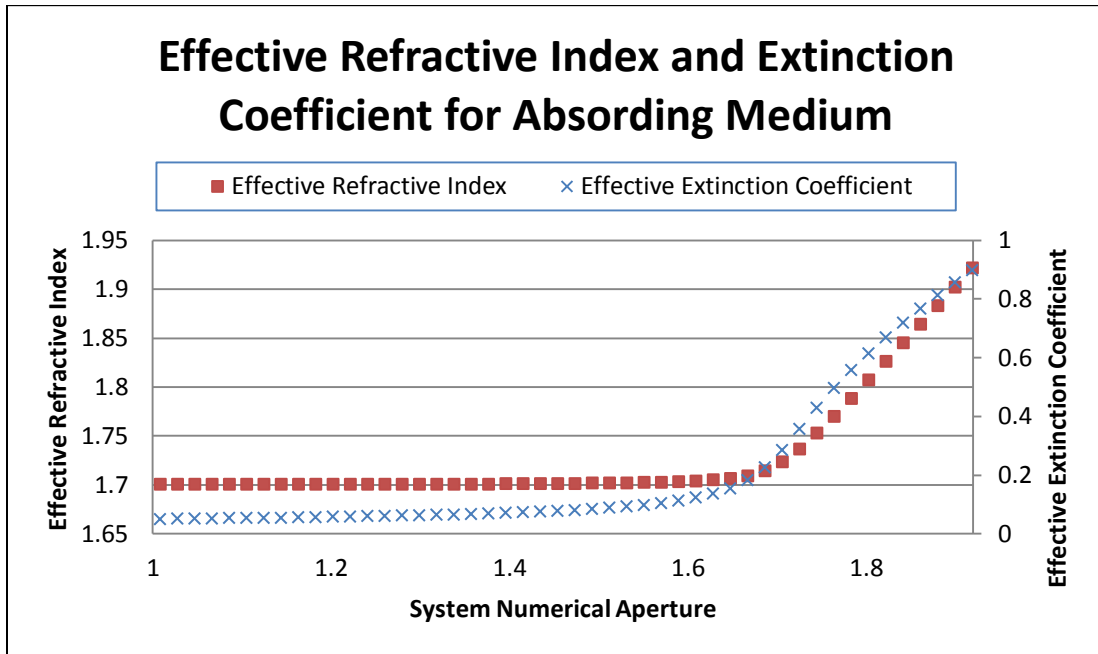


Figure 31. For an absorbing medium ( $n=1.7, k=0.04$ ), both the effective refractive index and effective extinction coefficient increases with system NA (incident angle) above the nominal refractive index. The net result is surface imaging on the top  $<20$  nm region. Light is incident from sapphire ( $n=1.92, k=0$ ).

Figure 31 shows a simulation scenario where light propagates from sapphire into photoresist ( $n=1.7, k=0.04$ ) with various incident angles. The effective refractive index of the resist increases at oblique angles well beyond 1.7, allowing light to penetrate into the photoresist at NA greater than 1.7. On the other hand, the effective extinction coefficient also increases significantly with the incident angle. The net result is surface imaging at NA exceeding the nominal refractive index of the resist.

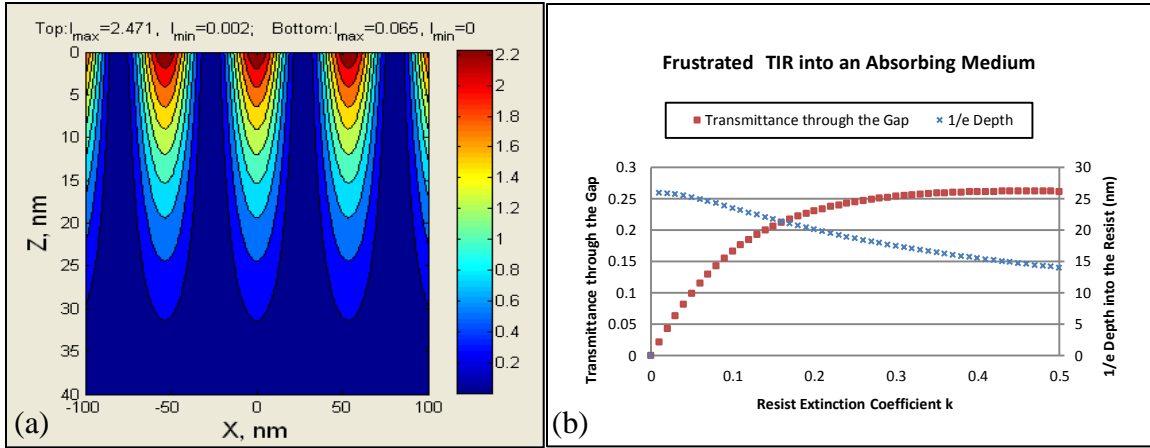


Figure 32. (a) resist profile simulation by ILSim2 at NA larger than the nominal refractive index of the resist; (b) Frustrated TIR transmittance through the evanescent gap and into the photoresist as a function of nominal resist extinction coefficient. System NA is 1.8. All other simulation conditions are kept the same.

This effect is simulated using ILSim2; results are shown in Figure 32(a). The surface imaging is confined in the top <20 nm region. Figure 32(b) illustrates the similar effect using the matrix method where light penetration through the evanescent gap is possible with slightly absorbing resist even though the system NA exceeds the nominal resist refractive index. However, with more absorbing resist, although more light gets through the gap, the skin depth into the photoresist decreases as the result of the increasing effective extinction coefficient. An optimum resist extinction coefficient exists to give maximum energy transfer into the resist. Recent development in metal plasmonic reflector offers an attractive solution to increase imaging depth [134].

### 3.3.4 Next generation resist research

The static interference EWL imaging has been used extensively as a test-bed for next generation resist developments [135], [136]. These developments have been focused in two areas: non-chemically amplified resist (non-CAR) to battle the deteriorating line-

edge roughness (LER) effect; and high index inorganic resist suitable for ultra-high NA imaging.

In a joint research project with Inpria Corp. and Oregon State University, we have experimented with peroxy modified forms of the materials such as zirconium oxide sulfate ZircSO<sub>x</sub> and hafnium sulfate HafSO<sub>x</sub> [39]. These materials provide many advantages with respect to both CARs and all other photo-patternable inorganic resists. These advantages include the tunability of the optical properties of the Metal-SO<sub>x</sub> resist platform at 193 nm, low LER, high etch resistance and the ability to access indices of refraction above 1.8.

The Metal-SO<sub>x</sub> materials are aqueous systems, which makes water immersion 193 nm lithography unsuitable to test the imaging performance of such resists at high NA. Formulating a water impermeable topcoat to meet requirements at both interfaces proves to be difficult. To test immersion capabilities and to avoid the need for a topcoat, static interference EWL experiments at 193 nm were performed on a range of HafSO<sub>x</sub>/ZircSO<sub>x</sub> formulations. Both air gap imaging and using cyclohexane as the immersion fluid were tested. Representative SEM images of 60 nm lines on a 60 nm half-pitch in ZircSO<sub>x</sub> exposed at a dose of 25 mJ/cm<sup>2</sup> are shown in Figure 33(a). However, lack of material candidates as bottom antireflective coating limited the imaging performance at ultra-high NA. Evidence for 40 nm half-pitch lines was observed in spite of this issue.

The Metal-SO<sub>x</sub> chemistry is also directly amenable to a negative-tone LFLE process. This process involves two consecutive lithographic steps and two resist coating steps. In the first lithography step, a resist layer is deposited, exposed, baked, and then

developed. A thermal freeze step follows to render the developed pattern insoluble in the second resist coat. In the case of Metal-SO<sub>x</sub>, a 5 min bake at 220 °C is adequate to lock in or “freeze” the pattern. After the 220 °C bake, Metal-SO<sub>x</sub> patterns have been transformed into dense oxides and are no longer soluble in resist or developer. A second lithography process can then be performed on top of the existing pattern. Finally, an etch step can be performed to transfer the doubly exposed pattern. Figure 33(b) shows a SEM image of the crosshatched patterns clearly revealing the 60 nm half-pitch line-space gratings.

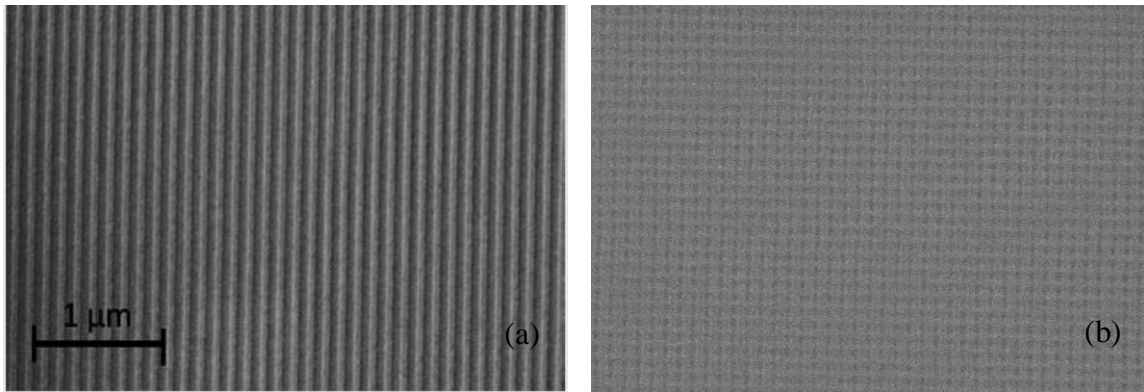


Figure 33. (a) 60 nm lines on a 60 nm half-pitch written in ZircSO<sub>x</sub> using 193 nm optical interference lithography at a dose of 25 mJ/cm<sup>2</sup>; (b) 60 nm half-pitch crosshatched patterns produced by static interference EWL imaging with LFLE double patterning process.

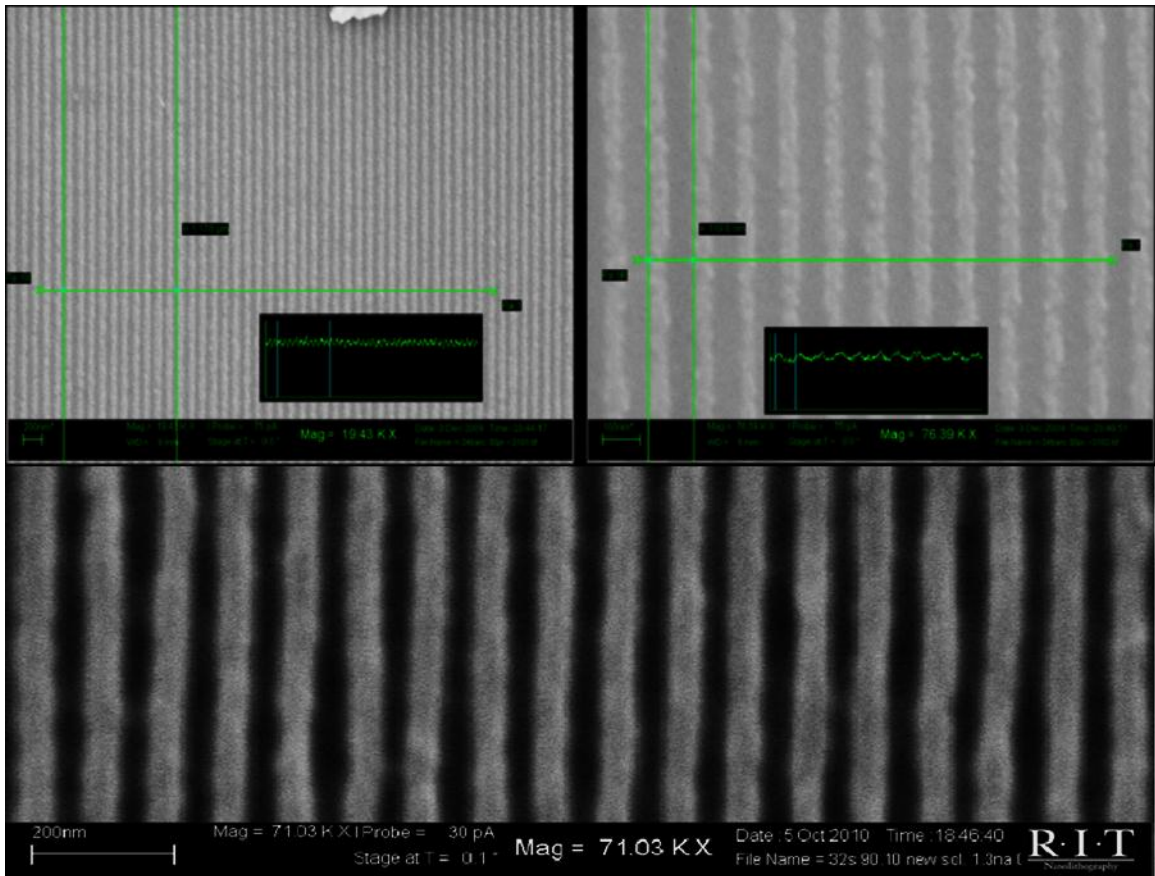


Figure 34. SEM images of patterns printed on the HfO nanoparticle resist using 193 nm static interference EWL: 60 nm half-pitch negative tone (upper) and 50 nm half-pitch negative tone (bottom).

In another research project conducted with Cornell University, Hafnium oxide nanoparticles are used as a core to build the inorganic nanocomposite resist [38], [137]. In the imaging experiments with static interference EWL, uniform thin films can be spin-coated on Si wafers using either PGMEA dispersions of the nanoparticles. The nanoparticle films with 2,2-dimethoxy-2-phenyl acetophenone (DPAP) as a photoinitiator act both as positive and negative tone photoresists. Films with the desired thickness are prepared and then baked at 130°C for 60 sec on a hot plate. After exposure, development in isopropyl alcohol or t-amyl alcohol gives a negative tone image. For the positive tone imaging, the film is baked after exposure (PEB) at 130°C for 3 min and then aqueous

tetramethylammonium hydroxide (TMAH) is used for the development. Since significant dark loss was observed during positive tone imaging, focus has been given to evaluate the negative tone mode of the resist. The films were coated on a bottom anti-reflecting coating (BARC) and tert-amyl alcohol was used as a developer. Figure 34 shows the SEM image of both 60 nm and 50 nm lines and spaces that were printed on the film. The film that was used was only 30 nm thick to minimize absorbance and reflection. Both air and purified Decalin as a gap material were evaluated.

---

## 4. DESIGNING A SCANNING EWL HEAD

---

The previous chapter presented the static interference EWL theory and experimentally demonstrated the near-field imaging resolution enhancement by gauging the evanescent gap. The static imaging system has been extensively used to examine new materials including resists and immersion fluids. The obvious limitation is that a small, 4-mm diameter imaging field is produced, dependent upon the laser spot size and gap control. Across the millimeter sized field, the line-space patterns are likely to be defective due to gap thickness variation caused by vibration, dust, surface imperfection and leveling.

In order to evaluate the possibility of extending interference EWL from laboratory prototyping to IC production, large field EWL tools need to be made. There are, in general, two approaches. The first approach is to build a large field (26 mm \* 33 mm) interference tool capable of near-field imaging. At current stage, this approach seems impractical primarily limited by the extreme requirement on laser coherence as mentioned in Chapter 2. The ability to control the gap uniformity across such a large field is also questionable considering the polished wafer surface roughness is on the order of 10 to 50 nm [138]. The second approach is to reduce the size of each individual imaging field and later stitch the many mini-fields together through scanning. In this chapter, we are going to present the design of the imaging head using this approach. We start by identifying the design tasks and system architecture in Section 4.1. The five key design components, including gap detection and measurement, imaging head design, prism

design and fabrication, servo control development, and scanning schemes, are detailed in Section 4.2.

## 4.1 System Architecture

### 4.1.1 *Design task identification*

To achieve the goal of evanescent wave imaging at sub-100 nm scanning height, the system we build includes the following functionalities:

- A. Gap detection and measurement: The system should be able to detect real-time gap height with fast response time and low noise.
- B. Feedback actuation: If the detected gap height is different from the set gap target, the system should include one or more actuation mechanisms to adjust and maintain a constant target gap height.
- C. Prism design and fabrication: The prism (final optical element) needs to be uniquely designed and fabricated to accommodate sub-100 nm gap imaging.
- D. Servo control: Sub-100 nm scanning needs to be automated in a control servo to achieve gap detection and actuation.
- E. Ultra-high NA interference imaging to produce uniform line-space patterns across the mini-field.
- F. Dynamic scan over an entire wafer surface and stitch together the many mini-fields.

#### 4.1.2 *System design overview*

There has been no previous report in developing a scanning imaging system using EWL. In a similar near-field imaging work, Zhang's group proposed near-field plasmonic lithography using a flying air bearing slider to maintain sub-20 nm air gap while the wafer spins [139]. This work differs from ours in that it uses plasmonics and requires wafer spinning which generates an air cushion to self-maintain the gap. In addition, it requires sophisticated air bearing surface design, and a micro-fabricated and focused ion-beam milled plasmonic lens array. Therefore, their imaging head design and application is significantly different from ours.

Some design concepts including mechanical flexure and leveling piezoelectric transducer can be found on the gap control system used in nanoimprint lithography processes. For the purpose of imprint lithography, it is important to maintain a nearly parallel gap about 200 nm between the template and substrate [140]. However, this design is different in not involving scanning and lithography imaging.

A more direct analogy can be drawn between scanning EWL imaging head and high density near-field optical disc recording system such as that proposed by Sony [141]. In this system, a conventional optical pick-up actuator (voice coil) with a solid immersion lens (SIL) is used to write or read pit patterns on a spinning optical disc. Disc rotation generates an air cushion and lifts the SIL a certain distance, effectively creating an air bearing surface. In some designs, the concepts of external air bearing, piezoelectric transducer, voice-coil actuator, servo control and near-field imaging lens design were developed to enhance system performance [142]. These concepts were incorporated into our scanning EWL design.

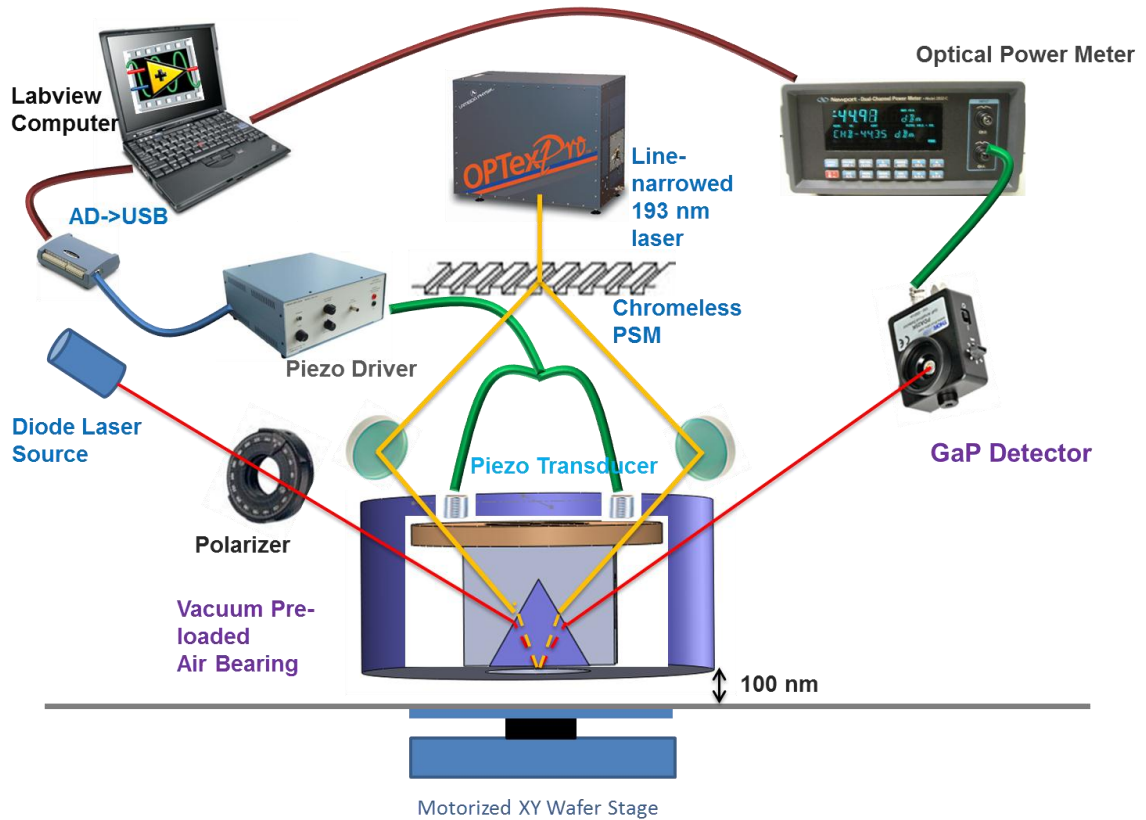


Figure 35. Schematic of the two-beam interference scanning EWL system.

Figure 35 shows the schematic of the overall system architecture. The system includes two major components. The first component is the 193 nm two-beam interference imaging system which consists of the line-narrowed excimer laser, essential imaging optics (polarization, beam expansion, spatial filtering, etc.) and final prism. The second component is the gap control system. This includes the gap detection system, and actuation mechanisms embedded in the imaging head and servo control system. In the rest of the chapter, each sub-component in the gap control system is described in detail.

## 4.2 System design considerations and implementations

### 4.2.1 Gap detection

Among many methods to detect gap height such as capacitive sensing [143] and white light interference [144], the total internal reflected power at the bottom of the prism (truncated cone with a small flat tip) is used as a gap error signal to control the gap between the wafer and prism's bottom surface.

Figure 36 shows the schematic of the detection method and the relation between the gap height and the total reflected power. When the incident off-wavelength laser beam (HeNe 632.8 nm) is focused on the high index sapphire prism from one arm, the above critical angle beam is reflected to the other arm. However, under the near field condition when prism comes closer to the wafer surface, part of the reflected beam penetrates the prism bottom surface as an evanescent wave, thus reducing the reflected beam power. Hence, by maintaining the reflected power at a constant reference level, the gap can be kept constant in the near field region.

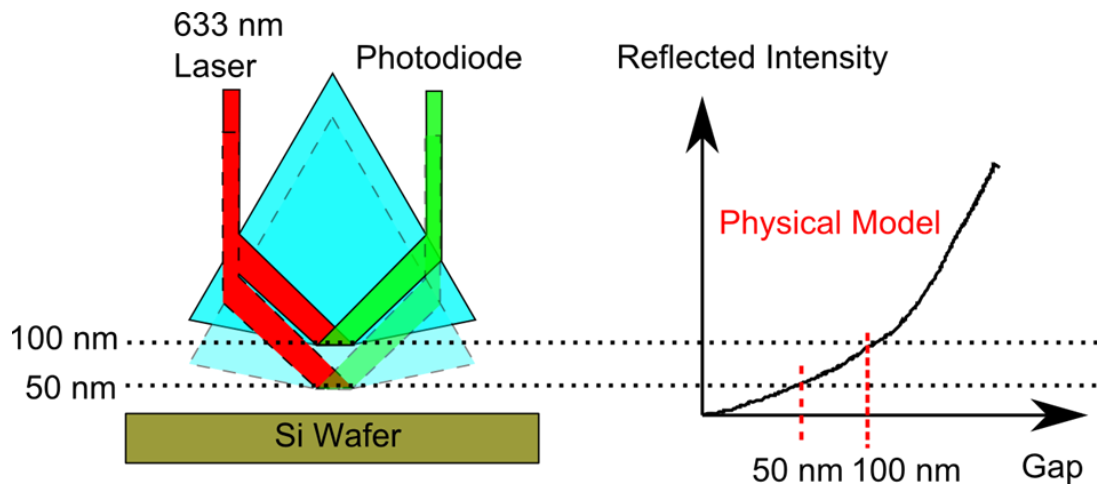


Figure 36. Total internal reflection detection and gap referencing.

It is not possible to correlate the TIR reflection with interference fringes caused by plane waves that are propagating in the air gap with multiple reflections between the bottom surface of the prism and the wafer. This is because as a gap decreases to sub-wavelength, the interference fringes disappear due to insufficient optical path difference (OPD) between the interfering beams. It is therefore impractical to use the interferometric method for gap detection at the sub-wavelength region we are interested in.

Figure 37 shows the experimental observations made on a similar setup which uses near-field solid immersion lens tester that focuses light through different air gaps onto a flat glass sample. Interference fringes are visible when air gaps are relative large at 1000 nm and 500 nm. Below 500 nm, the interference fringes disappear and are replaced by intensity varying dark central regions. This result is similar to what was observed in our experiment.

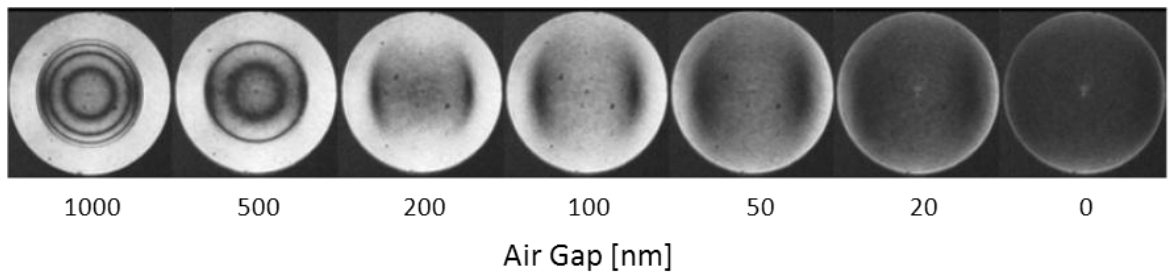


Figure 37. Experimental reflected irradiance observations of a 1.5 NA near-field solid immersion lens tester that focuses through an air gap onto a flat sample of BK7 glass. Observations were made at air gaps of 1000 nm, 500 nm, 200 nm, 100 nm, 50 nm, 20 nm and 0 nm. The illumination was linearly polarized in the vertical direction. [Reproduced from [145]]

#### 4.2.2 Scanning head design

The scanning head is designed to be able to scan at a constant height ( $\sim 100$  nm) above the wafer surface in the presence of disturbance (dust, surface flaw, tilt, vibration, etc.). In our system, two parts including a DC noise canceling carrying air-bearing pad that scans at a constant air gap with regulated air pressure, and an AC noise canceling piezoelectric transducer with real-time closed-loop feedback from gap detection were developed to meet the requirement.

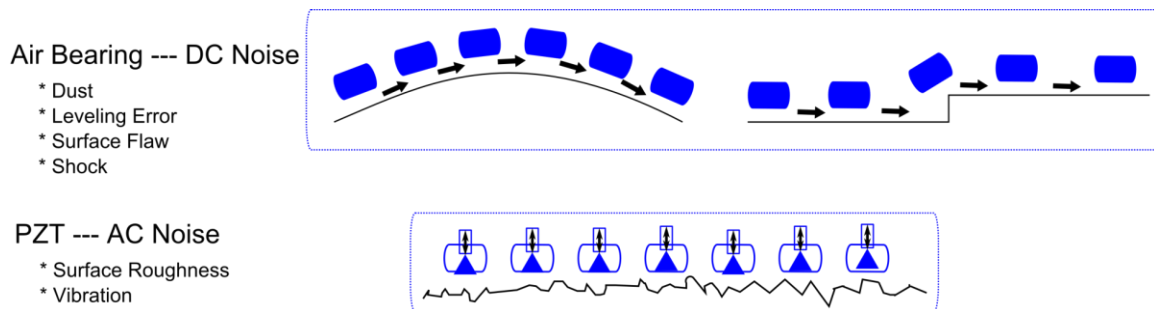


Figure 38. Two-stage gap control head with passive air floating system to control low frequency noise and active piezoelectric transducer feedback system to control high frequency deviation.

The block diagram for both parts is shown in Figure 38. The cylindrical air pad is redesigned from a vacuum preload air bearing to fit in the prism holder and piezoelectric transducer. The 50 mm air bearing was purchased from New Way Air Bearing, which blows compressed air down through a layer of porous carbon at a regulated pressure of 60 Psi to maintain a 0.0051 mm fly height over the wafer surface. The air bearing was then machined to accommodate a rectangular tight slip fit at the bottom in which the prism holder moves up and down by the force inserted from the piezoelectric transducer. This configuration allows movement in the z direction but restrict xy plane motion. An additional advantage of this configuration is to allow alignment of the flat surface of the

prism and the plane of the bottom surface of air bearing. Two rectangular openings were made on the opposite sides of the air bearing to allow light paths at very oblique angles. The original vacuum preloaded air bearing and the modified air pad are shown in Figure 39.

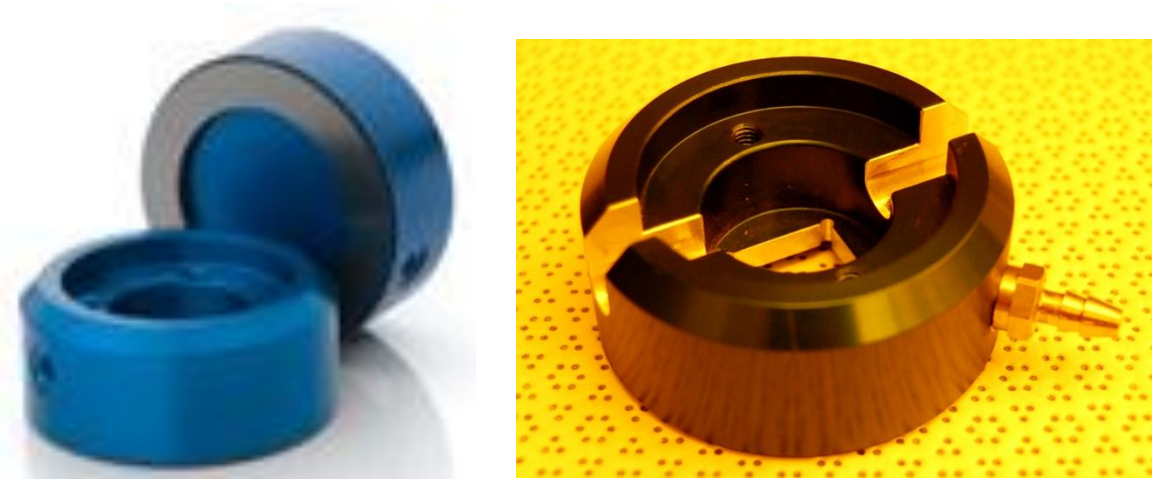


Figure 39. 50 mm air bearing. Left: original vacuum preloaded air bearing purchased from New Way Air Bearing; Right: customized air pad with tight slip fit and side openings.

Figure 40 shows the prism holder designed to accommodate the prism and connect to the piezoelectric transducer. The prism holder was made of aluminum and precisely manufactured to fit in the air pad. Epoxy (3M DP-420) was injected through the eight 2 mm holes to glue the prism to the air bearing while leaving space for oblique light paths. The square pocket on top of the prism holder is designed to glue and locate the piezoelectric transducer. To remove and replace prism, heat is applied with a soldering iron through the 2 mm holes to remove the epoxy.

The low voltage stacked piezoelectric transducer (TS18-H5-104 Piezo System Inc.) is a monolithic ceramic construction of many thin piezo-ceramic layers which are connected in parallel electrically. By applying voltage thus polarizing the electric dipole

moments of in piezo-material, it experiences mechanical deformation so that the piezo-stack elongates or shortens in the length direction [146].

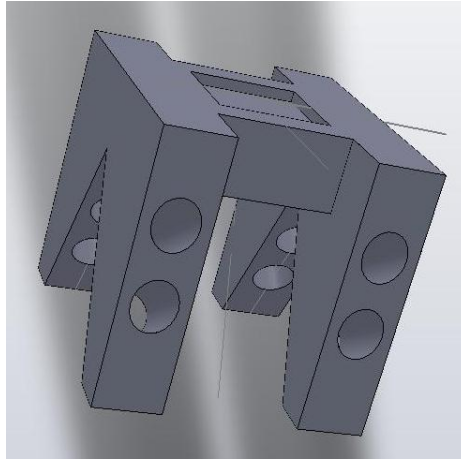


Figure 40. Prism holder designed to fit in the air bearing and actuated by the piezo-transducer.

Figure 41 shows the schematic of the piezoelectric transducer and its voltage-displacement curve. In this specific transducer, the range of motion is  $14.5 \mu\text{m}$  at the voltage of 100 volts in the positive direction. The typical 15 % hysteresis is not an issue in the feedback system we designed. The piezoelectric transducer is eventually glued on both ends to the prism holder and an adapting plate, shown in Figure 42.

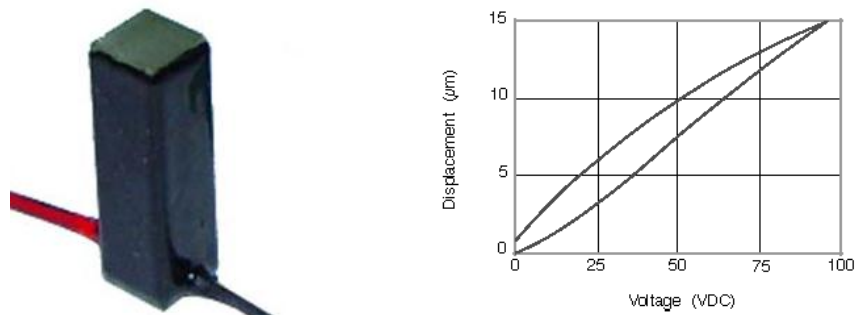


Figure 41. Piezoelectric transducer and its voltage-displacement curve.

To drive the piezoelectric transducer, a DAQ data acquisition box (Measurement Computing USB-1408FS) interfaces with the computer and a linear voltage amplifier (EPA-007-012) is used with maximum current of 30 mA. This low driving current limits the maximum frequency that we can operate the gap servo at, which is determined by  $f = I_{max} / 2\pi V_{max} C$ , where  $V_{max}$  is the maximum driving voltage, C is the piezo capacitance. Given the  $V_{max} = 80$  volts, and  $C = 1600$  nF, the maximum driving frequency allowed by the amplifier is 37 Hz, which is beyond the maximum sampling frequency (25 Hz) of the optical power meter (Newport 2832-C). So the system operation frequency is set at 25 Hz, the limit of the optical power meter.

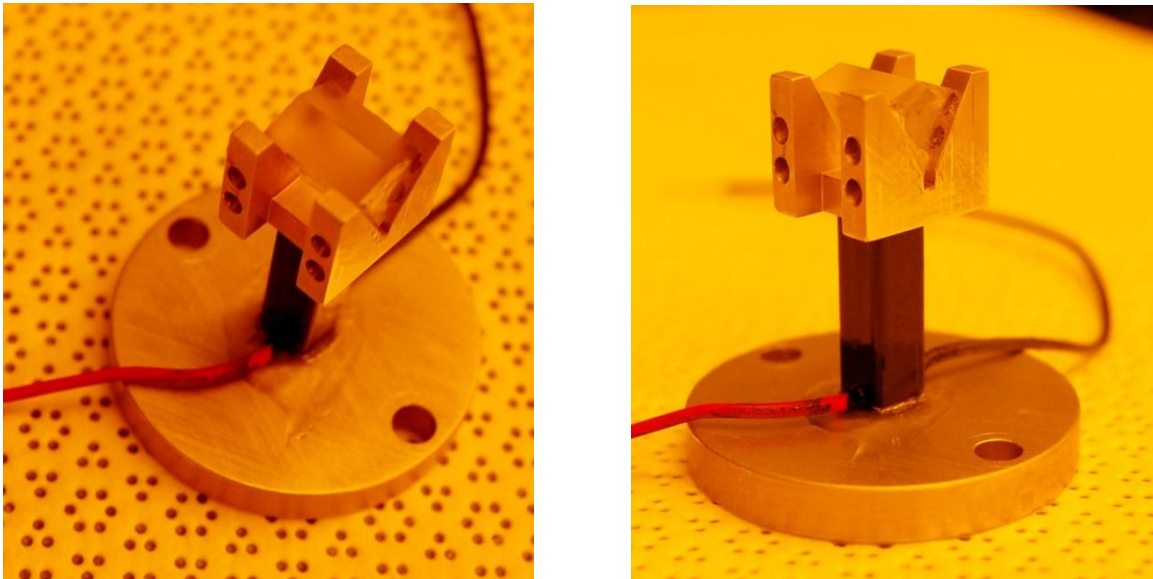


Figure 42. Assembled prism, prism holder, piezoelectric transducer and an adapting plate. The prism was glued to the prism holder through the side holes. The piezoelectric transducer was glued on both ends to the prism holder and an adapting plate.

It is important to fix one end of the piezoelectric transducer so that the actuation function can be realized on the other end. In this design, this is achieved by connecting

the top adapting plate (which glues to one end of the transducer) with the air bearing body with screws and precision machined spacer, making all the components “uni-body”. The spacer design locks in the position of the transducer relative to the air bearing and ensures that the actuation force won’t be absorbed by loose parts in the system. Worth noticing here is that the lock-in position has to be within the range of the motion of the piezoelectric transducer, which is less than 14  $\mu\text{m}$ . The stainless steel spacer pair was first precision machined at the machine shop, then ground onsite iteratively and assembled to reach the target position determined by gapping test. The final assembled imaging head is shown in Figure 43.

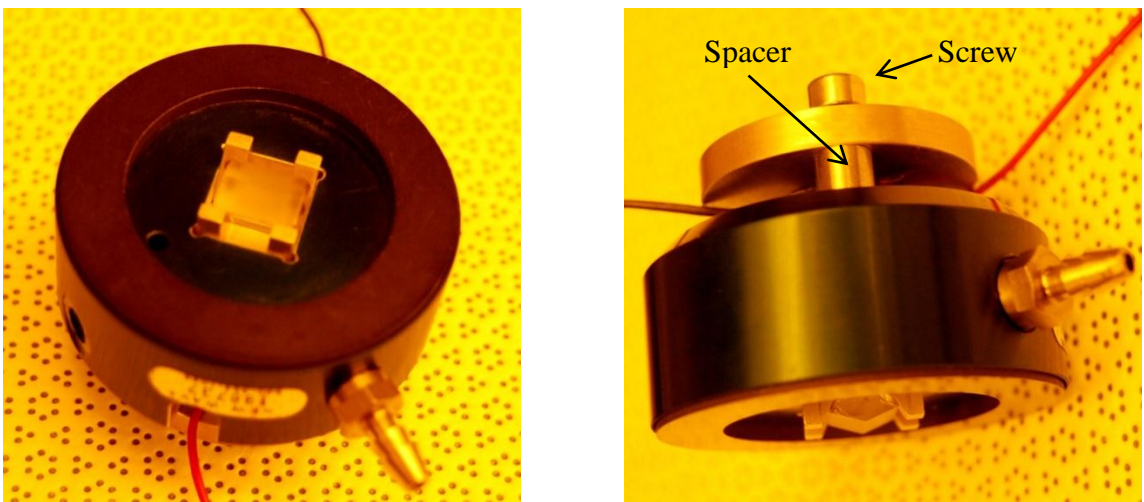


Figure 43. Assembled scanning EWL imaging head. Left: Bottom view of the air bearing with prism inserted; Right: Side view of the imaging head with screw and spacer identified.

To summarize the work in designing and making the scanning imaging head, SolidWorks design of the assembled imaging head is shown in Figure 44. All parts were machined at Micro Instrument Corp., and assembled at RIT Nanolithography Labs.

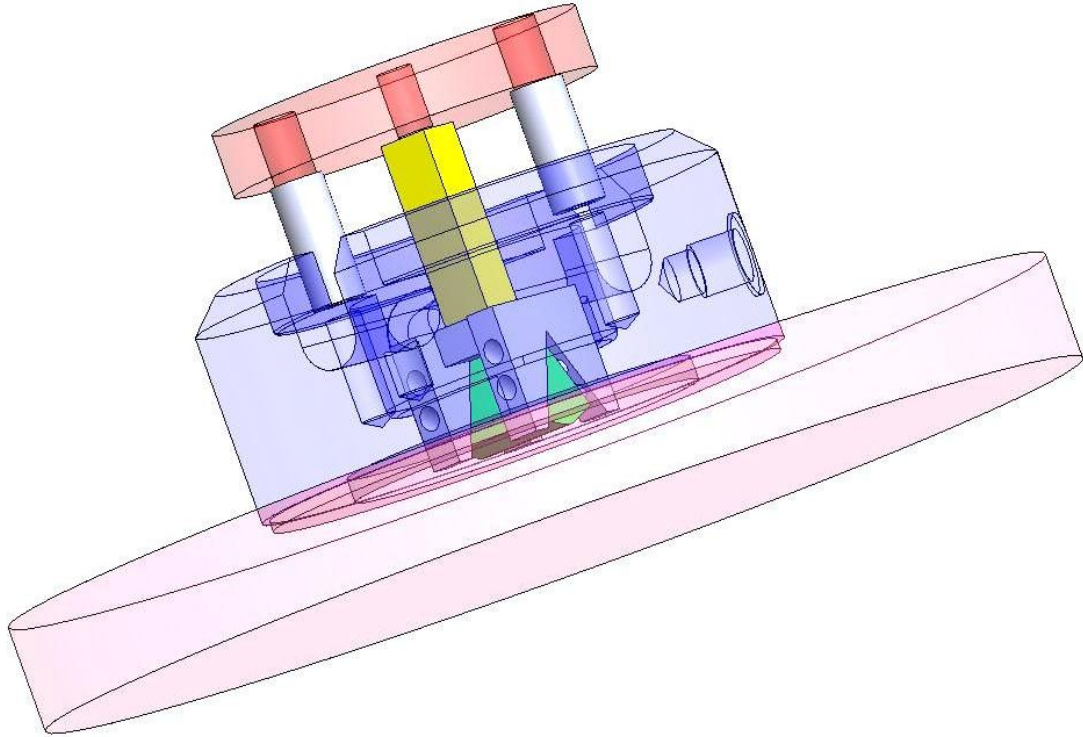


Figure 44. SolidWorks design of the assembled imaging head.

#### 4.2.3 Prism design and manufacturing

The final prisms that were used in the two-beam interference scanning EWL head were manufactured from sapphire and fused silica. The sapphire prism has a higher refractive index ( $n_o = 1.929$ ,  $n_e = 1.917$ ) at the wavelength  $\lambda = 193$  nm and ( $n_o = 1.766$ ,  $n_e = 1.758$ ) at the wavelength  $\lambda = 632.8$  nm. The fused silica prism has a refractive index  $n = 1.56$  at the wavelength  $\lambda = 193$  nm and  $n = 1.46$  at the wavelength  $\lambda = 632.8$  nm. We first purchased  $10 \times 10 \times 10$  mm  $60^\circ$  equilateral dispersing prisms from Crystran Ltd. The shape of the exit surface of the prism is modified to ease the requirement on aligning the prism and wafer. With a flat exit surface, the tolerance on the inclination angle between the prism and wafer becomes extremely small with sub-wavelength gap. To tolerate a small tilt margin, various designs have been proposed by reducing the contact

area, at the expense of exposing a smaller field. These designs include a small protruding flat head [143], spherical head [147] and a conically tapered surface with a small flat head [148], see Figure 45. We chose the conically tapered surface because it is difficult to produce spherical sapphire prisms and the protruding head has a problem with TIR light trapping.

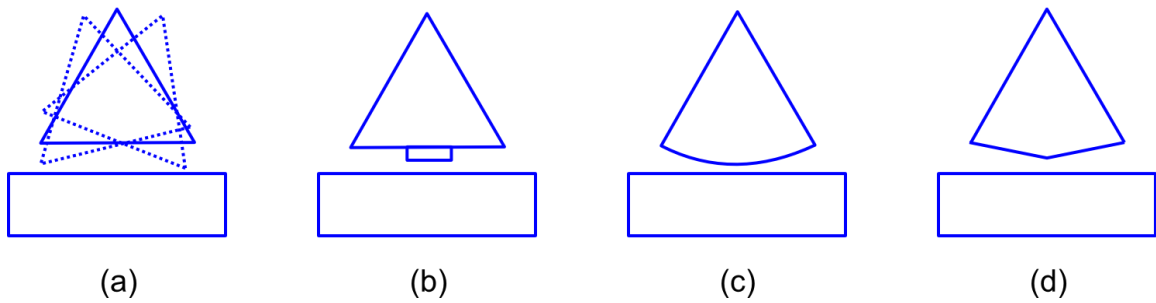


Figure 45. Four different configurations of the exit surface of the final prism. (a). a flat surface; (b). a small protruding flat head; (c). a semi-spherical surface; (d). a truncated cone with a small flat tip.

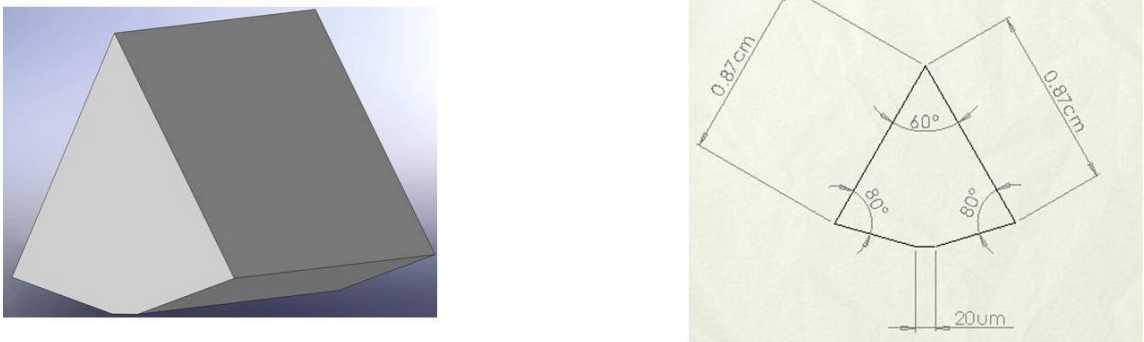


Figure 46. Design of the modified prism with a truncated cone exit surface. The conical angle is set to be 80 degrees and flat tip has a width between 20 and 50  $\mu\text{m}$ .

Figure 46 shows the shape of the exit surface of designed prism. The bottom flat tip is set to be between 20 to 50  $\mu\text{m}$  then the tilt margin for the air gap height of 100 nm

is +/- (0.11-0.29) degrees. The conical angle is set to be 80 degrees because the incident angle of the red monitor laser is between 55 and 65 degrees.

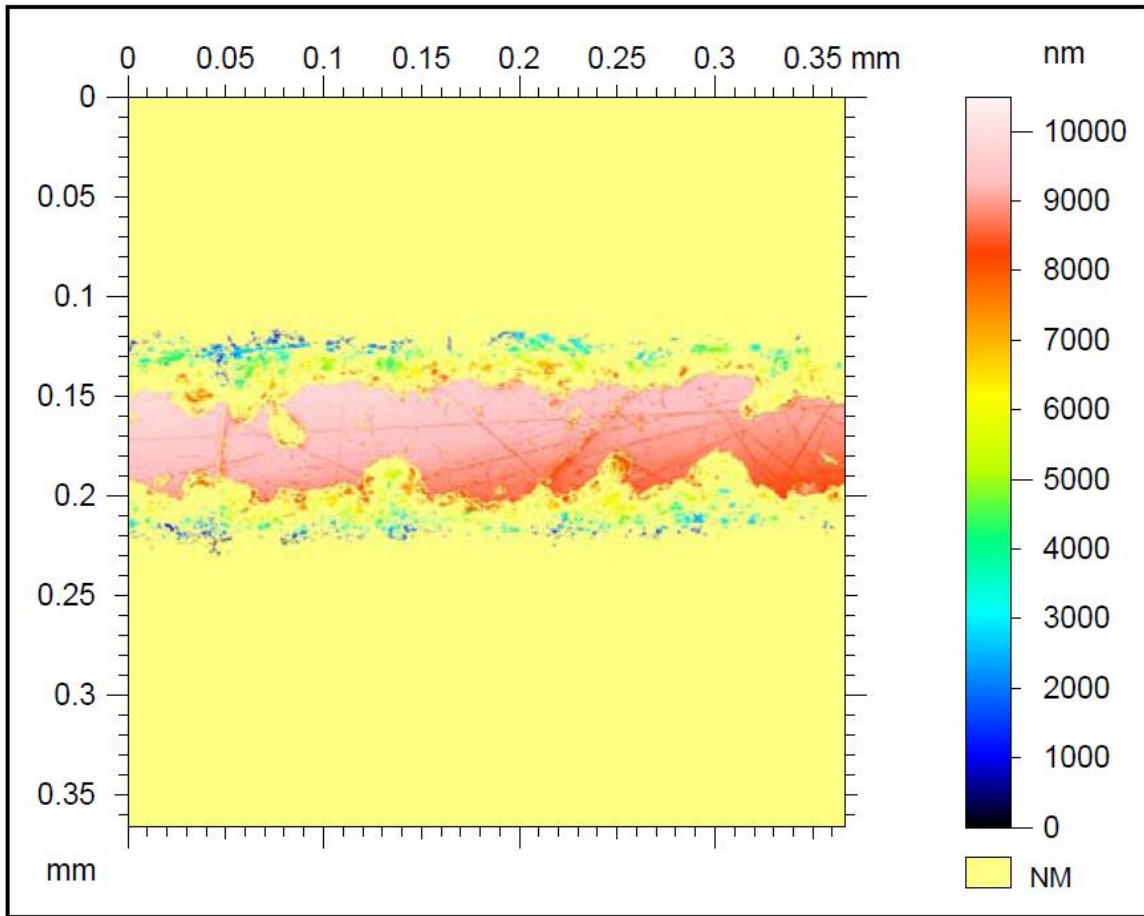


Figure 47. Surface roughness profile of a truncated cone exit surface. The image shows a test-run result on a glass sample without protective coating. The center flat strip shows a width around 50  $\mu\text{m}$ .

In the manufacturing process, the prisms were held using a sine table, angled correctly, and then the surface was ground using a fine grit in very small increments. A test run on glass was first performed to determine the interface between the ground area and polished area. The test run showed several deviations from design. Firstly, the flat tip widens from 40  $\mu\text{m}$  at each end to 50  $\mu\text{m}$  in the middle. Secondly, the flat is offset by 0.3 mm to one side. Finally, the wet grinding process affects the roughness of center strip (6

nm). Since the grit size is significant when compared to the area of the strip, if a grain is pushed across the polished strip in the process it will scratch it. An image is shown in Figure 47. While the first two deviations can be tolerated by allowing the field size to vary, careful measure was taken to avoid scratching the imaging surface. A protective paint was coated on the prisms to try and minimize damage on the polished area. A final microscopic inspection was performed on all three prisms we received from Crystran, shown in Figure 48. All prisms had acceptable surface roughness which validates the protective coating, but the sapphire prism had larger central strip area ( $\sim 275 \mu\text{m}$ ) than the fused silica prism ( $\sim 40 \mu\text{m}$ ). This would result in a tighter tilt margin when controlling the leveling of the prism with respect to the wafer surface.

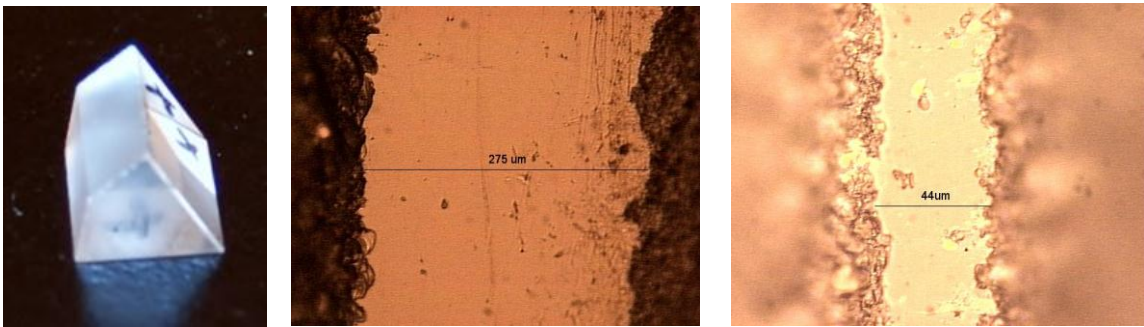


Figure 48. Modified prisms with a truncated cone exit surface. Left: photograph of a fused silica prism; Center: sapphire prism with  $275 \mu\text{m}$  center flat tip; Right: fused silica prism with  $44 \mu\text{m}$  wide center flat tip.

With the truncated cone prism design, the gap detection is made easy with a larger diameter detection laser. Laser reflections from the wedged surfaces will be separated from the flat tip reflection. The light path for the detection laser into a fused silica prism is shown in Figure 49.

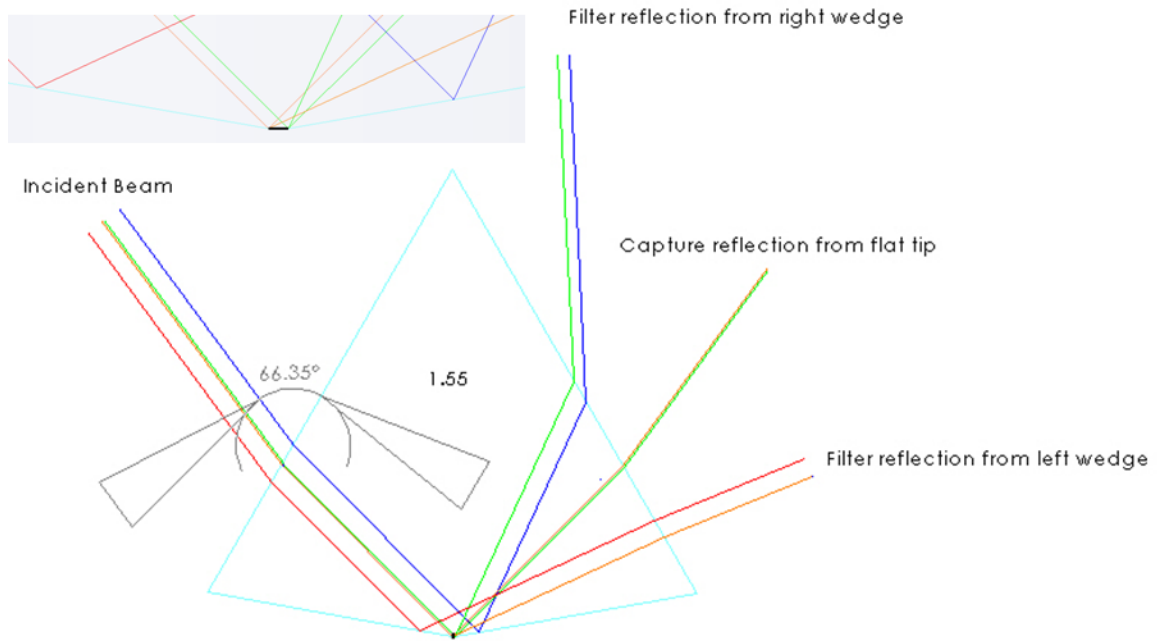


Figure 49. Total internal reflection detection and gap referencing.

#### 4.2.4 Control circuit design

The control algorithm was implemented using National Instruments LabVIEW together with Matlab. The graphic development environment offers a productive way to link the detection, feedback, and actuation components of the system. Figure 50 and Figure 51 show the block diagram and front panel of the control algorithm, respectively. The high-level flow is detailed as follows:

First the average of 1000 TIR signals (A) were referenced to laser source (C) when gap is large [this step is to normalize the laser source fluctuation]. The program then takes the active reflection (B) measurement when gap is in the near-field range (~200 nm) and referenced to laser source (C). The two control actions are developed into two case structures, shown in Figure 52. The sub-vi then computes  $(B/C)/(A/C)=B/A$ , which gives the true reflectance through the small gap. The B/A value is then referenced

to the embedded Matlab code to determine the true gap thickness and then feed forward to controller.

The PID [proportional-integral-derivative] controller, shown in Figure 53, first compares the real-time gap thickness signal and the setpoint target. It then determines the output voltage to piezoelectric transducer. The program, shown in Equation (4.1), involves three separate constant parameters: the proportional term P, the integral term I and the derivative term D [149].

$$u(t) = K_p e(t) + K_i \int_0^t e(\tau) d\tau + K_d \frac{d}{dx} e(t) \quad (4.1)$$

Heuristically, these constants can be interpreted in terms of time: P depends on the present error (the responsiveness of the controller to an error), I on the accumulation of past errors (the degree to which the controller overshoots the setpoint), and D is a prediction of future errors (the degree of system oscillation), based on current rate of change. By tuning the three parameters in the PID controller algorithm with the empirical AutoTune function, the weighted sum of these three actions is used to provide control action. The above actions are included in a while loop to complete the cycle until terminated by user.

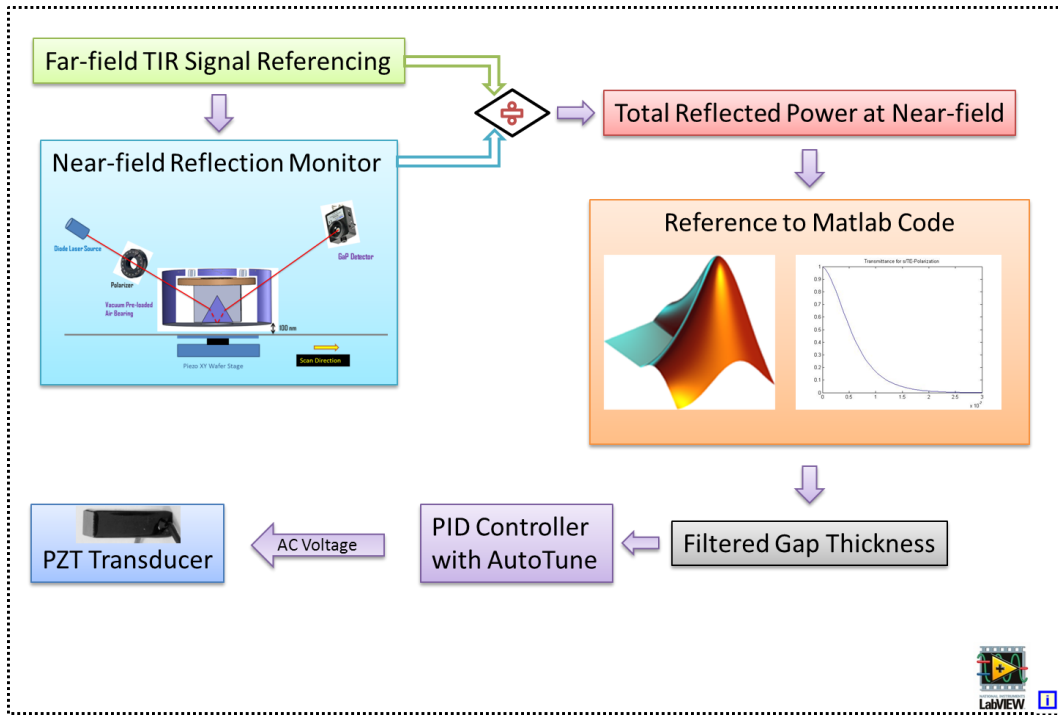


Figure 50. Gap control block diagram.

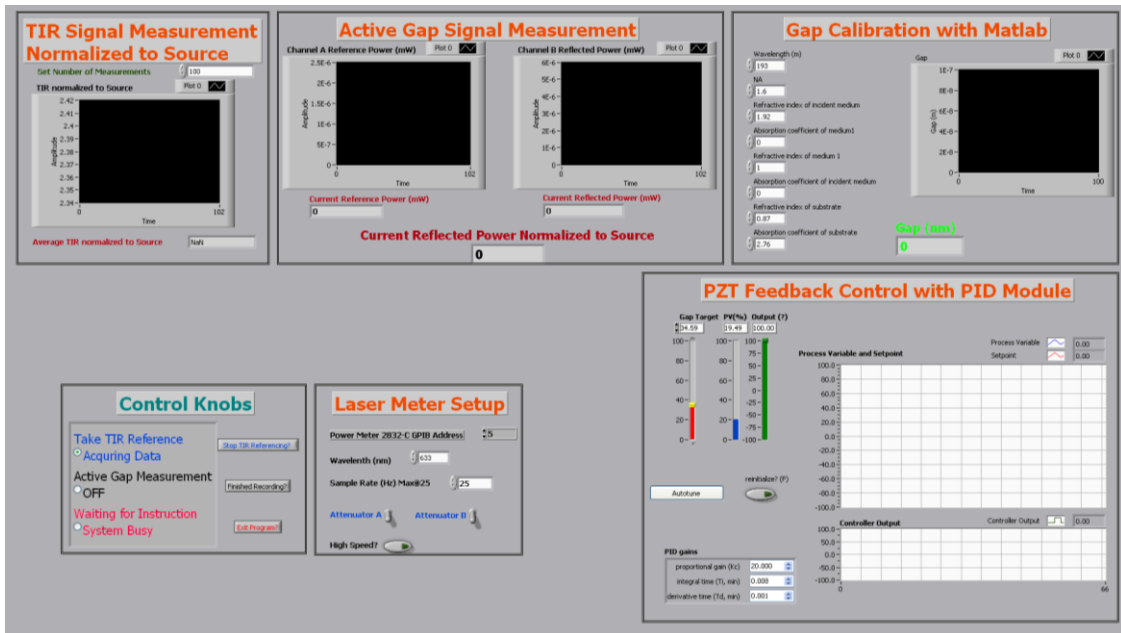


Figure 51. Front panel of the gap control and feedback system.

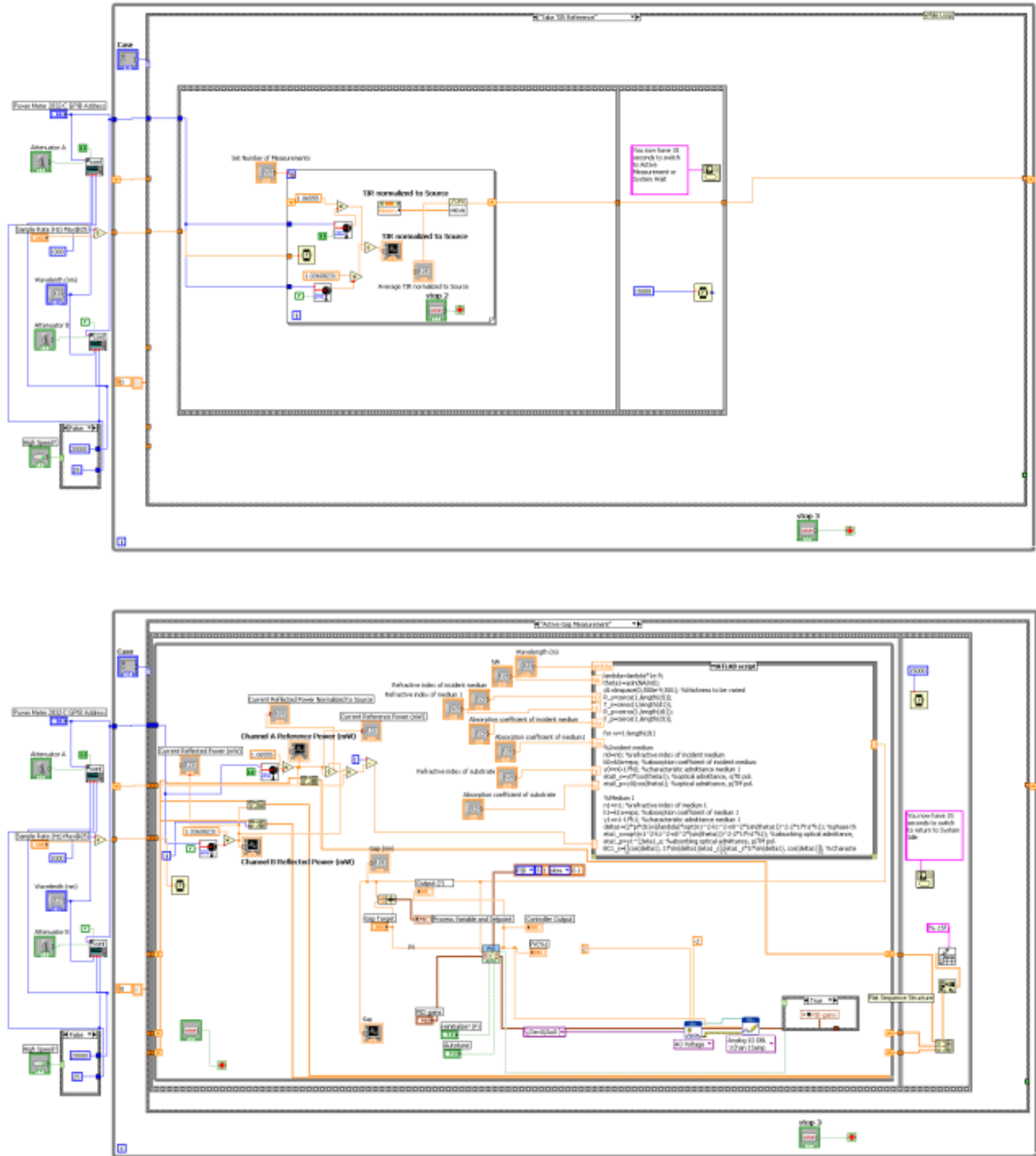


Figure 52. Block diagrams of the two case structures used in the control algorithm. Upper: Case 1 to take TIR reference with calibrated photodiode detectors; Lower: Case 2 to take active gap signal, relate to Matlab code to determine gap, and then feed back to PZT using PID control loop.

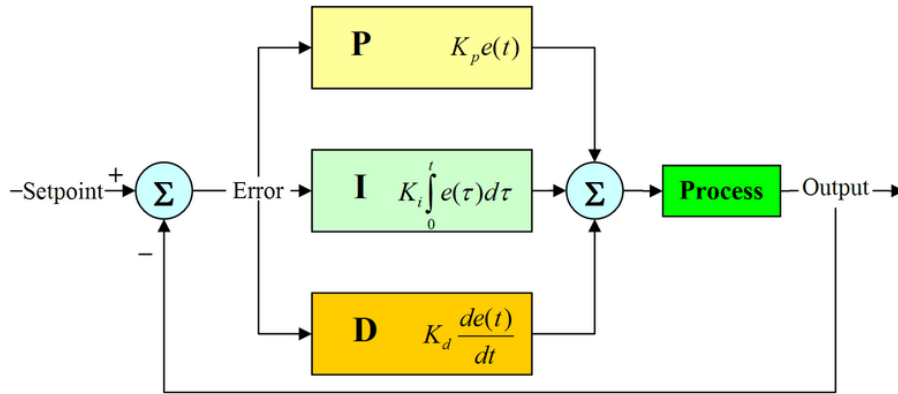


Figure 53. A block diagram of a typical PID controller.

#### 4.2.5 Scanning approaches

Scanning interference lithography has been a relatively new concept. The only known approach, developed by MIT and Plymouth Grating Laboratory, uses the so-called scanning beam interference lithography (SBIL) to manufacture large scale optical gratings with resolution down to 200 nm [101]. In this approach, two small coherent beams are phase compensated by electro-optic components and interfere to generate a small line/space image. The image is raster-scanned over the substrate by use of a high-precision “nano-ruler” stage to stitch the mini-fields to large grating patterns.

Two scanning schemes exist including parallel scanning and Doppler scanning, depicted in Figure 54 [150]. In the parallel scanning scheme, the substrate moves parallel to the interference fringes. Misalignment of the stage motion and the interference fringes causes image smearing. In Doppler scanning, the stage moves perpendicular to the image fringes. In addition to the alignment requirement, the image fringes must also be stationary to the moving staging by phase-locking the interferometer.

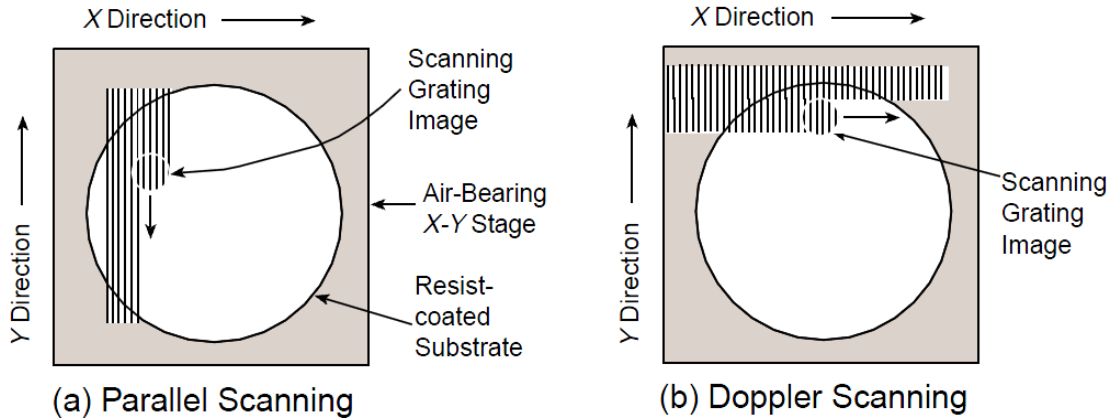


Figure 54. Depiction of two possible scanning schemes used by SBIL. (a) Parallel scanning. (b) Doppler scanning [150].

SBIL system requires sophisticated interferometer-controlled air bearing stage and phase compensating optics. In theory, these components can be integrated with our scanning EWL imaging head with tighter control on stage precision to image sub- 22 nm line/space gratings. In absence of such system, we adopted a dynamic stepping method to demonstrate both imaging capability and scanning height control, shown in Figure 55. The wafer stage was held stationary while the image field was exposed. After the exposure, the wafer scans in the linear direction at constant sub-100 nm gap to another isolated location await next exposure. Gap control system is always active during exposures and scanning. It is noticed here that the lack of full scanning capability is not related to the imaging head but the wafer stage available to us to control nanometer precision movement.

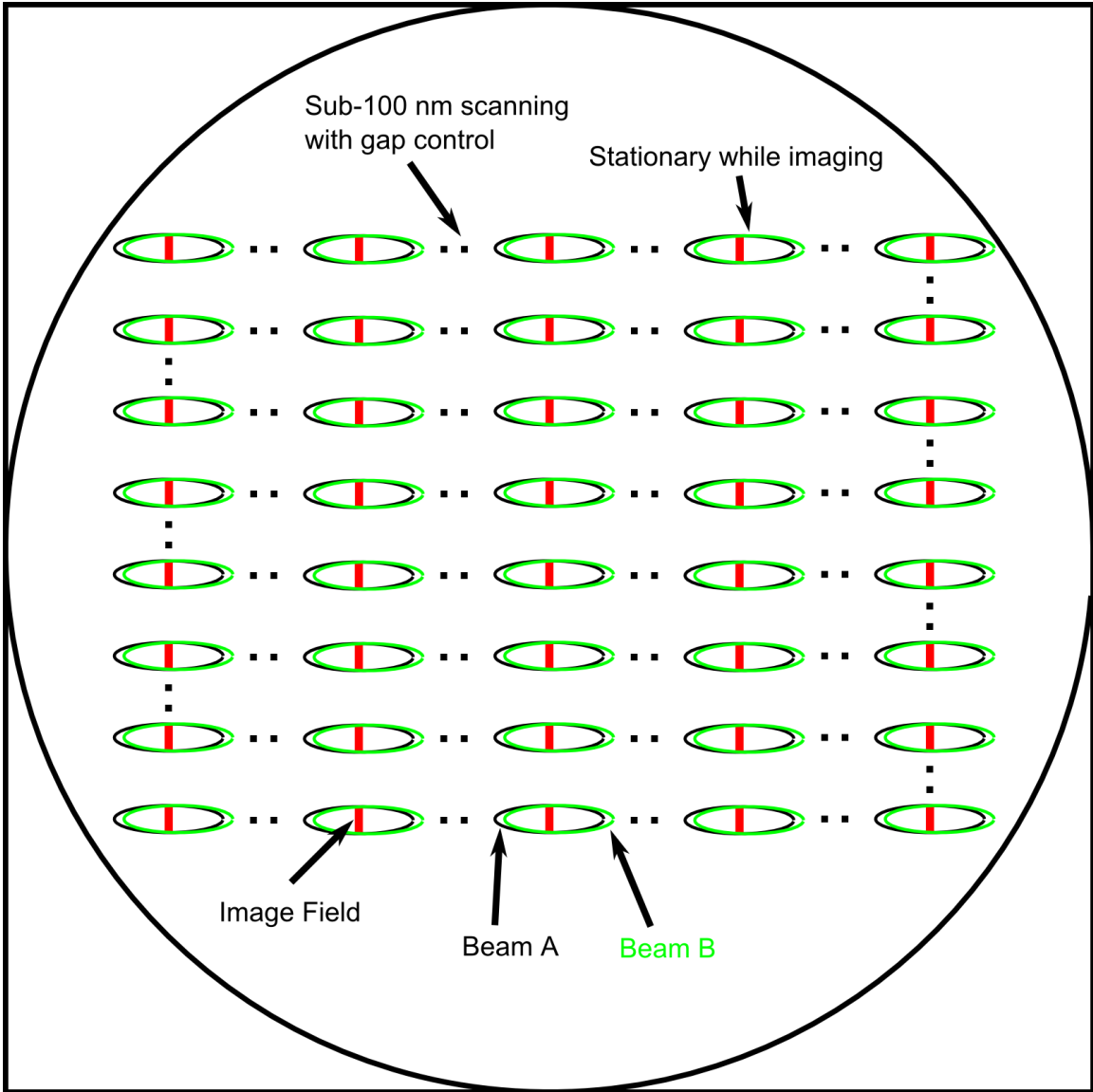


Figure 55. Schematics of the exposure schemes used in this work. The image field was exposed while the wafer is stationary. After each exposure, the wafer scans in the linear direction at sub-100 nm gap to another isolated location await next exposure. Gap control system is always active in both exposure and scanning modes. Beam A and beam B are intentionally misplaced to illustrate two-beam interference imaging. The size of the image field is determined by the prism bottom flat.

#### 4.2.6 Sources of gap variation and system limitation

Sources of Gap Variation		Sources of Internal Noise	
Wafer flatness	< 2 nm	DAQ	4 mV / 0.6 nm
Particles	~ $\mu\text{m}$	PZT transducer	5 mV / 0.8 nm
Stage tilt	Est. 10 $\mu\text{m}$	Laser fluctuation	1.2 nm @ 100 nm gap height
Thermal Expansion	N/A	Beam pointing instability	1.2 nm @ 25 Hz
Stage Vibration	15 nm	Alignment error	Shift absolute gap height
Head vibration	18 nm	PID controller	Improper control causes lots of noise

Table III. Summary of the sources of gap variation and internal noises of the system.

Table III lists the major sources of gap variation in the developed scanning system and the system internal noises that contribute to uncorrectable gap error. Polished silicon wafer has surface roughness around 5 nm but is planarized to less than 2 nm after film-stack coating. Particles in the class 100 cleanroom typically have size no larger than 5  $\mu\text{m}$  in diameter. Wafer stage tilt, while unable to measure directly, is estimated to be on the order of 10  $\mu\text{m}$ . Particles and stage tilt are in fact the largest gap variation and will be corrected by the air bearing. Other sources of gap variations, including material thermal expansion and environment vibration, are estimated on the order of nanometer scale.

Sources of internal noises are the gap errors induced by the control system therefore uncorrectable. These noises become the system error, recognized in the design phase. Electronic noises, including that of the data acquisition box, piezoelectric transducer and the voltage amplifier, have internal electronic noise measured in mVolts. These electronic noises transfer to gap variation through the piezoelectric effect. Monitor laser related error sources include monitor laser fluctuation, beam pointing instability due to reflecting optics vibration, and alignment error. While the first two error

sources could induce 1-2 nm error, misalignment in the optics shifts the absolute gap height measured and could potentially induce a large amount of errors. In this case, the monitor laser optics needs to be carefully aligned to minimize the above-mentioned error.

The PID controller is another potential error source in the system. The gap control module, namely the process gains for the P, I and D, needs to be properly tuned to yield an ideal response of the control system. In the absence of sufficient knowledge about process dynamics and disturbance, it becomes desirable to use empirical autotuning function such as the one supplied by LabView using the Ziegler Nichols method. With an educated guess of initial PID gains, this method iterates the PID values by the setpoint relay which steps the setpoint up or down until the system has reached a tuned state. I and D gains are initially set to zero and P is increased until the loop starts to oscillate. Once oscillation starts, the critical gain  $K_c$  and the period of oscillations  $P_c$  are noted. The P, I and D gains are then adjusted as per the tuning formula tables [151]. Too aggressive or too sluggish controllers contribute to unstable processes such as strong oscillation, overshooting, etc., leading to large gap variation.

---

## 5. EXPERIMENTS AND RESULTS

---

### 5.1 Experimental setup

The “Amphibian” two-beam interferometric imaging platform was used to integrate and test the scanning EWL imaging system. Two optical paths are designed in the system, indicated in “white” (dotted line) and “red” (solid line) in Figure 56.

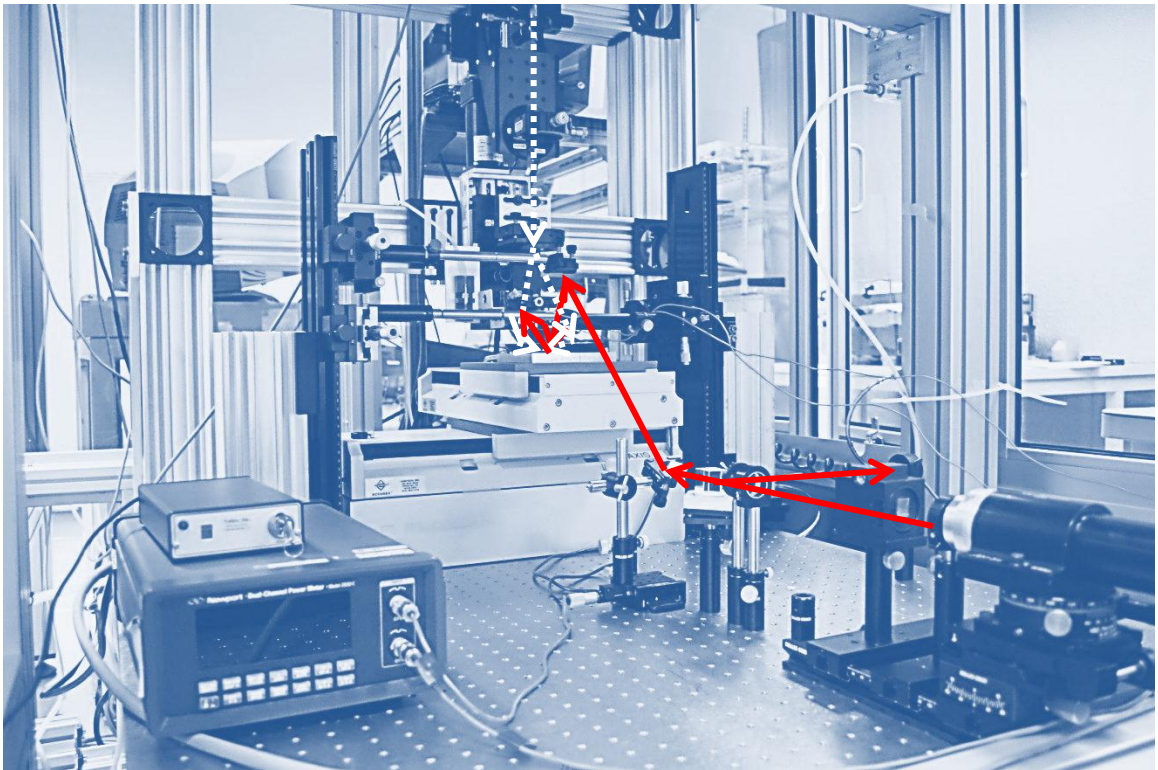


Figure 56. Experimental setup of the EWL head with static gap control. Additional optics were used to shape and direct the reference gap control laser beam.

The “red” (solid line) path indicates the 632.8 nm monitor laser path. A 0.8 W compact HeNe laser is used as the source. After Rochon polarizing optics, the TE polarized beam is expanded 3 times by a homemade beam expander. The expander

follows Galilean configuration which consists of a negative and a positive lens that are separated by the sum of their focal length. Since one of the lenses is negative, the separation distance between the two lenses is much shorter than in the Keplerian design. The expanded beam is then split into 2 beams by a non-polarizing cube beam splitter which is composed of two right-angled prisms. A dielectric coating is applied to the hypotenuse surface to provide equal transmission and reflection as well as to avoid ghost images. Antireflection coatings are used on the entrance and exit faces to minimize back reflections. One beam is sent to a p-i-n type photodiode detector as a laser source monitor to filter out internal laser power fluctuation such as caused by temperature variation. Since no internal power meter and feedback mechanism is available to adjust this fluctuation, the reflected signal needs to be normalized to this source monitor. The other beam is directed toward the imaging head and the reflected signal is picked up by another detector. The two photo-detectors are measured equal distance to the beam splitter to minimize effect of any delays. Figure 57 shows reflected laser beam follows the fluctuation of the incident laser beam. The division of the two signals gives the relative reflected power, filtering out any fluctuation in the laser source.

The alignment of the monitor laser to the prism has a significant impact on gapping. Since the gap is calculated by referencing the reflected signal to a theoretical EW model, mismatch in the incident angle or lateral shift at the prism flat causes erroneous gap reading and potential collision to the wafer. In the current setup where a prism is used as the final optical element, an off-axis incident beam is required to monitor the gap. When the prism moves up and down to adjust for gap height, the oblique laser beam becomes misaligned with the 50  $\mu\text{m}$  prism flat.

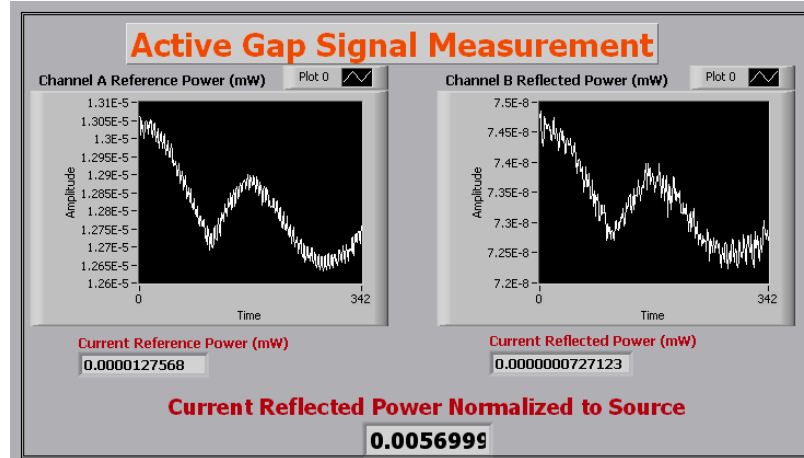


Figure 57. Reflected intensity as a function of incident laser light fluctuation. Left: Incident laser light fluctuation; Right: reflected laser light fluctuation. The two beams were separated by a non-polarizing beam splitter and detected with two calibrated broadband photodiodes.

As shown in Figure 58, there are two configurations to set up the final turning mirror to align monitor laser beam with prism. In configuration (a), the final turning mirror is mounted on the same micrometer stage together with the imaging head. In the initial alignment process, any micrometer movement will be amplified by additional distance travelled by the beam reflecting off the mirror and results in the worst misalignment between monitor beam and prism flat. The situation gets worse if the mirror presents different reflection angles at different locations. Configuration (b) is used to set up the monitor beam instead. In this configuration, the mirror position is independent of the prism position. The laser beam is always angularly aligned with prism flat but different portions of the laser beam are reflected. This then requires the laser beam has a uniform intensity profile. This is realized by increasing the beam size of the monitor laser with intensity homogenization provided by a beam expander.

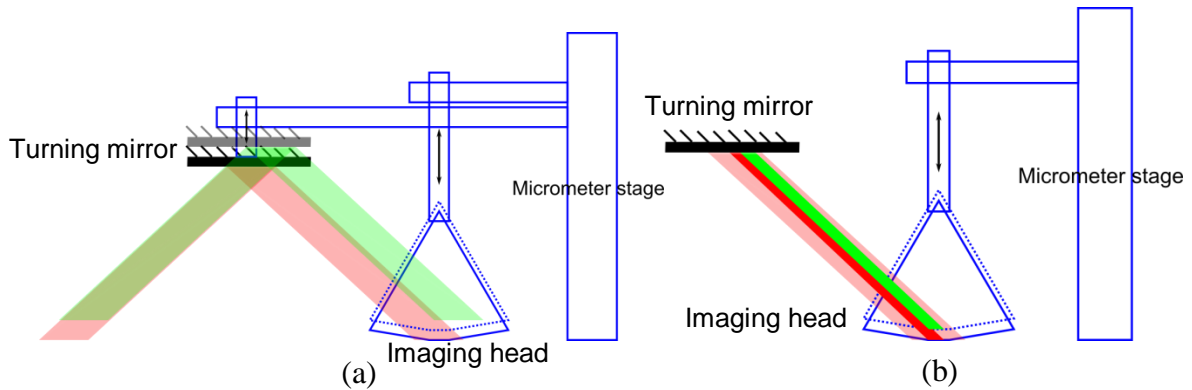


Figure 58. Two configurations showing misalignment between monitor laser and prism bottom flat when the imaging head moves vertically. (a): Final turning mirror mounted on micrometer stage; (b): Final turning mirror stationary.

Direct alignment of the monitor laser beam to the prism flat is difficult with the flat dimension to be  $50\ \mu\text{m}$ . The reflected signal intensity is then used as the alignment indicator. With the prism flat driven by the micrometer stage against wafer plane (zero gap height assumed), the monitor laser beam is aligned to the flat by observing the maximum intensity on the reflection beam. Once aligned, the prism is lifted to perform the initial “pull-in” procedure for the monitor laser to establish the reference reflected intensity as the far field signal. It does so as the EWL head is driven toward the wafer surface by a motorized micrometer stage, signal first increases which indicates the misalignment. The laser is aligned with the prism as soon as the reflectance reaches its peak. Further movement of the head toward the wafer surface induces evanescent tunneling so the peak signal becomes the reference signal. The observed intensity variation as a function of prism position is shown in Figure 59. The experimentally observed intensity drop agrees well with simulated reflectance attenuation using the experiment conditions.

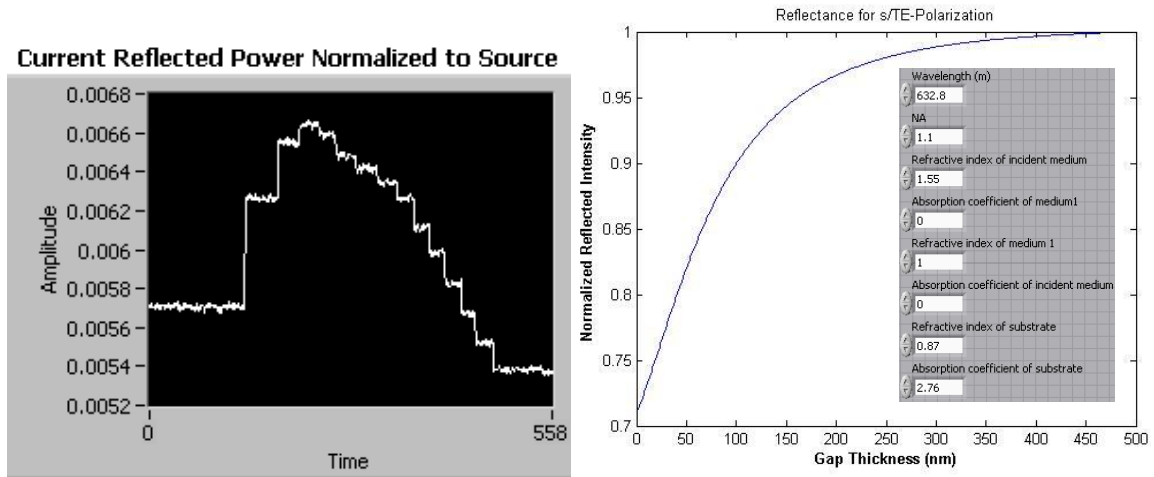


Figure 59. Left: Normalized reflectance power when the EWL head was driven toward the wafer surface by a motorized micrometer stage. The signal first increases which indicates the misalignment between the reference laser and the prism flat tip. The laser is aligned with the prism as soon as the reflectance reaches its peak. Further movement of the head toward the wafer surface induces evanescent coupling; Right: Simulated reflectance as a function of gap thickness in the gapping setup used in this experiment. The inset shows the experimental and simulation condition.

The “white” (dotted line) path in Figure 56 indicates the 193 nm imaging path. A line-narrowed ArF excimer laser source produces 193 nm light with 6 pm full bandwidth, which translates to 6.2 mm temporal coherence length. The laser light is expanded by 4 times to meet the coherence and field uniformity requirement. The beam then goes through a spatial filter to eliminate artifacts until it diffracts through a phase grating. The +1 and -1 diffraction orders are redirected by two final turning mirrors to recombine at the bottom of the prism flat. The varying mirror angles and positions allow the system to achieve different interference pattern periods in the resist.

As shown in Figure 60, the imaging head is mounted on a motorized micrometer z-stage through adapting rotational micrometer, while the wafer is placed on an XY

translational vacuum stage (Aerotech Accudex Model: ATS20020-U-40P; Controller Unit: Aerotech DR500). Both stages have 0.5  $\mu\text{m}$  travel resolution.

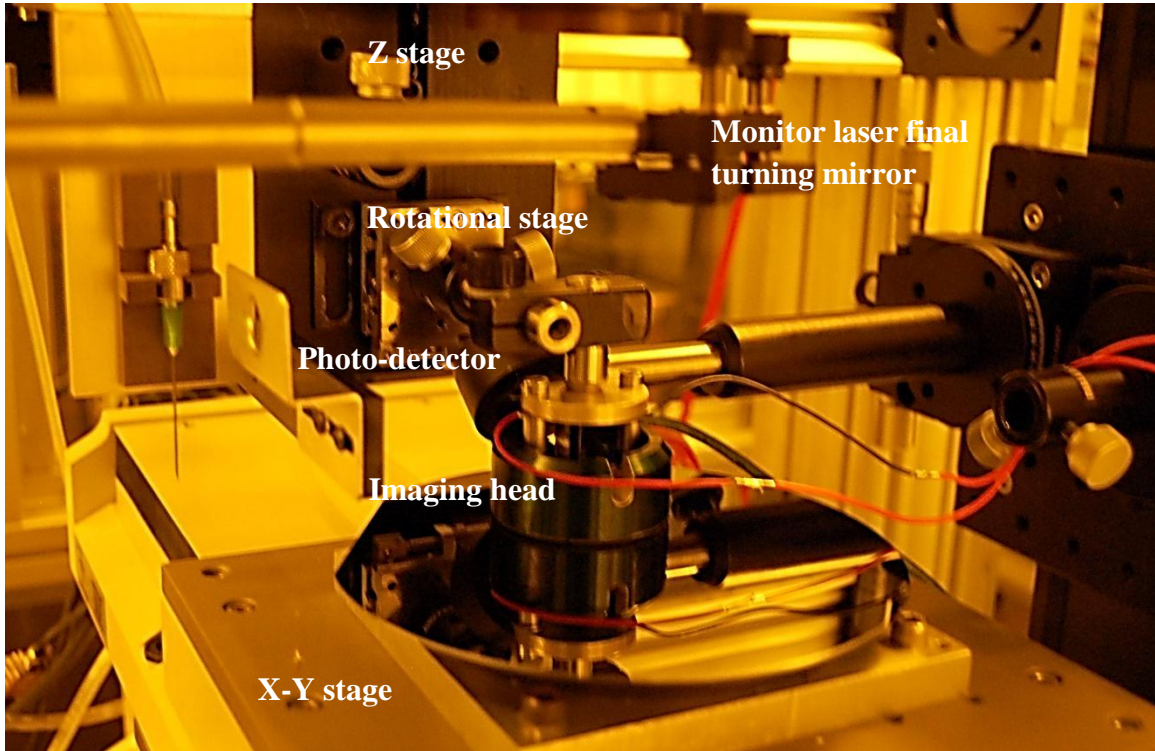


Figure 60. Static EWL head with gap control module to maintain constant gap above wafer surface. The EWL head was mounted on a motorized micrometer stage while the wafer is placed on an XY translation stage.

The mounting and alignment of the imaging head and imaging optics procedure is illustrated in Figure 61. Here, the image field has a center stripe which is 50  $\mu\text{m}$  and 1 cm long which corresponds to the prism flat. The two side lobes indicate leaked refraction beams from the two sides adjacent to the flat. The coarse alignment is done by positioning the imaging head against the wafer stage with zero gap and visually inspecting the reflected image beam from the flat. Fine alignment is achieved by iteratively exposing multiple resist samples and realigning the system based on the

appearance of the image fields. The image side lobes represent the leaked beam from the oblique prism surface directly adjacent to the flat. If the two image side lobes have left-right or up-down asymmetry, this indicates that the two final turning mirrors were misaligned and need to be adjusted accordingly. If the two image side lobes have intensity asymmetry (color difference), or the center image stripe has intensity asymmetry across the field, then the imaging head is tilted in left-right, or front-back direction. After iteratively adjusting and inspecting the image fields, the system is aligned. It is desirable in future system extensions that additional piezo-transducers be included for better alignment control. A redesign of the imaging head with vacuum preloading is another way to achieve self-alignment.

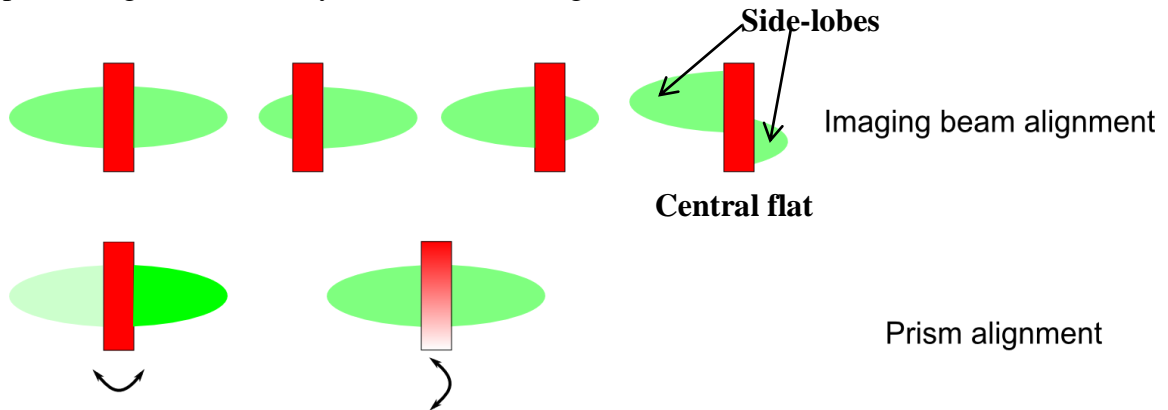


Figure 61. Illustrations of imaging samples indicating prism tilt and imaging beam misalignment.

## 5.2 Image contrast degradation

### 5.2.1 System vibration

Vibration measurements were performed on all aspects of the imaging system to ensure satisfactory gapping and imaging performance. Measurement data were taken from an ultra-quiet (10V/g), ultra-low frequency (0.05Hz) seismic accelerometer and power amplifier system (Wilcoxon Research 731A/P31). The voltage signals were then

inputted to a customized LabView program to compute and analyze the velocity power spectrum and vibrational displacement.

Based on the generic vibration criteria (VC) published by Colin Gordon & Associates, sub-100 nm lithography imaging should meet VC-D (velocity amplitude between 12.5 and 6.25  $\mu\text{m/s}$  from 1 to 80 Hz), which is suitable in most instances for demanding equipment, including many electron microscopes and e-beam systems; and preferably VC-E (velocity amplitude between 6.25 and 3.12  $\mu\text{m/s}$  from 1 to 80 Hz) which can be a challenging criterion to achieve [152]. VC-E standard is assumed to be adequate for the most demanding of sensitive systems including long path, laser-based, small target systems, e-beam lithography systems working at nanometer scales, and other systems requiring extraordinary dynamic stability.

Figure 62 and Figure 63 show the measured vertical and horizontal vibration velocity spectrum from 1 to 100 Hz, respectively. DC bias and high frequency noise are removed from the spectrum. It is shown that all system components except the monitor laser final turning mirror meet at least the VC-D standard. The poor vibration performance on the turning mirror is the result of its long arm due to space limitation. However, this much vibration doesn't directly translate to imaging performance but relates to the gap signal detection. Furthermore, since the sampling frequency of the gap detector is set at 25 Hz, the vibrational resonance peaks between 40 and 80 Hz shown on the turning mirror spectrum do not contribute to gap noise. A detailed summary of the system vibration measurement data and its respective vibration criterion is listed in Table IV.

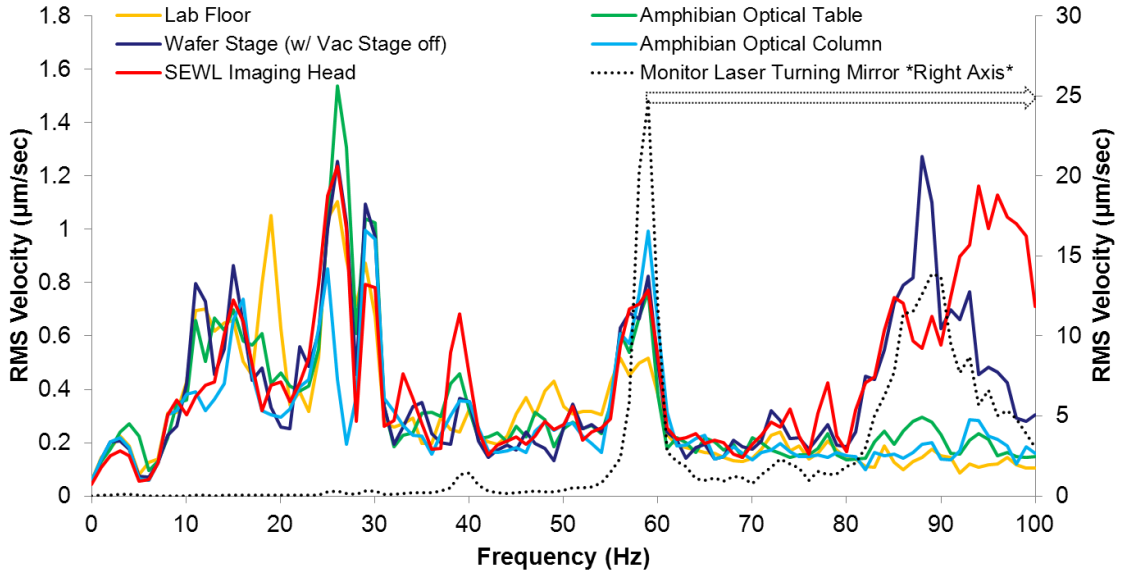


Figure 62. Measured vertical vibration velocity spectrum on SEWL imaging system.

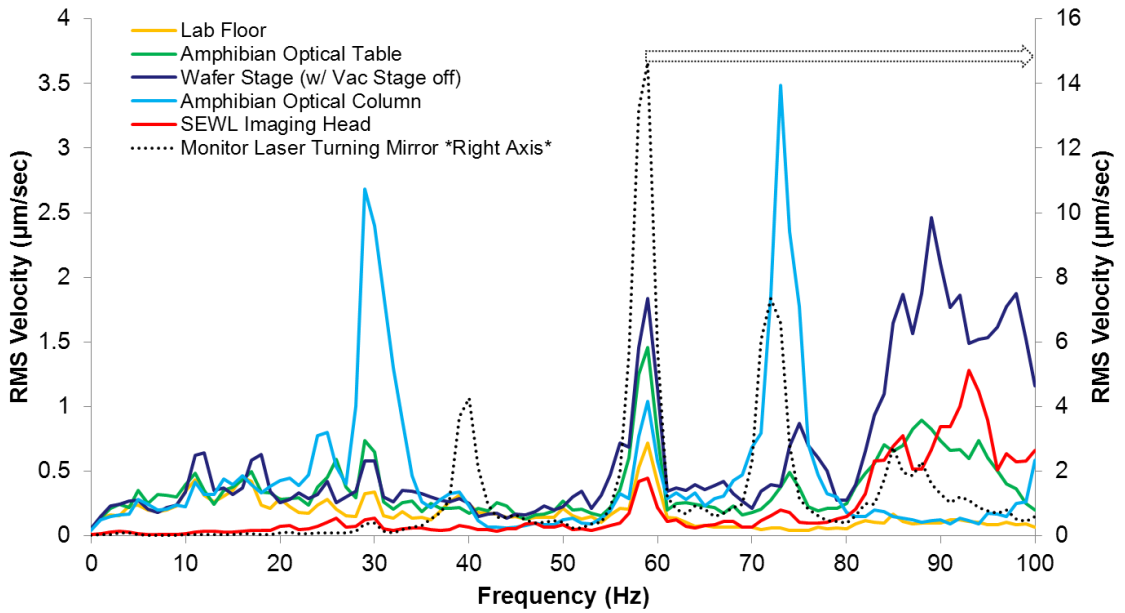


Figure 63. Measured horizontal vibration velocity spectrum on SEWL imaging system.

		Floor	Amphibian table	Optical column	Wafer stage	Imaging head	Turning mirror
Vertical Vibration	Velocity <sub>rms</sub> (μm/s)	2.351	2.483	2.583	5.940	7.286	23.95
	Displacement <sub>rms</sub> (nm)	15.46	15.15	12.44	14.69	14.61	55.95
	Vibration Criterion	E	E	E	E	D	B
Horizontal Vibration	Velocity <sub>rms</sub> (μm/s)	1.934	3.160	5.842	11.64	5.175	12.99
	Displacement <sub>rms</sub> (nm)	11.19	13.28	16.73	20.00	5.234	32.17
	Vibration Criterion	E	E	E	D	E	C

Table IV. Summary of the measured vibration data on SEWL imaging system.

### 5.2.2 Imaging misalignment

Optical system alignment is a critical step to achieve high contrast interference imaging. 193-nm excimer lasers are notorious for poor coherence, both temporally and spatially. Lacking a well-defined ground state for energy level transition, a typical free-run excimer laser's spectral line width is about 0.5nm. Modern line-narrow optics reduces this number to less than 1pm. In addition, excimer lasers have a very low degree of special coherence (around 1mm spatial coherence length) in that a large number of transverse modes are operated inside the laser cavity. While such low coherence is desirable in projection lithography to eliminate unwanted interference within the aerial image, it puts extra rigorous requirement on the amount of two-beam OPD that can be tolerated in interferometric imaging.

Detailed theoretical study on coherency, OPD and contrast has been done elsewhere; for example see [153]. For a spatially coherent imaging system, imaging contrast (visibility) is characterized as:

$$Contrast = \exp\left[-\left(\frac{\pi * OPD}{2l_c}\right)^2\right] \quad (5.1)$$

where  $l_c$  is the temporal coherence length. In a partially coherent system such as the one we use, the image contrast is also dependent on image field location which degrades from field center. To simplify the calculation, the spatial component of the image contrast is lumped in to an effective temporal coherence length, which yields the normalized contrast curve as the function of the OPD, as shown in Figure 64. Two sets of experiments were performed to vary the angular alignment (two beams with different in-plane incident angles) and the tilt alignment (two beams with different out-of-plane incident angles). To yield a satisfactory interference image, the required OPD is estimated to be less than 1 mm.

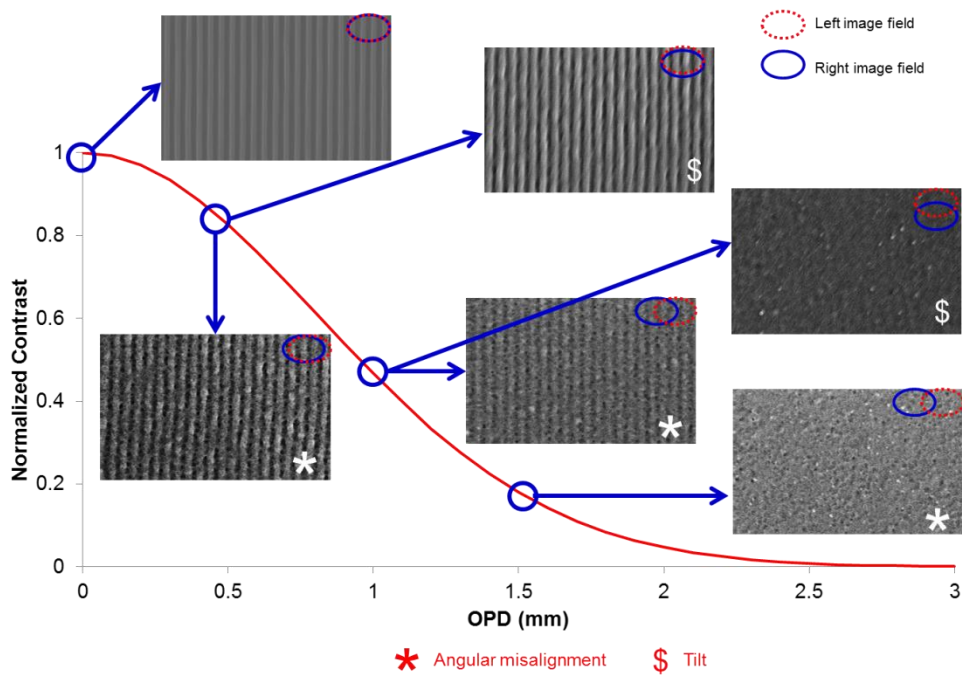


Figure 64. Simulated and experimental verification of contrast degradation as a function of system misalignment OPD between two interferometric arms. Experiments carried out on static EWL system with NA=1.3.

### 5.2.3 *Process latitude*

When employing ultra-high NA imaging, there is an extremely narrow process window in terms of dose and focus. Image quality degrades significantly from the best process condition. Although image contrast is independent on exposure dose, over- or under-exposures do not proportionally yield satisfactory line space gratings with different duty ratios. Figure 65 shows SEM snapshots taken with different exposure doses. Bridging, scumming, resist thinning, and LER are visible through the exposure dose matrix. These effects are difficult to model with existing resist models but contribute to image quality degradation nonetheless. In this experiment at 1.3NA, the exposure dose window is less than  $0.5 \text{ mJ/cm}^2$ . This number is expected to drop to  $0.2 \text{ mJ/cm}^2$  at 1.8NA. This is an extremely small dose window in the laser and optical system used in this experiment.

Two-beam interference lithography has the advantage of theoretically infinite depth of focus since the two first orders are symmetrically incident on the imaging plane. Practically, however, it is limited by the spatial coherency, beam uniformity and hyperbolic aberration. In this system, contrast degradation mostly arises from the short spatial coherence length which is estimated to be less than 2 mm. Experimental results displayed in Figure 66 show less than 1 mm depth of focus, which is significantly larger than that of the state-of-the-art 1.35 NA projection lithography system at around 100 nm.

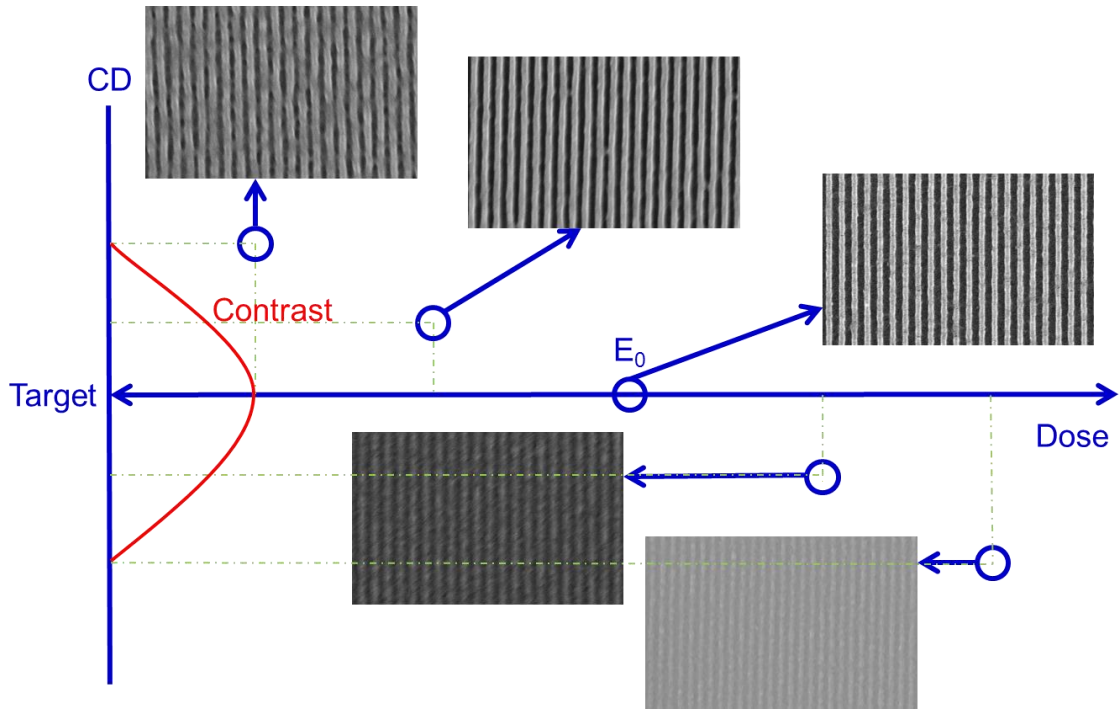


Figure 65. SEM snapshots showing pattern imaging quality degradation as a function of dose. Experiments carried out on static EWL system with NA=1.3.

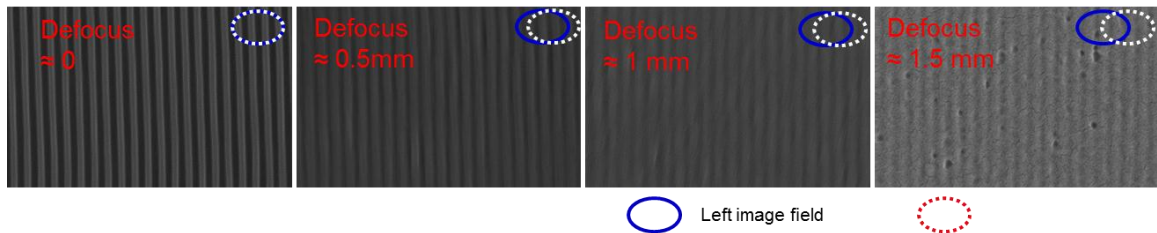


Figure 66. Simulated and experimental verifications of image quality degradation as a function of imaging plane defocus. Experiments carried out on static EWL system with NA=1.3.

#### 5.2.4 Gap height

Theoretical derivation in Chapter 3 shows the exposure dose dependence on gap height. In another words, gap height variation changes the amount of tunneling photons but should have no obvious effects on image quality except the nanometer scale defocus. As shown in the previous section, the amount of defocus that can be tolerated by our

system is significantly larger than projection systems, and it is expected that the contrast degradation would be minimal through the less than 100 nm depth of focus. This is experimentally confirmed and results are shown in Figure 67. No significant image quality difference is observed at different gap heights at the best dose condition. It should be also noted that since sub-100 nm gap height significantly changes dose-to-size, variations in gap height during exposure could potentially affect the image log slope and contribute to CD variation and LER.

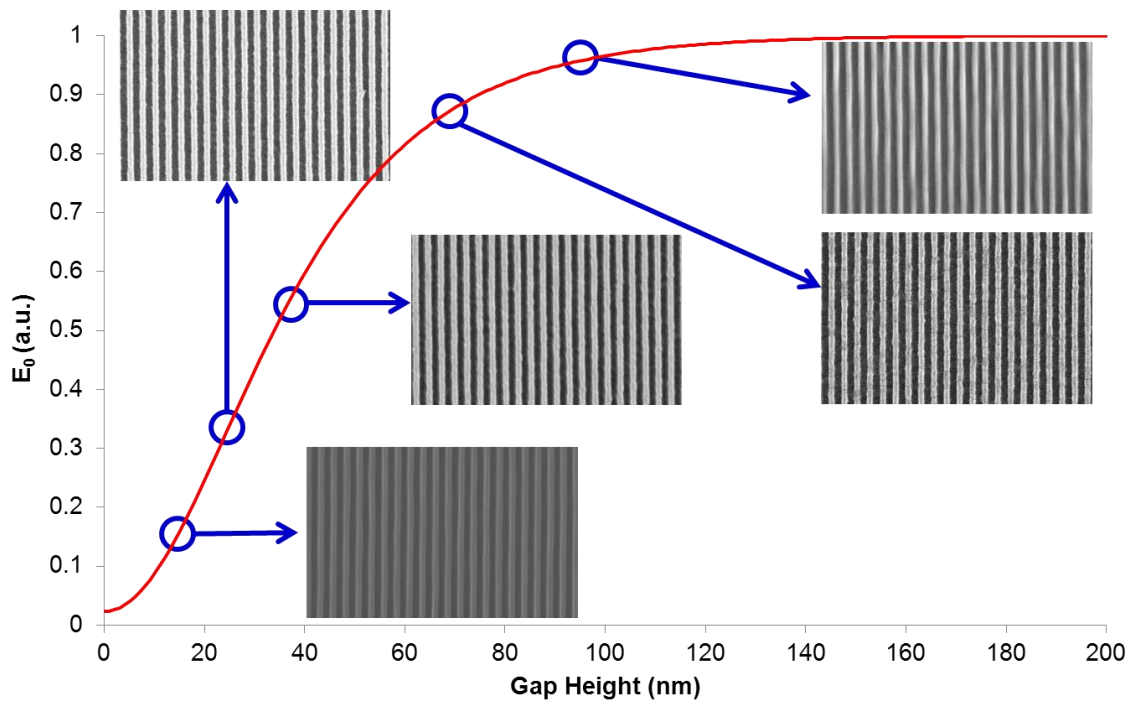


Figure 67. SEM snapshots of 1:1 line-space grating taken at different gap heights. Experiments carried out on static EWL system with NA=1.3.

### 5.3 Gapping and imaging with fused silica prism and sapphire prism

#### 5.3.1 Static gap gauging

After the imaging system was mounted and aligned, the static gap signal was read out through the control software. Figure 68 shows the real time gap signal with optimized

controller at various gap targets. The controller, as mentioned in previous chapter, needs to be fine-tuned by the auto-tuning program to yield a stable process. Figure 69 shows the characteristics of different gap control scenarios at 100 nm gap target. The green data line (B) shows the gap signal without any feedback control. The noise level is measured to be around 4.02 nm. This noise is due to the environmental vibration and internal laser fluctuation. With the controller switched on but unoptimized, the gap signal shows different characteristics and could potentially deteriorate. The blue data line (D) shows the gap signal with a faster than normal PID control. This control scheme tends to have a large P value (over-compensate the present error) but then overshoots the target and oscillates. The yellow line (A) represents a slower controller where the feedback reaction is slow and fails to capture the process variation. The red line (C) shows an optimized controller with gap target set at 100 nm. The noise level is measured to be 1.38 nm in this case. It is noted that the optimum controller configuration is different at each gap target. Therefore, the controller needs to be tuned when it is switched to a new gap target.

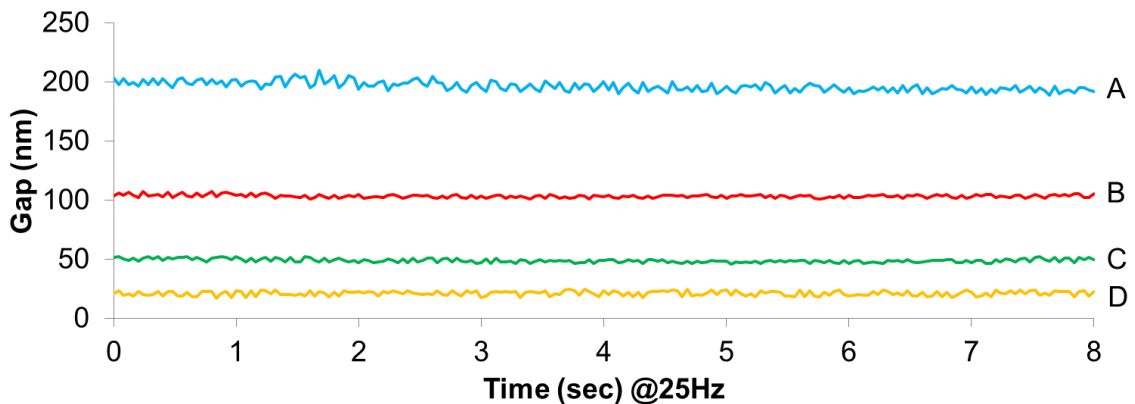


Figure 68. Static gapping results with optimized controller at various gap heights.

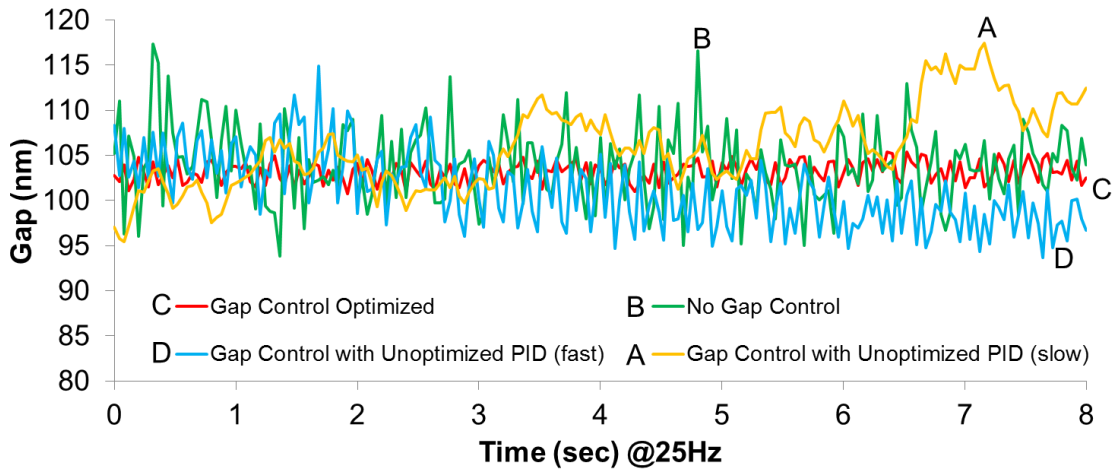


Figure 69. Static gapping results showing gap heights variation in various control scenarios.

To validate the static gap control module, the gap target is modified during gap servo operation. Figure 70 shows two scenarios when gap target is switched from 200 nm to 100 nm, and from 100 nm to 200 nm. The results show responsive gap switching, but notice that the new gap target exhibits larger noise level. This is because the gap control has only been optimized for the initial gap target.

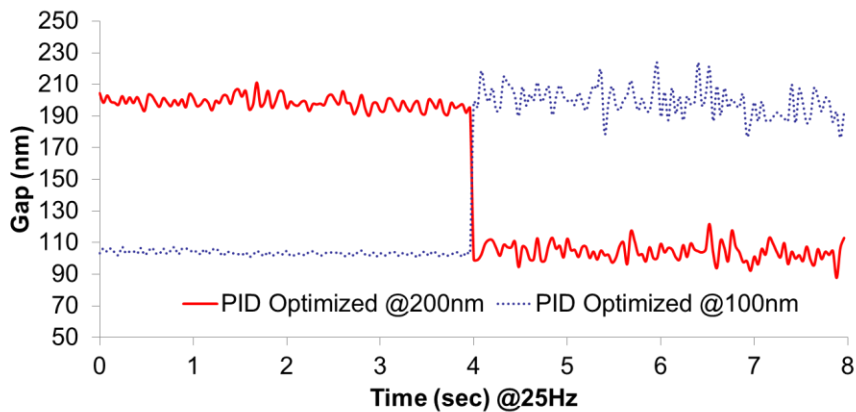


Figure 70. Static gapping results showing gap heights change when the gap target is adjusted in the control software.

### 5.3.2 Dynamic gap gauging

Dynamic gapping is made possible through gap control and manual actuation of the linear mechanic-bearings motor-driven stage. The stage travels in both X and Y directions, and has 10 nm resolution with various speed settings. The dynamic gap control process was performed as follows: While the wafer stage locked, the EWL head was first pulled-in to sub-200 nm gap region, followed by gap servo activation with a set gap target. The PID auto-tune module was then switched on to set the individual P, I, and D coefficients for the static gapping condition. The linear wafer stage was then actuated with an initial scan speed set at 1  $\mu\text{m}/\text{sec}$  to avoid catastrophic prism collision. PID auto-tune was performed again to learn the scanning gap condition. After acquiring optimized PID coefficients, the EWL head now scans over the wafer stage at targeted gap height. Figure 71 shows the real time scanning gapping signal with optimized controller at various gap targets.

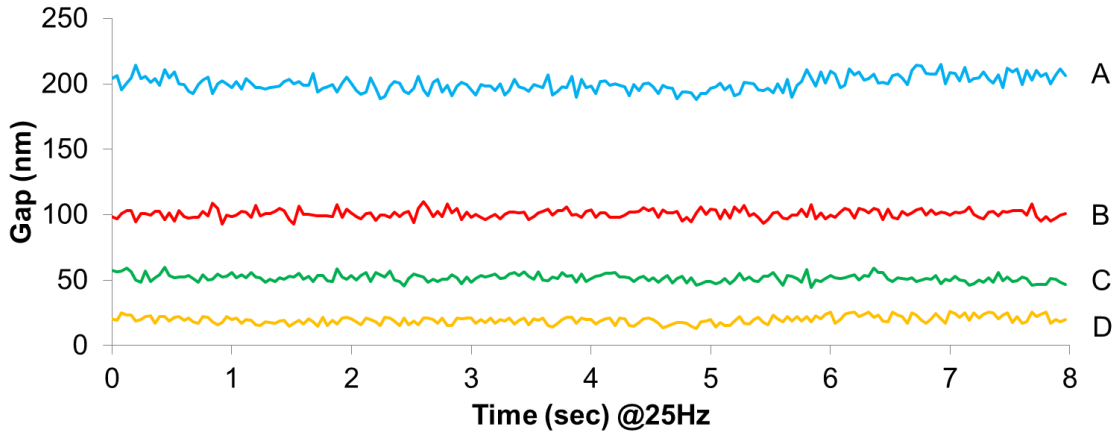


Figure 71. Dynamic gapping with optimized controller at various gap heights. Scan speed =1  $\mu\text{m}/\text{sec}$ .

To compare gapping performance at both static and scanning conditions, Figure 72 and Figure 73 show the static vs. scanning gapping signal with optimized controller at

100 nm and 50 nm gap targets, respectively. It is shown that at 100 nm gap target, dynamic gapping has slightly larger noise 4.64 nm compared to static gapping noise 1.38 nm. At 50 nm gap target, the gap noise difference becomes smaller, 1.23 nm in static gapping vs. 3.14 nm in dynamic gapping. The higher dynamic gapping noise is expected as the more gap disturbances such as stage vibration, wafer roughness and dust are present when scanning. However, both static and dynamic gapping gap noises are within tolerance level for dose control purpose. For the experimental conditions simulated, 4.64 nm gap noise corresponds to 0.6% dose fluctuation while 1.23 nm gap noise results in less than 0.2% dose fluctuation.

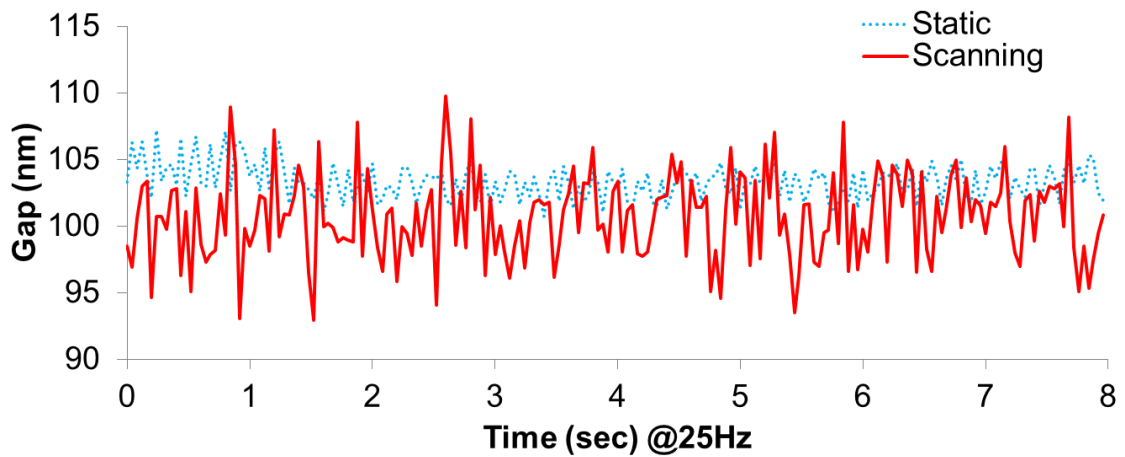


Figure 72. Comparative study on static vs. scanning gapping results with gap target set at 100 nm.

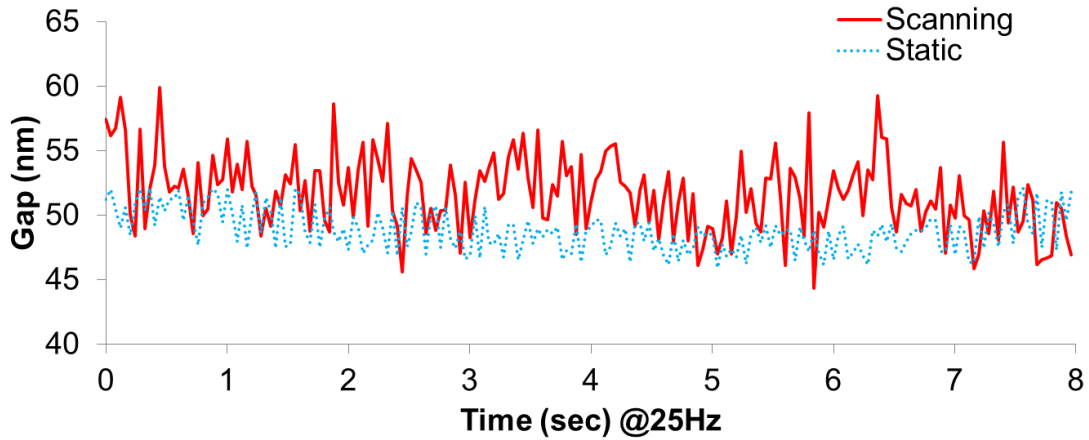


Figure 73. Comparative study on static vs. scanning gapping results with gap target set at 50 nm.

Experiments were performed to further confirm gap control by switching the wafer stage movement on and off, shown in Figure 74. The gap controller was optimized for static gapping condition at 80 nm. Scan speed was set at 1  $\mu\text{m}/\text{sec}$ . Stage movement was switched on and off every 150 seconds. It is shown that dynamic gapping has 7.32 nm gap noise compared to static gapping noise at 1.45 nm. The larger dynamic gapping noise is partially due to unoptimized PID controller as well as more gap disturbances.

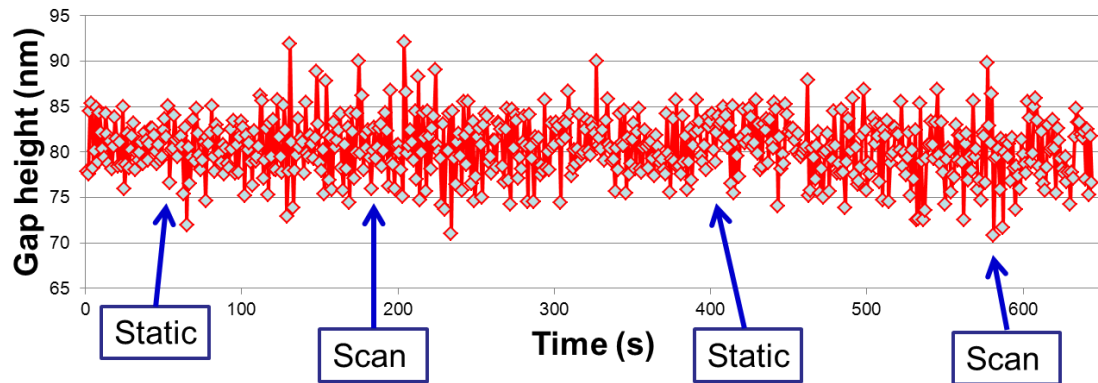


Figure 74. Plotted gap heights fluctuation when the wafer stage switches between stationary and scanning.

Compared to industrial scanner, the scan speeds used in our experiments are multiple orders of magnitude slower [154]. However, there is no fundamental show-stopper in terms of achieving high scan speed in the scanning EWL system. The primary limitation in the proto-typed system is the slow sampling rate (at 25 Hz) of the photodetector and the power meter used. Increasing the scan rate at slow sampling frequency may omit critical topography points on the wafer surface and create collision and scratches to prism surface. By adopting high bandwidth high precision optical detection systems, it is possible to achieve scan rate much higher than the 1  $\mu\text{m}/\text{sec}$  scan speed used in most of our experiments. Figure 75 shows the gapping signal with multiple scan speeds. It is observed that higher scan speeds have higher gap noise, which is an indication that the gap controller becomes less responsive due to the lack of gap sampling.

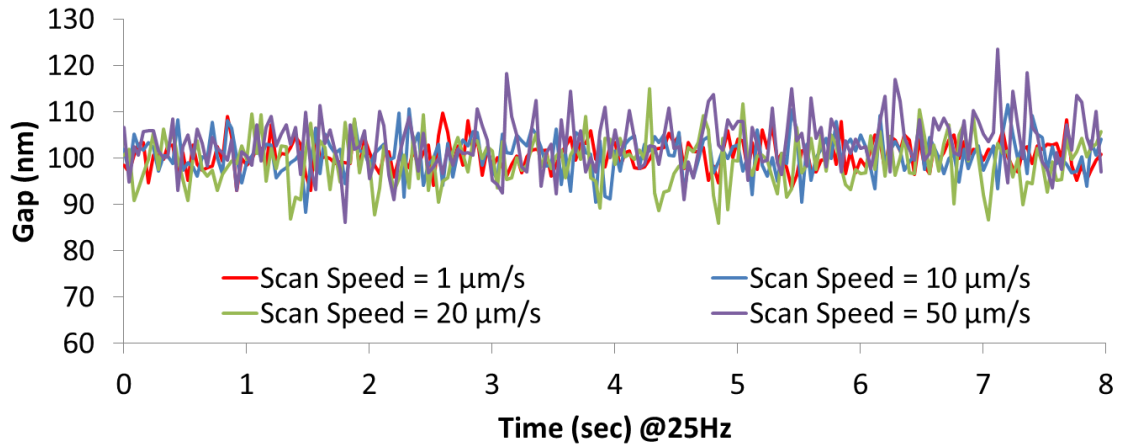


Figure 75. Dynamic gapping with different scan rate.

### 5.3.3 Imaging results

Imaging was carried out in the approach described in the section 4.2.5, after tuning and confirming static and scanning gap control. The wafer stage was held

stationary while the image field was exposed. After the exposure, the wafer scans in the linear direction at constant sub-100 nm gap to another isolated location to carry out the next exposure. The gap control system is always active during exposures and scanning.

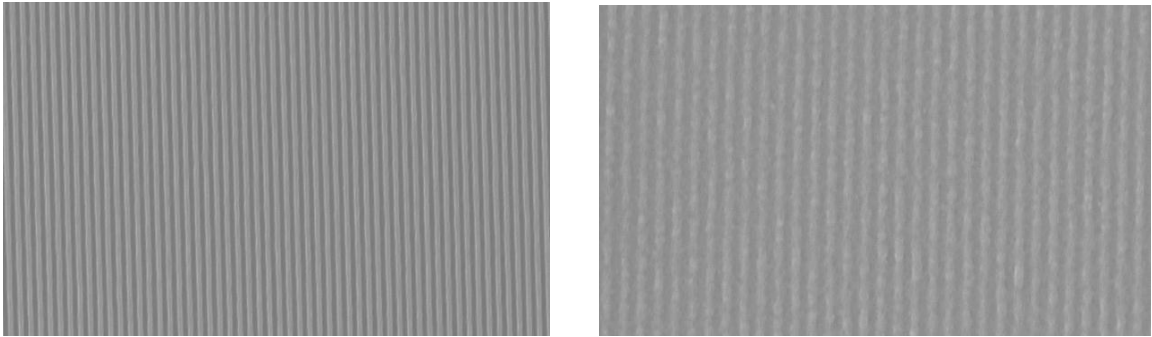


Figure 76. SEM snapshots of 1.35 NA line-and-space patterns imaged with stepping EWL using fused silica prism.

Standard resist processing is used in the experiment, as described in Chapter 3. 40-70 nm JSR ARX2928JN-7 methacrylate-based resist were spin-coated on top of appropriate thickness Brewer ARC29A-8 BARC or AZ Krf-17B-100 BARC, depending on the NA (pattern pitch) the samples were imaged at. Initial imaging results with fused silica prism showed significant contrast degradation and was contributed to poor alignment in the interferometer. A micrometer rotation stage was added to the head mount to allow for better alignment. The improved imaging results are shown in Figure 76. In addition, some image fields exhibit local non-uniformity as shown in Figure 77. This is due to the local gap variation (imperfections from the prism itself) underneath the prism. Improvement needs to be carried out to produce prism with super-flat 50  $\mu\text{m}$  wide tip.

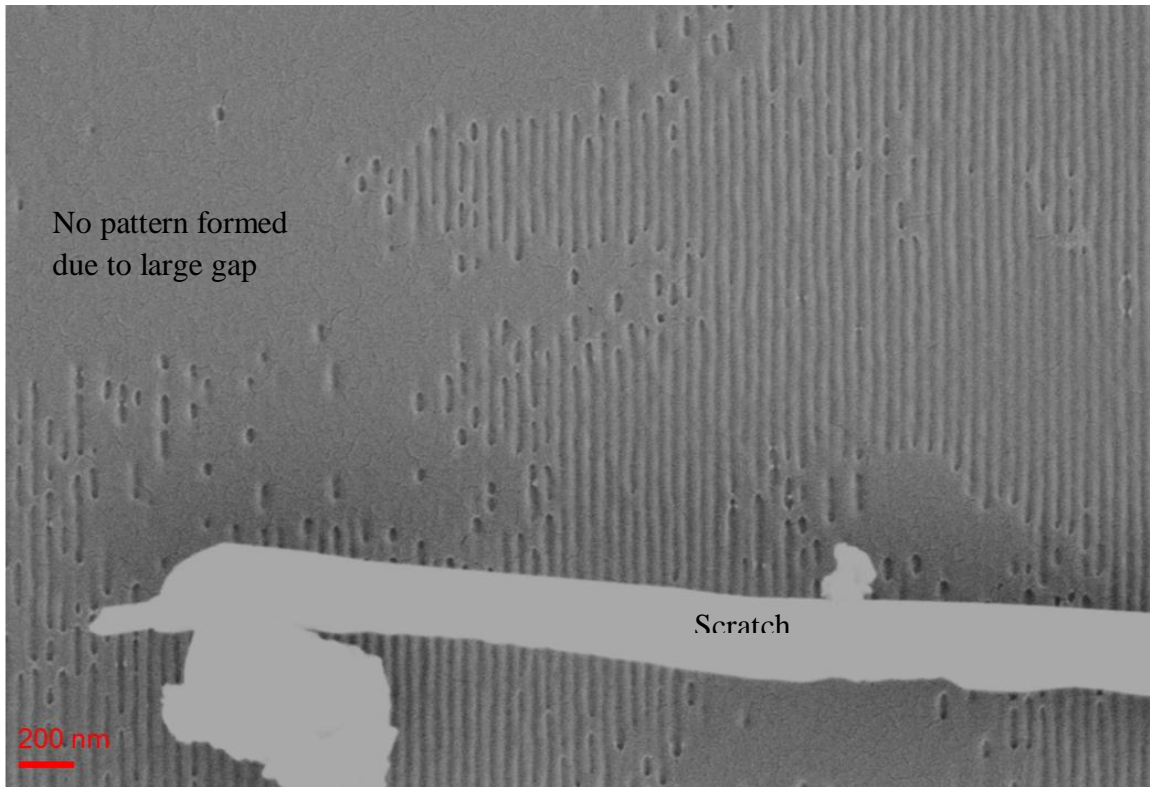


Figure 77. SEM snapshot of a non-uniform image field. 1.35 NA line-and-space patterns were imaged with stepping EWL using fused silica prism. Field non-uniformity is caused by local gap variations.

Similarly, imaging with sapphire prism produced comparable results at 1.2 NA, as shown in Figure 78. Ideally, sapphire prism is capable of up to 1.9 NA resolution, but the process window at such NA is much limited. Optical alignment becomes critical. SEM becomes extremely challenging considering the field width is on the order of 200  $\mu\text{m}$  and lack of focus reference.

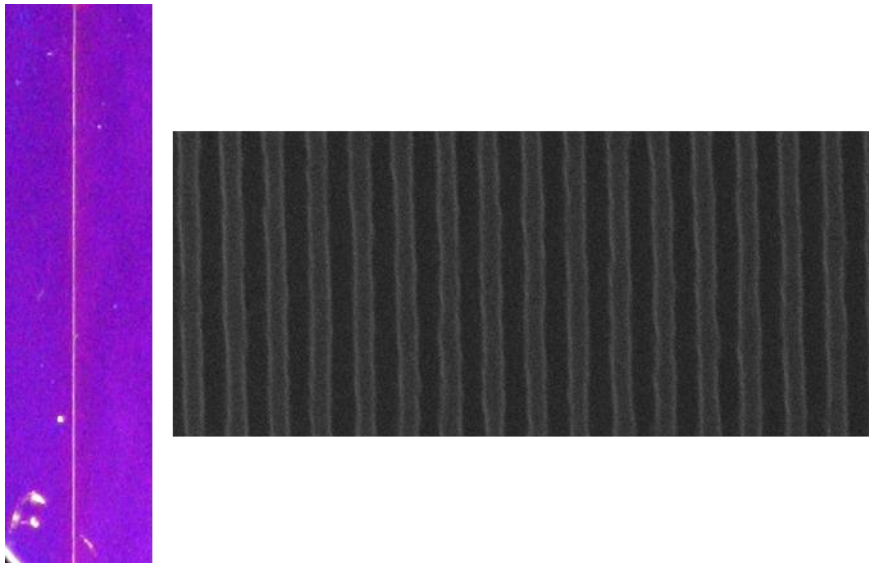


Figure 78. Left: photograph of an exposed silicon wafer sample. The bright line indicates the image field exposed with 1.2 NA stepping EWL using sapphire prism; Right: SEM snapshot of the image field.

---

## 6. CONCLUSIONS AND FUTURE WORK

---

In this thesis, the concept of evanescent wave lithography (EWL) and scanning EWL has been developed, explored, and presented. In order to meet the fast scaling pace in semiconductor IC manufacturing, innovative lithography technologies are demanded to print high resolution circuit features cost-effectively. Conventional optical lithography fails to scale beyond 32 nm due to lack of high index materials, and is being complemented and replaced by non-optical approaches surveyed in Chapter 1. While it is still early to predict the definitive technology for advanced lithography nodes, a hybrid patterning solution comprised of multiple lithography techniques is likely to prevail. While conventional optical lithography will continue to print less demanding lithography layers, it will transform to a supporting role in the advanced lithography nodes. Design rule evolution is another important observation in the transition to non-optical lithography regime. 2D structures are becoming increasingly difficult to print beyond 22 nm, forcing circuit layout designers to adopt 1D gridded design rules. This opens up opportunities for previously overlooked interference lithography which prints high contrast regular line-space grating structures.

Interference lithography operates on interfering two or more mutually coherent beams. While it is possible to build an EUV interference lithography system, the discussion in this thesis has been focused on 193 nm optical interference lithography. IL imaging theory and the study of its scalability to sub-22 nm nodes with NGLs was presented in Chapter 2. With the advent of regular design rules, IL becomes an attractive

candidate to pattern ultra-dense line-space grating templates. IL based on state-of-the-art 1.35 NA immersion lithography platforms allows patterning down to 37 nm half-pitch and is extendable to 22 nm with pitch division techniques such as double patterning lithography or directed self-assembly lithography. Several key IL challenges towards integration, namely manufacturability, field size, and resolution were introduced. This thesis research looks to address the challenges associated with IL resolution and field size.

IL would need to be capable of imaging NA  $>1.35$  to meet its resolution requirement. A novel optical lithography approach called evanescent wave lithography was developed. Compatible with IL imaging platforms, EWL relies on the near field perturbation of evanescent fields to extract and re-propagate the high NA imaging components. The theoretical evaluation of EWL and static imaging results were presented in Chapter 3 which allows for imaging down to 26 nm using 193 nm two-beam IL together with evanescent wave optical effects at the imaging plane. The physical limitations of imaging imposed by the refractive indices of the materials were surpassed through the interference of evanescent waves at near fields. A special situation where imaging at a system numerical aperture above the resist refractive index was discussed which requires re-defining effective refractive indices for Snell's law on absorbing media. Lithography results were shown using image media including air, water, and a high refractive index fluid together with a systematic gauge control to determine the nanometer scale gap requirements and tolerances to achieve adequate image contrast into the resist. It is established that gap depths in the sub-100 nm regime to be sufficient for

acceptable throughput. Using this static EWL platform, multiple next-generation high index inorganic resists have been developed and evaluated.

Building on the successful static EWL imaging results, a prototype dynamic scanning system capable of full field imaging was devised in Chapter 4, along with various system design concepts and considerations. A scanning EWL imaging head was designed and fabricated with a two-stage gap control system including a DC noise canceling carrying air-bearing pad that scans at a constant air gap with regulated air pressure, and a AC noise canceling piezoelectric transducer with real-time closed-loop feedback from gap detection. Specific design tasks including gap detection, prism design and alignment, servo control and software integration, feedback actuation and scanning have been accomplished to achieve sub-100 nm gapping and imaging up to 1.4 NA with fused silica optical element and 1.8 NA with sapphire.

To validate the design concepts, the prototyped scanning EWL imaging head was integrated into the Amphibian two-beam interference platform, detailed in Chapter 5. Experimental results showed successful gap gauging at sub-100 nm with gap noise root-mean-square around 2.3 nm in static gapping and 3.5 nm in linear scanning gapping. Imaging results were obtained with both prisms in a step-and-scan imaging mode due to stage limitation. Image contrast degradations observed in early samples were resolved by thoroughly studying system alignment, environmental vibration sources and process conditions. The final gapping and imaging results confirmed the promise of scanning EWL to extend optical lithography to sub-22 nm generations.

This work is significant in that it is the first study to systematically investigate evanescent wave lithography on an IL platform for sub-22 nm lithography nodes. Further,

while there are studies to date to demonstrate EWL or solid immersion lithography at UV wavelengths, this work has demonstrated record resolution of 26 nm with single patterning optical lithography means at 193 nm. The systematic gap detection and gauging method used in both static and scanning EWL has been novel to the lithography field. The static EWL apparatus has also been used extensively to develop new resists and immersion fluids. This work is the first study of extending evanescent wave lithography into full-field dynamic scanning system. Many design concepts developed in this system are unique in lithography systems such as near-field gap detection, prism design and head design. The successful sub-100 nm gapping and imaging results confirmed the potential to keep investigating near-field lithography approaches. Finally in the big picture, this work proposes a novel scanning EWL+ IL as a template patterning technique in the scope of next generation lithography. The use of a regular patterning template with additive lithography steps to re-work the circuitry is also novel in advanced lithography research.

The results of this dissertation points to several interesting directions for future work. From the imaging head design perspective, the prototype system suffers three major drawbacks: monitor laser alignment, prism leveling and complicated imaging head assembly procedure. With the use of prism as the final optical element, the incident imaging beam and monitor beam comes in at an oblique angle. The direct consequence of this off-axis design is that different portions of the monitor laser beam hits the prism flat surface as it moves up and down. Since the flat has a width of only 50  $\mu\text{m}$ , intensity variation across the cross-section area of the beam results in additional gap signal variation. This puts a strict requirement on monitor beam uniformity. A potential solution

is to replace the prism with a half-ball or lens to enable on-axis illumination and detection. However, manufacturing of hyper-NA imaging quality sapphire half-ball or lens may prove to be difficult.

Lack of multi-point alignment technique in the system resulted in a non-ideal empirical expose-and-align method. The leveling of the prism with reference to the ground is not guaranteed in the system. This causes wearing of the prism and non-uniform image field. Adding additional piezoelectric transducers and leveling monitor laser on the periphery of the image head would allow for precision leveling. Alternatively, by adopting a flexure or vacuum design that forces the imaging prism to self-conform to wafer surface is another way to achieve leveling.

The imaging head assembly procedure described in Figure 43 needs to be improved. To realize the actuation function of the piezoelectric transducer, the transducer needs to be loaded. This was achieved in the system by locking in the transducer with a precision machined spacer, which was first made at a machine shop and then grind onsite iteratively to match the required spacing. By adopting a “one-body” design where the two ends of the transducer are attached to the same component would avoid the above-mentioned complication.

From the hardware respective, a couple of upgrades can be used to allow for better system performance. Firstly, faster optical power meter and higher piezoelectric amplifier drive current would allow for faster frequency response of the gap detection. This would allow for faster stage scanning motion. Secondly, the prisms used in the imaging head are not defect free, which is related to the prism grinding process. The wet grinding solution has particles of size comparable to that of the flat, leading to scratches.

A technique that produces higher quality, defect-free prism with 50  $\mu\text{m}$  flat surface is needed to ensure uniform image field.

To fully utilize the merits of the scanning EWL, the system needs to realize dynamic scanning function, which requires nanometer precision stage, coupled of with phase locking optics and controller. Such systems have already been realized on larger dimensions (200 nm grating) scanning beam interference imaging tools. The challenge however remains to scale the control precision to  $\sim 20\text{nm}$  resolution. Lastly, it is the ultimate goal of scanning EWL to employ a fluid bearing design to enable fluid gap. Adding fluid to the gap will not only relax the gapping requirement, but also allow for higher NA imaging and efficient photon tunneling. However, the abnormal fluid-resist interaction observed in static EWL experiments need to be understood before the investigation.

In summary, the evanescent wave lithography systems developed in this thesis prove to be capable of ultra-high NA optical imaging despite material limitations. The static EWL apparatus has experimentally demonstrated high contrast 1:1 line-space grating structure with resolution down to 26 nm. The prototyped scanning EWL system validated the design concepts and demonstrated sub-100 nm gapping and step-and-scan imaging. While dynamic scanning is limited by stage precision, this work represent the important milestone of the demonstration of near-field scanning optical lithography and its potential for subsequent development.

---

## 7. REFERENCES

---

- [1] Y. Borodovsky, "Marching to the beat of Moore's Law," in *Proceedings of SPIE*, 2006, vol. 6153, p. 615301.
- [2] J. H. Bruning, "Optical lithography—thirty years and three orders of magnitude: the evolution of optical lithography tools," in *Proceedings of SPIE*, 1997, vol. 3051, p. 14.
- [3] D. G. Flagello, "Evolution as applied to optical lithography," in *Proceedings of SPIE*, 2007, vol. 6827, p. 68271N.
- [4] T. A. Brunner, "Why optical lithography will live forever," *Journal of Vacuum Science & Technology B: Microelectronics and Nanometer Structures*, vol. 21, p. 2632, 2003.
- [5] B. J. Lin, "NGL comparable to 193-nm lithography in cost, footprint, and power consumption," *Microelectronic Engineering*, vol. 86, no. 4–6, pp. 442–447, 2009.
- [6] T. Matsuyama, Y. Ohmura, and D. M. Williamson, "The lithographic lens: its history and evolution," in *Proceedings of SPIE*, 2006, vol. 6154, p. 615403.
- [7] J. de Klerk, C. Wagner, R. Droste, L. Levasier, L. Jorritsma, E. van Setten, H. Kattouw, J. Jacobs, and T. Heil, "Performance of a 1.35 NA ArF immersion lithography system for 40-nm applications," in *Proceedings of SPIE*, 2007, vol. 6520, p. 65201Y.
- [8] J. W. Goodman, *Introduction to Fourier Optics*, 3rd ed. Roberts & Company Publishers, 2004.
- [9] R. L. Easton Jr., *Fourier Methods in Imaging*, 2nd ed. Wiley, 2010.
- [10] A. J. Den Dekker and A. Van den Bos, "Resolution: a survey," *JOSA A*, vol. 14, no. 3, pp. 547–557, 1997.
- [11] Lord Rayleigh, "XLVI. Investigations in optics, with special reference to the spectroscope," *Philosophical Magazine Series 5*, vol. 8, no. 50, p. 403.
- [12] K. Ronse, P. De Bisschop, A. M. Goethals, J. Hermans, R. Jonckheere, S. Light, U. Okoroanyanwu, R. Watso, D. McAfferty, J. Ivaldi, and others, "Status and critical challenges for 157-nm lithography," *Microelectronic engineering*, vol. 73, pp. 5–10, 2004.
- [13] P. A. Zimmerman, B. J. Rice, E. C. Piscani, and V. Liberman, "High index 193 nm immersion lithography: the beginning or the end of the road," in *Proceedings of SPIE*, 2009, vol. 7274, p. 727420.
- [14] M. D. Levenson, N. S. Viswanathan, and R. A. Simpson, "Improving resolution in photolithography with a phase-shifting mask," *IEEE Transactions on Electron Devices*, vol. 29, no. 12, pp. 1828–1836, 1982.
- [15] N. B. Cobb, A. Zakhor, M. Reihani, F. Jahansooz, and V. N. Raghavan, "Experimental results on optical proximity correction with variable-threshold resist model," in *Proceedings of SPIE*, 1997, vol. 3051, p. 458.
- [16] T. A. Brunner, "Rim phase-shift mask combined with off-axis illumination: a path to 0.5 ( $\lambda$ )/numerical aperture geometries," *Optical Engineering*, vol. 32, p. 2337, 1993.

- [17] B. W. Smith, L. V. Zavyalova, and A. Estroff, "Benefiting from polarization effects on high-NA imaging," in *Proceedings of SPIE*, 2004, vol. 5377, p. 68.
- [18] A. E. Rosenbluth, S. Bukofsky, C. Fonseca, M. Hibbs, K. Lai, A. F. Molless, R. N. Singh, and A. K. . Wong, "Optimum mask and source patterns to print a given shape," *Journal of Microlithography, Microfabrication, and Microsystems*, vol. 1, p. 13, 2002.
- [19] L. W. Liebmann, "Layout impact of resolution enhancement techniques: impediment or opportunity?," in *Proceedings of the 2003 international symposium on Physical design*, 2003, pp. 110–117.
- [20] D. Basting, "History and future prospects of excimer lasers," in *Proceedings of SPIE*, Singapore, Singapore, 2002, pp. 25–34.
- [21] D. Brown and N. Farrar, "The Continuation of Moore's Law," *Laser Technik Journal*, vol. 6, no. 4, pp. 40–43, 2009.
- [22] J. Leonard, J. Carriere, J. Stack, R. Jones, M. Himel, J. Childers, and K. Welch, "An improved process for manufacturing diffractive optical elements (DOEs) for off-axis illumination systems," in *Proceedings of SPIE*, 2008, vol. 6924, p. 69242O.
- [23] E. van Setten, W. de Boeij, B. Hepp, N. le Masson, G. Swinkels, and M. van de Kerkhof, "Pushing the boundary: low-k<sub>1</sub> extension by polarized illumination," in *Proceedings of SPIE*, 2007, vol. 6520, p. 65200C.
- [24] M. Mulder, A. Engelen, O. Noordman, G. Streutker, B. van Drienuizen, C. van Nuenen, W. Endendijk, J. Verbeeck, W. Bouman, A. Bouma, R. Kazinczi, R. Socha, D. Jürgens, J. Zimmermann, B. Trauter, J. Bekaert, B. Laenens, D. Corliss, and G. McIntyre, "Performance of FlexRay: a fully programmable illumination system for generation of freeform sources on high NA immersion systems," presented at the Optical Microlithography XXIII, San Jose, California, USA, 2010, p. 76401P–76401P–10.
- [25] Y. Granik and N. B. Cobb, "MEEF as a Matrix," in *Proceedings of SPIE*, 2002, vol. 4562, p. 980.
- [26] H. J. Levinson, *Principles of lithography*. SPIE Press, 2005.
- [27] C. Mack, *Fundamental Principles of Optical Lithography: The Science of Microfabrication*. Wiley, 2008.
- [28] M. Saied, F. Foussadier, J. Belledent, Y. Trouiller, I. Schanen, E. Yesilada, C. Gardin, J. C. Urbani, F. Sundermann, F. Robert, C. Couderc, F. Vautrin, L. LeCam, G. Kerrien, J. Planchot, C. Martinelli, B. Wilkinson, Y. Rody, A. Borjon, N. Morgana, J.-L. Di-Maria, and V. Farys, "3D mask modeling with oblique incidence and mask corner rounding effects for the 32nm node," in *Proceedings of SPIE*, Monterey, CA, USA, 2007, pp. 673050–673050–11.
- [29] J. H. Bruning, "Optical lithography: 40 years and holding," in *Proceedings of SPIE*, San Jose, CA, USA, 2007, pp. 652004–652004–13.
- [30] F. Staals, A. Andryzhyieuskaya, H. Bakker, M. Beems, J. Finders, T. Hollink, J. Mulkens, A. Nachtwein, R. Willekers, P. Engblom, T. Gruner, and Y. Zhang, "Advanced wavefront engineering for improved imaging and overlay applications on a 1.35 NA immersion scanner," presented at the Optical Microlithography XXIV, San Jose, California, USA, 2011, p. 79731G–79731G–13.
- [31] K. Suzuki, B. Smith, and B. W. Smith, *Microlithography: Science and Technology, Second Edition*, 2nd ed. CRC Press, 2007.

- [32] H. Ito, "Evolution and progress of deep UV resist materials," *Journal of Photopolymer Science and Technology*, vol. 11, no. 3, pp. 379–393, 1998.
- [33] H. Ito, "Rise of chemical amplification resists from laboratory curiosity to paradigm enabling Moore's law," in *Proceedings of SPIE*, San Jose, CA, USA, 2008, pp. 692302–692302–15.
- [34] H. Ito, H. D. Truong, R. D. Allen, W. Li, P. R. Varanasi, K. -J Chen, M. Khojasteh, W. -S Huang, S. D. Burns, and D. Pfeiffer, "ArF excimer laser resists based on fluoroalcohol," *Polymers for Advanced Technologies*, vol. 17, no. 2, pp. 104–115, Feb. 2006.
- [35] G. M. Gallatin, P. Naulleau, D. Niakoula, R. Brainard, E. Hassanein, R. Matyi, J. Thackeray, K. Spear, and K. Dean, "Resolution, LER, and sensitivity limitations of photoresists," in *Proceedings of SPIE*, 2008, vol. 6921, p. 69211E.
- [36] W. D. Hinsberg, F. A. Houle, M. I. Sanchez, J. A. Hoffnagle, G. M. Wallraff, D. R. Medeiros, G. M. Gallatin, and J. L. Cobb, "Extendibility of chemically amplified resists: another brick wall?," in *Proceedings of SPIE*, 2003, vol. 5039, p. 1.
- [37] H. J. Levinson, "Extreme ultraviolet lithography's path to manufacturing," *J. Micro/Nanolith. MEMS MOEMS*, vol. 8, no. 4, p. 041501, 2009.
- [38] M. Trikeriotis, W. J. Bae, E. Schwartz, M. Krysak, N. Lafferty, P. Xie, B. Smith, P. A. Zimmerman, C. K. Ober, and E. P. Giannelis, "Development of an inorganic photoresist for DUV, EUV, and electron beam imaging," in *Proceedings of SPIE*, 2010, vol. 7639, p. 76390E.
- [39] A. Telecky, P. Xie, J. Stowers, A. Grenville, B. Smith, and D. A. Keszler, "Photopatternable inorganic hardmask," *Journal of Vacuum Science & Technology B: Microelectronics and Nanometer Structures*, vol. 28, p. C6S19, 2010.
- [40] J. Finders, M. Dusa, and S. Hsu, "Double patterning lithography: The bridge between low  $k_1$  ArF and EUV," *Microlithography World*, vol. 17, no. 1, p. 2, 2008.
- [41] B. J. Lin, "Sober view on extreme ultraviolet lithography," *Journal of Microlithography, Microfabrication, and Microsystems*, vol. 5, p. 033005, 2006.
- [42] T. Ebihara, "Beyond  $k_1=0.25$  lithography: 70-nm L/S patterning using KrF scanners," in *Proceedings of SPIE*, Monterey, CA, USA, 2003, pp. 985–994.
- [43] P. Zimmerman, "Double patterning lithography: double the trouble or double the fun?," *SPIE Newsroom*, 2009.
- [44] "International Technology Roadmap for Semiconductors, 2010 Update." [Online]. Available: <http://www.itrs.net/>. [Accessed: 31-May-2011].
- [45] B. Wu, "Next-generation lithography for 22 and 16 nm technology nodes and beyond," *Sci. China Inf. Sci.*, vol. 54, no. 5, pp. 959–979, May 2011.
- [46] P. J. Silverman, "Extreme ultraviolet lithography: overview and development status," *J. Microlith., Microfab., Microsyst.*, vol. 4, no. 1, p. 011006, 2005.
- [47] S. Wurm, "SEMATECH pushes extreme UV lithography forward," *SPIE Newsroom*, 2006.
- [48] C. Wagner, J. Bacelar, N. Harned, E. Loopstra, S. Hendriks, I. de Jong, P. Kuerz, L. Levasier, M. van de Ker, M. Lowisch, H. Meiling, D. Ockwell, R. Peeters, E. van Setten, J. Stoeldraijer, S. Young, J. Zimmerman, and R. Kool, "Performance validation of ASML's NXE:3100," presented at the Extreme Ultraviolet (EUV) Lithography II, San Jose, California, USA, 2011, p. 79691F–79691F–12.

- [49] P. P. Naulleau, C. N. Anderson, L.-M. Baclea-an, P. Denham, S. George, K. A. Goldberg, G. Jones, B. McClinton, R. Miyakawa, S. Rekawa, and N. Smith, "Critical challenges for EUV resist materials," presented at the Advances in Resist Materials and Processing Technology XXVIII, San Jose, California, USA, 2011, pp. 797202–797202–10.
- [50] B. Wu and A. Kumar, "Extreme ultraviolet lithography: A review," *J. Vac. Sci. Technol. B*, vol. 25, no. 6, p. 1743, 2007.
- [51] C. Bencher, H. Dai, L. Miao, Y. Chen, P. Xu, Y. Chen, S. Oemardani, J. Sweis, V. Wiaux, J. Hermans, L.-W. Chang, X. Bao, H. Yi, and H.-S. P. Wong, "Mandrel-based patterning: density multiplication techniques for 15nm nodes," presented at the Optical Microlithography XXIV, San Jose, California, USA, 2011, p. 79730K–79730K–10.
- [52] A. Carlson and T. J. . Liu, "Low-variability negative and iterative spacer processes for sub-30-nm lines and holes," 2009.
- [53] P. Xie and B. W. Smith, "Analysis of higher order pitch division for sub-32nm lithography," in *Proceedings of SPIE*, San Jose, CA, USA, 2009, p. 72741Y–72741Y–8.
- [54] Y. Chen, P. Xu, L. Miao, Y. Chen, X. Xu, D. Mao, P. Blanco, C. Bencher, R. Hung, and C. S. Ngai, "Self-aligned triple patterning for continuous IC scaling to half-pitch 15nm," presented at the Optical Microlithography XXIV, San Jose, California, USA, 2011, p. 79731P–79731P–8.
- [55] C. Cork, J. C. Madre, and L. Barnes, "Comparison of triple-patterning decomposition algorithms using aperiodic tiling patterns," in *Proceedings of SPIE*, 2008, vol. 7028, p. 702839.
- [56] S. Matsui and Y. Ochiai, "Focused ion beam applications to solid state devices," *Nanotechnology*, vol. 7, pp. 247–258, 1996.
- [57] R. D. Piner, J. Zhu, F. Xu, S. Hong, and C. A. Mirkin, "'Dip-pen' nanolithography," *Science*, vol. 283, no. 5402, p. 661, 1999.
- [58] H. I. Smith, R. Menon, A. Patel, D. Chao, M. Walsh, and G. Barbastathis, "Zone-plate-array lithography: A low-cost complement or competitor to scanning-electron-beam lithography," *Microelectronic engineering*, vol. 83, no. 4–9, pp. 956–961, 2006.
- [59] C. Vieu, F. Carcenac, A. Pepin, Y. Chen, M. Mejias, A. Lebib, L. Manin-Ferlazzo, L. Couraud, and H. Launois, "Electron beam lithography: resolution limits and applications," *Applied Surface Science*, vol. 164, no. 1–4, pp. 111–117, 2000.
- [60] E. Platzgummer, "Maskless lithography and nanopatterning with electron and ion multibeam projection," presented at the Alternative Lithographic Technologies II, San Jose, California, USA, 2010, pp. 763703–763703–12.
- [61] C. Klein, J. Klikovits, L. Szikszai, E. Platzgummer, and H. Loeschner, "50 keV electron-beam projection maskless lithography (PML2): results obtained with 2,500 programmable 12.5-nm sized beams," in *Proceedings of SPIE*, 2010, vol. 7637, p. 76370B.
- [62] P. Petric, C. Bevis, A. Carroll, H. Percy, M. Zywno, K. Standiford, A. Brodie, N. Bareket, and L. Grella, "REBL: A novel approach to high speed maskless electron beam direct write lithography," *Journal of Vacuum Science & Technology B: Microelectronics and Nanometer Structures*, vol. 27, p. 161, 2009.

- [63] M. J. Wieland, G. De Boer, G. F. Ten Berge, M. Van Kervinck, R. Jager, J. J. M. Peijster, E. Slot, S. Steenbrink, T. F. Teepen, and B. J. Kampherbeek, "MAPPER: high-throughput maskless lithography," in *Proceedings of SPIE*, 2010, vol. 7637, p. 76370F.
- [64] L. J. Guo, "Nanoimprint Lithography: Methods and Material Requirements," *Advanced Materials*, vol. 19, no. 4, pp. 495–513, Feb. 2007.
- [65] M. D. Stewart, S. C. Johnson, S. V. Sreenivasan, D. J. Resnick, and C. G. Willson, "Nanofabrication with step and flash imprint lithography," *J. Microlith., Microfab., Microsyst.*, vol. 4, no. 1, p. 011002, 2005.
- [66] Y. S. Jung, J. B. Chang, E. Verploegen, K. K. Berggren, and C. A. Ross, "A Path to Ultranarrow Patterns Using Self-Assembled Lithography," *Nano Letters*, vol. 10, no. 3, pp. 1000–1005, Mar. 2010.
- [67] G. M. Whitesides, J. P. Mathias, and C. T. Seto, "Molecular self-assembly and nanochemistry: a chemical strategy for the synthesis of nanostructures," *Science*, vol. 254, no. 5036, p. 1312, 1991.
- [68] D. P. Sanders, J. Cheng, C. T. Rettner, W. D. Hinsberg, H. C. Kim, H. Trung, A. Fritz, S. Harrer, S. Holmes, and M. Colburn, "Integration of Directed Self-Assembly with 193 nm Lithography," *Journal of Photopolymer Science and Technology*, vol. 23, no. 1, pp. 11–18, 2010.
- [69] J. Y. Cheng, D. P. Sanders, H. D. Truong, S. Harrer, A. Friz, S. Holmes, M. Colburn, and W. D. Hinsberg, "Simple and Versatile Methods To Integrate Directed Self-Assembly with Optical Lithography Using a Polarity-Switched Photoresist," *ACS Nano*, vol. 4, no. 8, pp. 4815–4823, 2010.
- [70] D. J. C. Herr, "Directed Block Copolymer Self-Assembly for Nanoelectronics Fabrication," *Journal of Materials Research*, vol. 26, no. Special Issue 02, pp. 122–139, 2011.
- [71] C. Bencher, J. Smith, L. Miao, C. Cai, Y. Chen, J. Y. Cheng, D. P. Sanders, M. Tjio, H. D. Truong, S. Holmes, and others, "Self-assembly patterning for sub-15nm half-pitch: a transition from lab to fab," in *Proceedings of SPIE*, 2011, vol. 7970, p. 79700F.
- [72] C. T. Black, R. Ruiz, G. Breyta, J. Y. Cheng, M. E. Colburn, K. W. Guarini, H. C. Kim, and Y. Zhang, "Polymer self assembly in semiconductor microelectronics," *IBM Journal of Research and Development*, vol. 51, no. 5, pp. 605–633, 2007.
- [73] C. Webb, "Intel design for manufacturing and evolution of design rules," in *Proceedings of SPIE*, San Jose, CA, USA, 2008, pp. 692503–692503–8.
- [74] P. Nikolsky, N. Davydova, and R. Goossens, "Topological and model based approach to pitch decomposition for double patterning," in *Proceedings of SPIE*, 2008, pp. 679205–679205–12.
- [75] M. C. Smayling, H. Liu, and L. Cai, "Low k1 logic design using gridded design rules," in *Proceedings of SPIE*, 2008, vol. 6925, p. 69250B.
- [76] C. Bencher, H. Dai, and Y. Chen, "Gridded design rule scaling: taking the CPU toward the 16nm node," in *Proceedings of SPIE*, San Jose, CA, USA, 2009, p. 72740G–72740G–10.
- [77] M. Fritze, B. Tyrrell, T. Fedynyshyn, M. Rothschild, and P. Brooker, "High-throughput hybrid optical maskless lithography: all-optical 32-nm node imaging," in *Proceedings of SPIE*, 2005, vol. 5751, p. 1058.

- [78] H. H. Solak and Y. Ekinici, "Achromatic spatial frequency multiplication: A method for production of nanometer-scale periodic structures," *Journal of Vacuum Science & Technology B: Microelectronics and Nanometer Structures*, vol. 23, p. 2705, 2005.
- [79] S. R. J. Brueck, S. H. Zaidi, X. Chen, and Z. Zhang, "Interferometric lithography—from periodic arrays to arbitrary patterns\* 1," *Microelectronic engineering*, vol. 41, pp. 145–148, 1998.
- [80] M. Farhoud, J. Ferrera, A. J. Lochtefeld, T. E. Murphy, M. L. Schattenburg, J. Carter, C. A. Ross, and H. I. Smith, "Fabrication of 200 nm period nanomagnet arrays using interference lithography and a negative resist," *Journal of Vacuum Science & Technology B: Microelectronics and Nanometer Structures*, vol. 17, no. 6, pp. 3182–3185, 1999.
- [81] A. Bourov, Y. Fan, F. C. Cropanese, N. V. Lafferty, L. V. Zavyalova, H. Kang, and B. W. Smith, "Immersion microlithography at 193 nm with a Talbot prism interferometer," in *Proceedings of SPIE*, 2004, vol. 5377, p. 1573.
- [82] D. J. Smith, M. McCullough, B. Xu, S. Smith, M. L. Schattenburg, T. Jitsuno, and T. Mikami, "Large area pulse compression gratings fabricated onto fused silica substrates using scanning beam interference lithography," *Ultrahigh Intens. Lasers: Dev. Sci. Emerg. Appl.*, 2008.
- [83] V. Ramanan, E. Nelson, A. Brzezinski, P. V. Braun, and P. Wiltzius, "Three dimensional silicon-air photonic crystals with controlled defects using interference lithography," *Applied physics letters*, vol. 92, p. 173304, 2008.
- [84] J. J. Wang, F. Walters, X. Liu, P. Sciortino, and X. Deng, "High-performance, large area, deep ultraviolet to infrared polarizers based on 40 nm line/78 nm space nanowire grids," *Applied physics letters*, vol. 90, no. 6, pp. 061104–061104, 2007.
- [85] "International Technology Roadmap for Semiconductors, 2009 Edition." [Online]. Available: <http://www.itrs.net/Links/2009ITRS/Home2009.htm>. [Accessed: 02-Jun-2011].
- [86] B. W. Smith, Y. Fan, J. Zhou, N. Lafferty, and A. Estroff, "Evanescent wave imaging in optical lithography," in *Proceedings of SPIE*, 2006, vol. 6154, p. 61540.
- [87] J. Zhou, "Hyper-NA imaging in optical lithography at oblique angles," Rochester Institute of Technology, Ph.D. dissertation, 2007.
- [88] Y. Fan, "Pushing the limits of hyper-NA optical lithography," Rochester Institute of Technology, Ph.D. dissertation, 2005.
- [89] B. W. Smith, A. Bourov, Y. Fan, F. Cropanese, and P. Hammond, "Amphibian XIS: an immersion lithography microstepper platform," in *Proc. SPIE*, 2005, vol. 5754, pp. 751–759.
- [90] V. Liberman, M. Rothschild, S. T. Palmacci, R. Bristol, J. Byers, N. J. Turro, X. Lei, N. O'Connor, and P. A. Zimmerman, "High-index immersion lithography: preventing lens photocontamination and identifying optical behavior of LuAG," in *Proceedings of SPIE*, 2008, vol. 6924, p. 692416.
- [91] S. Owa and H. Nagasaka, "Advantage and feasibility of immersion lithography," *Journal of Microlithography, Microfabrication, and Microsystems*, vol. 3, p. 97, 2004.
- [92] R. H. French, V. Liberman, H. V. Tran, J. Feldman, D. J. Adelman, R. C. Wheland, W. Qiu, S. J. McLain, O. Nagao, M. Kaku, and others, "High-index

- immersion lithography with second-generation immersion fluids to enable numerical apertures of 1.55 for cost effective 32-nm half pitches,” in *Proceedings of SPIE*, 2007, vol. 6520, p. 65201O.
- [93] P. A. Zimmerman, C. Peski, B. Rice, J. Byers, N. J. Turro, X. Lei, J. L. Gejo, V. Liberman, S. Palmacci, M. Rothchild, and others, “Status of high-index materials for generation-three 193nm immersion lithography,” *Journal of Photopolymer Science and Technology*, vol. 20, no. 5, pp. 643–650, 2007.
- [94] P. A. Zimmerman, B. Rice, R. Rodriguez, M. F. Zettel, M. Trikeriotis, D. Wang, Y. Yi, W. J. Bae, C. K. Ober, and E. Giannelis, “The use of Nanocomposite Materials for High Refractive Index Immersion Lithography,” *Journal of Photopolymer Science and Technology*, vol. 21, no. 5, pp. 621–629, 2008.
- [95] A. J. Merriam, D. S. Bethune, J. A. Hoffnagle, W. D. Hinsberg, C. M. Jefferson, J. J. Jacob, and T. Litvin, “A solid-state 193-nm laser with high spatial coherence for sub-40-nm interferometric immersion lithography,” in *Proceedings of SPIE*, 2007, vol. 6520, p. 65202Z.
- [96] B. W. Smith, “Is interference lithography really on the roadmap,” 2010.
- [97] “Actinix.” [Online]. Available: <http://www.actinix.com/index.htm>. [Accessed: 20-Jul-2011].
- [98] T. A. Savas, M. L. Schattenburg, J. M. Carter, and H. I. Smith, “Large-area achromatic interferometric lithography for 100 nm period gratings and grids,” *Journal of Vacuum Science & Technology B: Microelectronics and Nanometer Structures*, vol. 14, no. 6, pp. 4167–4170, 1996.
- [99] T. A. Savas, S. N. Shah, M. L. Schattenburg, J. M. Carter, and H. I. Smith, “Achromatic interferometric lithography for 100-nm-period gratings and grids,” *Journal of Vacuum Science & Technology B: Microelectronics and Nanometer Structures*, vol. 13, no. 6, pp. 2732–2735, Nov. 1995.
- [100] C. Rydberg, J. Bengtsson, and T. Sandström, “Dynamic laser speckle as a detrimental phenomenon in optical projection lithography,” *J. Microlith., Microfab., Microsyst.*, vol. 5, no. 3, p. 033004, 2006.
- [101] C. G. Chen, P. T. Konkola, R. K. Heilmann, G. S. Pati, and M. L. Schattenburg, “Image metrology and system controls for scanning beam interference lithography,” *Journal of Vacuum Science & Technology B: Microelectronics and Nanometer Structures*, vol. 19, p. 2335, 2001.
- [102] B. W. Smith, Y. Fan, J. Zhou, N. Lafferty, and A. Estroff, “Evanescent wave imaging in optical lithography,” in *Proceedings of SPIE*, 2006, vol. 6154, p. 61540A.
- [103] T. M. Bloomstein, M. F. Marchant, S. Deneault, D. E. Hardy, and M. Rothschild, “22-nm immersion interference lithography,” *Opt. Express*, vol. 14, no. 14, pp. 6434–6443, Jul. 2006.
- [104] R. T. Greenway, R. Hendel, K. Jeong, A. B. Kahng, J. S. Petersen, Z. Rao, and M. C. Smayling, “Interference assisted lithography for patterning of 1D gridded design,” in *Proceedings of SPIE*, 2009, vol. 7271, p. 72712U.
- [105] V. Axelrad and M. C. Smayling, “16nm with 193nm immersion lithography and double exposure,” in *Proceedings of SPIE*, 2010, vol. 7641, p. 764109.
- [106] M. Asano, “Sub-100 nm lithography with KrF exposure using multiple development method,” *Jpn. J. Appl. Phys*, vol. 38, no. 12B pt 1, pp. 6999–6999, 1999.

- [107] S. Tarutani, H. Tsubaki, and S. Kanna, "Development of materials and processes for double patterning toward 32 nm node ArF immersion lithography," *Journal of Photopolymer Science and Technology*, vol. 21, no. 5, pp. 685–690, 2008.
- [108] M. Maenhoudt, R. Gronheid, N. Stepanenko, T. Matsuda, and D. Vangoidsenhoven, "Alternative process schemes for double patterning that eliminate the intermediate etch step," in *Proceedings of SPIE*, 2008, vol. 6924, p. 69240P.
- [109] S. Jeon, V. Malyarchuk, J. A. Rogers, and G. P. Wiederrecht, "Fabricating three-dimensional nanostructures using two photon lithography in a single exposure step," *Optics Express*, vol. 14, no. 6, pp. 2300–2308, 2006.
- [110] W. G. Oldham, "The use of contrast enhancement layers to improve the effective contrast of positive photoresist," *IEEE Transactions on Electron Devices*, vol. 34, no. 2, pp. 247–251, 1987.
- [111] IMEC, "Internal Communication," 2007.
- [112] D. Perret, J. Simon, S. Gaugiran, C. Cutler, T. Cardolaccia, A. Pikon, I. Guerin, C. Lapeyre, S. Derrough, C. Szmanda, and others, "Materials for double patterning strategies: Development and application," *Microelectronic Engineering*, vol. 86, no. 4–6, pp. 757–760, 2009.
- [113] D. K. Lee, Y. Cao, D. Abdallah, J. Yin, M. Thiyagarajan, and R. Dammel, "Freezing Materials For Double Patterning," *Journal of Photopolymer Science and Technology*, vol. 22, no. 5, pp. 653–661, 2009.
- [114] N. Bekiaris, H. Cervera, J. Dai, R. Kim, A. Acheta, T. Wallow, J. Kye, H. J. Levinson, T. Nowak, and J. Yu, "A lithographic and process assessment of photoresist stabilization for double-patterning using 172-nm photoresist curing," in *Proceedings of SPIE*, 2008, vol. 6923, p. 692321.
- [115] H. Nakamura, T. Shibata, K. Rikimaru, S. Ito, S. Tanaka, and S. Inoue, "Ion implantation as insoluble treatment for resist-stacking process," 2010.
- [116] C. Lapeyre, S. Barnola, I. Servin, S. Gaugirana, V. Salvetat, N. Magome, A. J. Hazelton, and M. McCallum, "Impact of CD and overlay errors on double-patterning processes," in *Proceedings of SPIE*, 2009, vol. 7274, p. 72740W.
- [117] T. Ando, M. Takeshita, R. Takasu, Y. Yoshii, J. Iwashita, S. Matsumaru, S. Abe, and T. Iwai, "Pattern freezing process free litho-litho-etch double patterning," in *Proceedings of SPIE*, 2008, vol. 7140, p. 71402H.
- [118] C. A. Mack and J. E. Connors, "Fundamental differences between positive-and negative-tone imaging," in *Proceedings of SPIE*, 1992, vol. 1674, p. 328.
- [119] M. C. Smayling, C. Bencher, H. D. Chen, H. Dai, and M. P. Duane, "Apf pitch-halving for 22nm logic cells using gridded design rules," in *Proceedings of SPIE*, 2008, vol. 6925, p. 69251E.
- [120] J. Y. Cheng, C. A. Ross, H. I. Smith, and E. L. Thomas, "Templated Self-Assembly of Block Copolymers: Top-Down Helps Bottom-Up," *Advanced Materials*, vol. 18, no. 19, pp. 2505–2521, 2006.
- [121] C. J. Hawker and T. P. Russell, "Block copolymer lithography: Merging 'bottom-up' with 'top-down' processes," *MRS bulletin*, vol. 30, no. 12, pp. 952–966, 2005.
- [122] G. M. Whitesides and B. Grzybowski, "Self-assembly at all scales," *Science*, vol. 295, no. 5564, p. 2418, 2002.
- [123] M. Li and C. K. Ober, "Block copolymer patterns and templates," *Materials Today*, vol. 9, no. 9, pp. 30–39, 2006.

- [124] R. A. Segalman, H. Yokoyama, and E. J. Kramer, "Graphoepitaxy of spherical domain block copolymer films," *Advanced Materials*, vol. 13, no. 15, pp. 1152–1155, 2001.
- [125] E. W. Edwards, M. F. Montague, H. H. Solak, C. J. Hawker, and P. F. Nealey, "Precise Control over Molecular Dimensions of Block-Copolymer Domains Using the Interfacial Energy of Chemically Nanopatterned Substrates," *Advanced Materials*, vol. 16, no. 15, pp. 1315–1319, Aug. 2004.
- [126] M. Fritze, T. M. Bloomstein, B. Tyrrell, T. H. Fedynyshyn, N. N. Efremow Jr, D. E. Hardy, S. Cann, D. Lennon, S. Spector, M. Rothschild, and others, "Hybrid optical maskless lithography: Scaling beyond the 45 nm node," *Journal of Vacuum Science & Technology B: Microelectronics and Nanometer Structures*, vol. 23, p. 2743, 2005.
- [127] C. Bencher, Y. Chen, H. Dai, W. Montgomery, and L. Huli, "22nm half-pitch patterning by CVD spacer self alignment double patterning (SADP)," in *Proceedings of SPIE*, 2008, vol. 6924, p. 69244E.
- [128] H. Dai, J. Sweis, C. Bencher, Y. Chen, J. Shu, X. Xu, C. Ngai, J. Huckabay, and M. Weling, "Implementing self-aligned double patterning on non-gridded design layouts," in *Proceedings of SPIE*, 2009, vol. 7275, p. 72751E.
- [129] W. Srituravanich, N. Fang, C. Sun, Q. Luo, and X. Zhang, "Plasmonic nanolithography," *Nano letters*, vol. 4, no. 6, pp. 1085–1088, 2004.
- [130] S. Zhu, A. W. Yu, D. Hawley, and R. Roy, "Frustrated total internal reflection: A demonstration and review," *American Journal of Physics*, vol. 54, p. 601, 1986.
- [131] H. A. Macleod, *Thin-film optical filters*. Taylor & Francis, 2001.
- [132] Y. Fan, A. Bourov, L. Zavyalova, J. Zhou, A. Estroff, N. Lafferty, and B. W. Smith, "ILSim: a compact simulation tool for interferometric lithography," in *Proceedings of SPIE*, 2005, vol. 5754, p. 1805.
- [133] R. W. Ditchburn, *Light*. Courier Dover Publications, 1991.
- [134] P. Mehrotra, C. W. Holzwarth, and R. J. Blaikie, "Solid-immersion Lloyd's mirror as a testbed for plasmon-enhanced high-NA lithography," in *Proceedings of SPIE*, 2011, vol. 7970, p. 79701L.
- [135] Y. K. Goh, L. Chen, A. Dorgelo, X. Peng, N. Lafferty, B. Smith, P. Zimmerman, W. Montgomery, I. Blakey, and A. K. Whittaker, "Sensitive polysulfone based chain scissioning resists for 193nm lithography," presented at the Advances in Resist Materials and Processing Technology XXVIII, San Jose, California, USA, 2011, p. 79722E–79722E–8.
- [136] B. Baylav, M. Zhao, R. Yin, P. Xie, C. Scholz, B. Smith, T. Smith, and P. Zimmerman, "Alternatives to chemical amplification for 193nm lithography," presented at the Advances in Resist Materials and Processing Technology XXVII, San Jose, California, USA, 2010, pp. 763915–763915–12.
- [137] M. Krysak, M. Trikeriotis, E. Schwartz, N. Lafferty, P. Xie, B. Smith, P. Zimmerman, W. Montgomery, E. Giannelis, and C. K. Ober, "Development of an inorganic nanoparticle photoresist for EUV, e-beam, and 193nm lithography," presented at the Advances in Resist Materials and Processing Technology XXVIII, San Jose, California, USA, 2011, p. 79721C–79721C–6.
- [138] C. J. Tay, S. H. Wang, C. Quan, B. L. Ng, and K. C. Chan, "Surface roughness investigation of semi-conductor wafers," *Optics & Laser Technology*, vol. 36, no. 7, pp. 535–539, 2004.

- [139] W. Srituravanich, L. Pan, Y. Wang, C. Sun, D. B. Bogy, and X. Zhang, "Flying plasmonic lens in the near field for high-speed nanolithography," *Nature Nanotechnology*, vol. 3, no. 12, pp. 733–737, 2008.
- [140] B. J. Choi, V. Sreenivasan, G. C. Willson, M. Colburn, T. Bailey, and J. Ekerdt, *Method and system of automatic fluid dispensing for imprint lithography processes*. 2002.
- [141] M. Shinoda, K. Saito, T. Ishimoto, T. Kondo, A. Nakaoki, M. Furuki, M. Takeda, and M. Yamamoto, "High-density near-field readout over 100-GB capacity using a solid immersion lens with NA of 2.05," in *Proceedings of SPIE*, 2003, vol. 5069, p. 306.
- [142] J. S. Berg and N. K. S. Lee, *Flying head with adjustable actuator load*. Google Patents, 2001.
- [143] S. Imanishi, T. Ishimoto, Y. Aki, T. Kondo, K. Yamamoto, and M. Yamamoto, "Near-field optical head for disc mastering process," *JPN J APPL PHYS PART 1 REGUL PAP SHORT NOTE REV PAP*, vol. 39, no. 2, pp. 800–805, 2000.
- [144] L. P. Ghislain and V. B. Elings, "Near-field scanning solid immersion microscope," *Applied physics letters*, vol. 72, no. 22, pp. 2779–2781, 1998.
- [145] F. Zijp, *Near-field optical data storage*. 2007.
- [146] A. Arnau, *Piezoelectric transducers and applications*. Springer, 2008.
- [147] J. A. H. Stotz and M. R. Freeman, "A stroboscopic scanning solid immersion lens microscope," *Review of scientific instruments*, vol. 68, p. 4468, 1997.
- [148] M. Shinoda, K. Saito, T. Ishimoto, T. Kondo, A. Nakaoki, M. Furuki, M. Takeda, Y. Akiyama, T. Shimouma, and M. Yamamoto, "High-density near-field optical disc recording using phase change media and polycarbonate substrate," in *Proceedings of SPIE*, 2004, vol. 5380, p. 224.
- [149] K. Ogata, *Modern control engineering*. Prentice Hall, 2010.
- [150] M. L. Schattenburg, C. G. Chen, R. K. Heilmann, P. T. Konkola, and G. Pati, "Progress toward a general grating patterning technology using phase-locked scanning beams," in *Proceedings of SPIE*, 2002, vol. 4485, p. 378.
- [151] "LabVIEW PID Control Toolkit User Manual," *National Instruments*, 2008.
- [152] H. Amick, M. Gendreau, T. Busch, and C. Gordon, "Evolving criteria for research facilities: vibration," in *Proceedings of SPIE*, 2005, vol. 5933, p. 593303.
- [153] A. Bourov, "A systematic approach to determining the limits of nanolithography at extreme NA," Rochester Institute of Technology, 2008.
- [154] J. Mulkens, J. de Klerk, M. Leenders, F. de Jong, and J. W. Cromwijk, "Latest developments on immersion exposure systems," in *Proceedings of SPIE*, 2008, vol. 6924, p. 69241P.